Microstructural and Interface Engineering of Garnet-Type Fast Li-ion-Conductor for Use in Solid-State Batteries

by

Asma Sharafi

A dissertation submitted in partial fulfillment
of the requirements for the degree of
Doctor of Philosophy
(Mechanical Engineering)
in The University of Michigan
2017

Doctoral Committee:

Associate Professor Jeff. Sakamoto, Chair
Associate Professor Donald J. Siegel
Assistant Professor Neil P. Dasgupta
Associate Professor Pierre Ferdinand P. Poudeu

Asma Sharafi

sharafi@umich.edu

ORCID iD: 0000-0001-7809-579X

DEDICATION

This thesis is dedicated to my love (Owjan) who has been a constant source of support and encouragement

ACKNOWLEDGMENTS

This thesis becomes a reality with the kind support and help of many individuals. I would like to extend my sincere thanks to all of them.

First and foremost, I would like to express my sincere gratitude to my advisor Professor. Jeff Sakamoto for his continuous support during my PhD study and research, for his patience, motivation, enthusiasm, and immense knowledge. This dissertation could not have been finished without his encouragement and mentorship. I would also like to thank my committee members Professor. Donald J. Siegel, Professor. Neil P. Dasgupta and Professor. Pierre Ferdinand P. Poudeu for their support and great insight toward my research.

I owe much of the completion of this dissertation to numerous collaborations and discussions with scientists. Particularly, I would like to acknowledge Dr. Jeff Wolfenstine, Dr. Nancy Dudney, Dr. Jagjit Nanda, Dr. Erik Herbert, and their lab members. Their stimulating thoughts, advice and contributions were pivotal to success of this work. I also would like to extend my thanks to all present and past lab mates in Sakamoto's research group over the years, the success of each work depends on the nature of the working environment. They created a friendly and cooperative atmosphere at work. I specially would like to thank Dena, Regina and Yunsung for all their great supports and their friendship. Throughout my PhD, I had the opportunity to mentor undergraduate students, I should thank Marcus Lee and Catherine Haslam, who tirelessly and with much enthusiasm tackled all challenges we faced to keep our research

running smoothly. I must also thank the people outside of our group including Eric Kazyak, Seungho Yu, and Robert Kerns for their assistance to collect data, interpret results and engage in discussions at various points of my work.

My greatest admiration goes to the love of my life, Owjan, who has always been a great support in all my struggles and frustrations. He was always there cheering me up and stood by me through the good times and bad. Thank you Owjan and I love you. I am deeply and forever indebted to my family, especially my mother (Fatemeh) and father (Gholamali) for always believing in me, for their continuous love and their unwavering supports in my decisions throughout my entire life, even being thousands of miles far away from home. My siblings Amin, Nafiseh, Ensi, and Hosna are the circle of love and strength, without them I could not have made it here.

Lastly, this work would have not been possible without the funding sources that allowed me to pursue my graduate studies. This work was funded by the U.S. Department of Energy (DOE) Office of Energy Efficiency and Renewable Energy (EERE) Vehicle Technologies Office (VTO) and Advanced Battery Material Research (BMR) program under contract DE-EE 00006821. This dissertation comprises a summary based on the following papers, which are referred to in the text:

Chapter 3: A. Sharafi, H.M. Mayer, J. Nanda, J. Wolfenstine, J. Sakamoto., Characterizing the Li-$Li_7La_3Zr_2O_{12}$ interface stability and kinetics as a function of temperature and current density. Journal of Power Sources, 2016 (302), 135-139 and E. Cheng, A. Sharafi, J. Sakamoto., Intergranular Li metal propagation through polycrystalline $Li_{6.25}Al_{0.25}La_3Zr_2O_{12}$ ceramic electrolyte, Electrochimica Acta, 2017 (223), 85-91.

Chapter 4: A. Sharafi, S. Yu, M. Naguib, M. Lee, C. Ma, H.M Harry, J. Nanda, M. Chi, D.J. Siegel, J. Nanda, J. Sakamoto., Impact of air exposure and surface chemistry on the Li-$Li_7La_3Zr_2O_{12}$ interfacial resistance, Journal of Material Chemistry A, 2017 (5) 13475-13487.

Chapter 5: A. Sharafi, E. Kazyak, A.L. Davis, S. Yu, T. Thompson, D.J. Siegel, N.P. Dasgupta, J. Sakamoto., Surface chemistry mechanism of ultra-low interfacial resistance in the solid-state electrolyte $Li_7La_3Zr_2O_{12}$, Accepted to Chemistry of Materials, 2017.

Chapter 6: A. Sharafi, C. Haslam, B. Kerns, J. Wolfenstine, J. Sakamoto., Controlling and correlating the effect of grain size with the mechanical and electrochemical properties of $Li_7La_3Zr_2O_{12}$ solid-state electrolyte, Accepted to Journal of Materials Chemistry A, 2017.

TABLE OF CONTENTS

LIST OF FIGURES

LIST OF TABLES

ABSTRACT

Large-scale adoption of electric vehicles requires batteries with higher energy density, lower cost, and improved safety compared to state-of-the-art (SOA) Li-ion batteries. This dissertation addresses the great-unmet need to develop beyond Li-ion batteries to facilitate the transition to electric power trains. The successful integration of metallic Li anodes into rechargeable batteries will enable a step increase in energy density compared to SOA Li-ion technology. However, the unstable nature of the electrode-electrolyte interface has limited the use of metallic Li anodes when paired with conventional organic solvent-based electrolytes. One approach to stabilize the metallic Li anode interface involves the integration of a solid-state electrolyte (SSE). Theoretical predictions suggest that Li dendrites will not form if a SSE exhibits a shear modulus that is approximately twice the shear modulus of metallic Li (G_{Li}= 4.2 GPa) or higher. This criterion indicates that ceramic Li-ion conducting solid-state electrolytes (SSE) can prevent dendrites. Thus, the development of solid-state batteries using SSE has been overlooked as a potential means to stabilize the metallic Li anode during cycling.

The garnet-type Li-ion conductor, $Li_7La_3Zr_2O_{12}$ (LLZO), is an example of a SSE that exhibits the unique combination of high Li-ion conductivity (1 $mS.cm^{-1}$ at 298 K) and stability against metallic Li. Additionally, LLZO has a shear modulus 14 times higher than metallic Li, thus should act as a physical barrier to prevent Li dendrite formation according to computational

analysis. However, despite satisfying the shear modulus criterion, Li metal propagation has been observed in polycrystalline LLZO. This dissertation hypothesizes that atomistic and microstructural defects such as porosity, grain boundaries, interfaces, and surface impurities govern the stability of the Li-LLZO interface. The effect of each defect was isolated through ceramic processing and analyzed using a suite of characterization tools such as X-ray diffraction, electron backscatter, scanning and transmission electron microscopy, electron energy loss, acoustic, and Raman spectroscopy, direct current cycling and complex impedance, Vickers indentation, and fracture toughness measurements. The overarching goal of this dissertation was to better understand the phenomena that control the stability of the Li-LLZO interface, quantify the contributions of each defect, and develop engineering approaches to tailor the LLZO microstructure and interface for maximum resistance to Li metal propagation during cycling. The implications of this dissertation could accelerate the development of high energy density solid-state batteries.

CHAPTER I

Aims and objectives

1.1 Motivation

The concentration of greenhouse gases (GHGs) including 82% carbon dioxide (CO_2), 10% methane (CH_4), 5% nitrous oxide (N_2O) and 3% fluorinated gases have increased substantially over the past century. Most climate scientists agree GHGs trap heat in the atmosphere and cause global warming (greenhouse effect). Among GHGs, CO_2 emissions are the primary source of global warming emitted from anthropomorphic activities that burn fossil fuels to provide power for the residential, commercial, electric power, and transportation sectors (Figure 1.1).[1-3] Between the various industries that consume energy in the U.S., electric power (39%) and transportation (27%), are the largest emitters of CO_2 in the US, respectively.[4] The transportation sector consists of passenger cars, light-duty trucks, medium and heavy-duty trucks, and aircraft; amongst which passenger vehicles consume the most energy. CO_2 emissions closely follow energy use because the primary source of energy is petroleum-based. Thus, electrifying transportation by enabling new technologies such as electric vehicles (EVs) including battery electric vehicles (BEVs) and plug-in hybrid electric vehicles (PHEVs) is a strategy to substantially reduce CO_2 emissions.

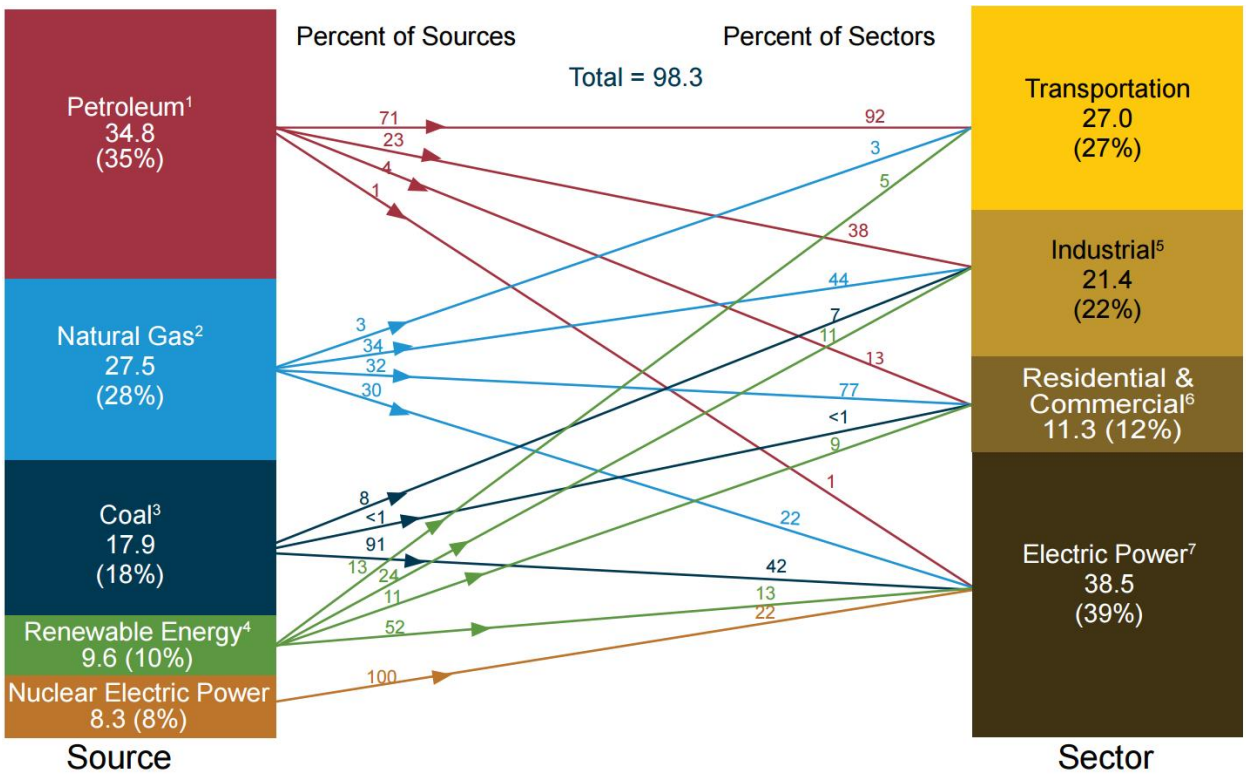

Figure 1.1. Estimated U.S. energy consumption in different sectors 2016.[3]

1.2 Vehicle electrification

Vehicle electrification requires the development of energy storage systems (ESS) that convert or store electrical energy. The selection of appropriate ESS technology for specific applications is typically based on the energy density and power density. The energy density is the amount of energy per unit volume ($Wh.l^{-1}$), while the power density is the amount of power per unit volume ($W.l^{-1}$). To compare the energy per unit mass, the terms specific energy ($Wh.kg^{-1}$) and specific power ($W.kg^{-1}$) are used.[5] Figure 1.2 shows a Ragone plot, which maps specific energy and specific power density for various ESS.[6] The diagonal dotted lines demarcate charge or discharge times. In selection of viable ESS for EVs, the energy density would represent the driving range on a single charge and the power density would represent how fast vehicles can accelerate, e.g. from 0 to 60 mph. From Figure 1.2, it is apparent that fuel cells offer the highest energy density but not power density, while capacitors offer the highest power density but not

energy density. Li-ion batteries (LIB) on the other hand, offer a compromise between energy density and power density, which makes them the leading technology to enable vehicle electrification.

This perspective outlines the main motivation of this thesis, which is focused on understanding and improving batteries. The following sections will describe the basic function of state-of-the-art (SOA) Li battery technology and identify strategies to improve their performance.

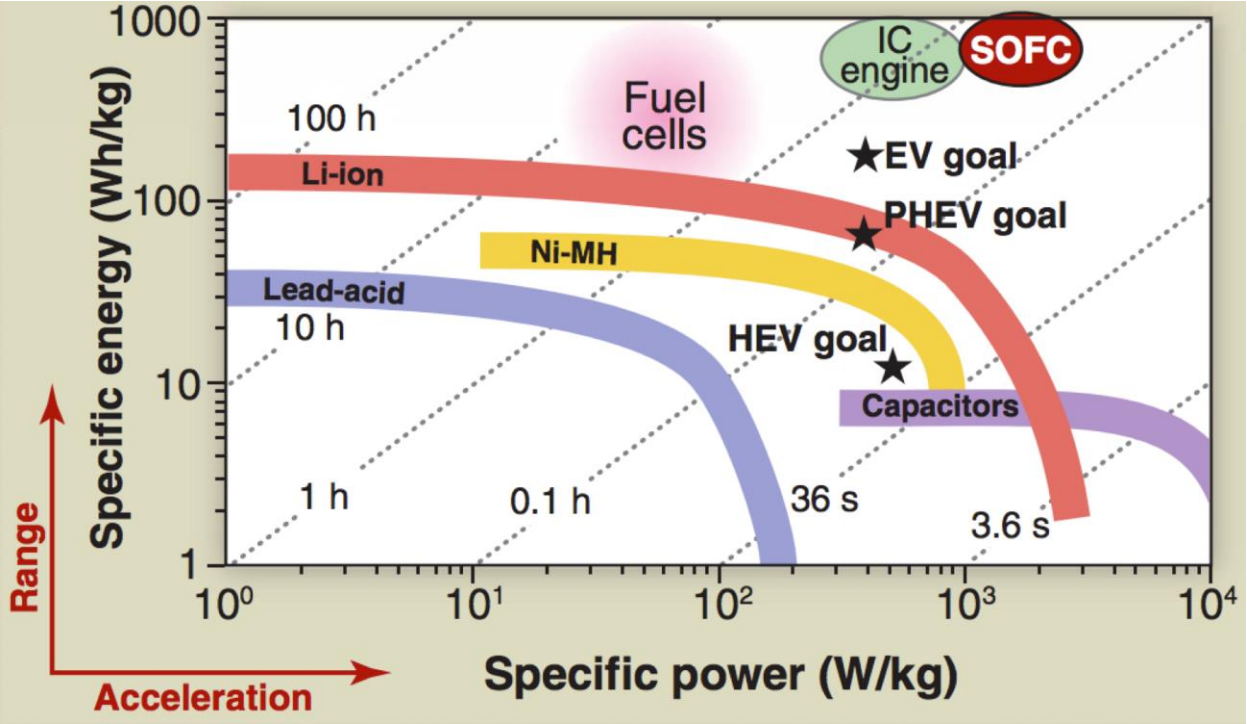

Figure 1.2. Ragone plot depicting specific energy against specific power for various energy storage technologies. The diagonal lines represent the time of charge for each energy storage technology.[6]

1.3 Li-ion battery principles of operation

Li-ion batteries (LIBs) are electrochemical devices that convert chemical energy into electrical energy, consisting of three main components: a positive electrode (cathode), a negative electrode (anode), and an ionically conducting electrolyte (Figure 1.3).[7] The electrodes transport ions to each other through a liquid electrolyte and are connected through an external circuit,

through which an electric current can flow. Cathode materials are typically a transition metal oxide with a layered structure such as lithium cobalt oxide ($LiCoO_2$) or lithium manganese oxide ($LiMn_2O_4$). Anode materials typically consist of a carbon-based material such as graphite. The electrolyte acts as a selective filter only allowing ions to pass while blocking the flow of electrons. Due to the relatively narrow electrochemical stability window of aqueous electrolytes, non-aqueous liquids such as organic solvent-based electrolytes are used. To prevent physical contact between electrodes, a porous polymeric membrane (separator) is used and is permeated by the liquid electrolyte. At the interface of the electrodes and the electrolyte the electrochemical reaction known as a reduction/oxidation (also known as "redox") occurs. The essence of LIBs is enabled by these redox reactions simultaneously occurring at both electrodes, which sends electrons through an external circuit to power a device such as an electric vehicle. The chemical driving force for charge and discharge results from the chemical potential differences between the cathode and anode, and is given by Equation 1:

$$\Delta G_{rxn} = -ZFE \quad (1)$$

where ΔG_{rxn} is the free energy change of the redox reaction, z is number of electron associated with charge transfer, F is Faraday's constant (96,486 coulombs) and E is the cell voltage. ΔG_{rxn} is can be given in Joules per mole of reaction; 1 Joule is the product of one Coulomb and one Volt.

Initially, all Li-ions (Li^+) are in the cathode, when the battery is assembled; while charging, Li-ions are extracted from the cathode, diffuse through electrolyte, and intercalate into the anode. Meanwhile, electrons move from the cathode to the anode through an external electric circuit. During discharging, the opposite reaction takes place, Li^+ are released from the anode simultaneously accompanied by the uptake of Li^+ in the cathode. During operation, the redox

reactions take place during charge and discharge. The half reactions and overall reaction can be described in the following equations:

$$\text{Cathode: } LiMO_2 \overset{Discharge/charge}{\longleftrightarrow} Li_{1-x}MO_2 + xLi^+ + xe^-$$

$$\text{Anode: } 6C + xLi^+ + xe^- \overset{Discharge/charge}{\longleftrightarrow} Li_xC_6$$

$$\text{Overall: } LiMO_2 + 6C \overset{Discharge/charge}{\longleftrightarrow} Li_xC_6 + Li_{1-x}MO_2$$

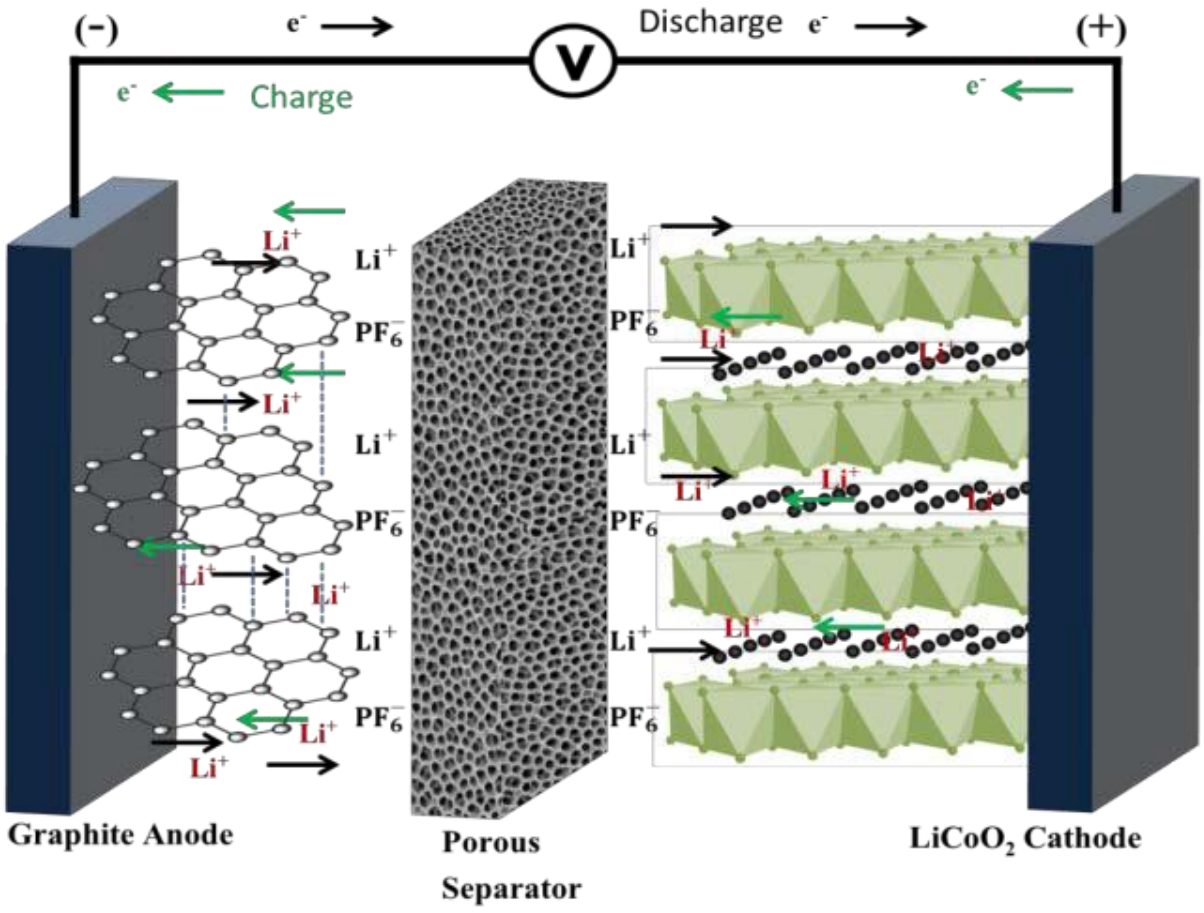

Figure 1.3. Lithium-ion battery schematic showing the three-main components of a LIB.[7]

1.4 Beyond Li-ion technology

At present, Li-ion batteries (LIBs) are the most promising technology to enable vehicle electrification. However, future EV demands will likely require performance characteristics that LIBs cannot provide. Hence, batteries with higher energy densities are required to enable viable and widespread adoption of EVs with improved characteristics such as longer driving range (>350 miles).[8-9] The U.S Department of Energy Vehicle Technologies Office (DOE VTO) defined benchmark performance targets for batteries that would results in electric vehicles competitive with gasoline or diesel-powered vehicles on a mass-produced basis (Table 1.1).[10] The metrics are energy density ($Wh.l^{-1}$), specific energy ($Wh.kg^{-1}$), specific power ($W.kg^{-1}$), self-discharge (% of initial cell capacity per day), operating temperature range (°C), cost ($\$.kWh^{-1}$), and cycle life (cycles).

From Table 1.1, it is clear that significant improvements in existing technology is required to meet the DOE VTO's targets. Vehicle electrification will require batteries with approximately 10 times greater energy densities at about one fifth the cost per kWh. For example, the longest running electric vehicle produced by Nissan (Nissan Leaf) utilizes a state of the art Li-ion battery pack with a specific energy density of 140 $Wh.kg^{-1}$, with a driving range of 100 miles. However, to match the driving range of a typical gasoline-powered vehicle (~ 300 mi), the battery is required to have considerably higher performance than what is currently available. Thus, the widespread use of electric vehicles requires the development of batteries with performance that greatly exceeds that of Li-ion batteries. A brief discussion of alternative battery chemistries is given in the next section.

Table 1.1. Department of Energy targets (2020) for PHEV and EVs.[10]

Feature	Current Status	Future Target
Battery pack cost	\$800.kWh^{-1}	<\$100-150.kWh^{-1}
Specific energy density	150-250 Wh.kg^{-1}	1000-3000 Wh.kg^{-1}
Specific power	500 W.kg^{-1}	2000 W.kg^{-1}
Operating Temperature	-20ºC-50ºC	-40ºC-85ºC
Calendar life	6-12 years	15 years
Driving range	100 miles	>300 miles

1.5 Solid-state batteries employing metallic Li anodes

The theoretical energy density of a battery is mainly defined by the theoretical capacities of the active materials at both electrodes (anode and cathode), and the electrochemical potential differences between the two electrodes.[1] Thus, to further increase the specific energy of rechargeable batteries, batteries employing different types of cathode and anode materials are under investigation. Along with the continuous efforts to substitute conventional cathode materials (intercalation cathodes such as $LiCoO_2$) with conversion cathodes such as sulfur (S) and oxygen (O_2) with much higher theoretical capacities,[11-12] considerable research on high performance anodes is also underway. There are primarily four different types of anode materials that could replace commercial graphite anodes: pyrolytic porous carbon, alloy-based anodes, conversion-type anodes, and metallic Li.[13-20] Among these candidates, metallic Li is believed to offer the highest increase in performance owing to its high theoretical capacity (3860 mAh.g^{-1}) and its low potential (0 V *vs.* Li^+/Li). [21,12, 22] However, the use of metallic Li as a negative electrode is hindered by the formation of Li dendrites when paired with conventional organic liquid electrolyte.[23] The dendrite formation, and subsequent fracture thereof to form Li moss,

eventually causes internal short circuiting resulting in self or instantaneous discharge.[24-25] The instantaneous discharge results in rapid Joule heating to the point that liquid electrolytes ignite, which can lead to explosions.[24-25] Thus, it becomes evident that most of the limitations in enabling metallic Li anodes arise from the instability of electrolyte.

One strategy to enable the use of metallic Li anodes includes the development of solid-state batteries (SSB) employing solid-state electrolyte (SSE). The use of SSE has been overlooked as a potential means to reduce the tendency to form Li dendrites and avoid short-circuiting. Many different inorganic SSE have been investigated since the 1970s,[26-27] however relatively few materials have been identified as promising candidates. The following section focuses on the required performance criteria for the selection of promising SSE to enable the use of metallic Li.

1.6 Solid-state electrolytes

Extensive research has been devoted to discovering and developing suitable SSE. There are myriad examples of solid-state electrolytes (SSEs) available in literature.[26-27] However, identifying the most promising SSE is not trivial due to the numerous selection criteria that must be simultaneously satisfied. Ideally, SSE should meet the following requirements to be considered for its use in SSBs:

- High ambient temperature ionic conductivity greater than $1x10^{-4}$ $S.cm^{-1}$
- Negligible electronic conductivity
- Low grain boundary resistances (for polycrystalline electrolyte membranes)
- Chemical and electrochemical stability against reactions with electrodes, and more specifically metallic Li
- Low interfacial resistance with both electrode materials
- Simple, scalable, and low-cost manufacturing

In the recent past, several SSE have been studied, however currently there are no SSE that can meet all the above requirements. A brief review of the most promising SSE is discussed in this section. The SSE materials can be categorized in two classes: amorphous and crystalline Li-ion conductors.

1.6.1 Amorphous Li-ion conductors

1.6.1.1 Glass LiPON

Lithium Phosphorous OxiNitride (LiPON) was first reported by Bates *et al*.[28] LiPON was synthesized in form of a thin film by nitriding of bulk phosphate glass to improve its stability toward water and salt solutions.[29] The thin films are typically synthesized by physical vapor deposition in an Ar-N_2 environment. The ionic conductivity was reported to be 2.26×10^{-6} $S.cm^{-1}$ at room temperature. Moreover, it has been shown that LiPON films are stable in contact with metallic Li.[30] A major advantage of LiPON is its excellent cyclability for more than 10,000 cycles. However, the maximum conductivity of this material is three orders of magnitude lower than the conventional liquid electrolyte and it must be made using vacuum deposition systems, which limits widespread use.

1.6.1.2 Sulfide glasses

The high ionic conductivities and low activation energies observed in sulfide-based glassy electrolytes have attracted great interest for their use as SSE.[31] These benefits can be attributed to the weaker bonding of Li with the non-bridging sulfur anions, due to the higher polarizability and softer basicity of the sulfide ion.[32] Sulfide glasses of nominal composition B_2S_3-Li_2S-LiX (X = F, Cl, Br, I) were synthesized to study the effect of polarizability on conductivity.[33] Conductivities of the order of 10^{-3} $S.cm^{-1}$ were demonstrated with the maximum conductivity for the LiI substituted glass systems. It has been shown the ionic conductivity can be improved to

values as high as high as 10^{-2} S.cm^{-1} at room temperature by changing the stoichiometry (B_2O_3–0.57Li_2O – 0.85LiCl). Similar room temperature conductivities (10^{-3} S.cm^{-1}) have been reported for the well-known fast-ion conducting $GeS_2 + Li_2S + LiI$ glass system.[34] This system was further optimized for higher ionic conductivity and improved thermal and chemical stability required for next generation SSE applications by doping with Ga_2S_3 and La_2S_3.[34] Clearly high Li-ion conductivities were observed in sulfide glasses, but these glasses are highly hygroscopic, which could complicate large-scale manufacturing.

1.6.2 Crystalline Li-ion conductors

1.6.2.1 Perovskite-Type

The perovskite–type material with the general formula ABO_3, has a three-dimensional crystal structure composed of corner sharing BO_6 octahedra. The A ions reside in the middle of the cubic cell and can move from cell to cell by hopping through a square set of four oxide ions where there is a vacancy in the adjacent cell. The perovskite-type Lithium Lanthanum Titanate ($Li_{3x}La_{(2/3-x)}\square_{(1/3-2x)}TiO_3$, LLTO) shows excellent bulk Li-ion conductivity (>10^{-3} S.cm^{-1}) when x~0.3.[35] The introduction of La^{3+} ions into the lattice can replace three Li^+ ions in the Perovskite structure, introducing two vacancies and increase ionic conductivity.[36] Li-ion hopping occurs through square planer bottlenecks between A sites (Figure 1.4). Although LLTO offers high ionic conductivity, several key technical problems limit its use as viable SSE. First polycrystalline LLTO (the practical form compared to the single crystal form) has inherently high grain boundary resistance thus reducing the total conductivity to ~ 10^{-5} S.cm^{-1}. Second, the spontaneous reduction of Ti^{4+} to Ti^{3+} upon contact with metallic Li makes LLTO impractical for use with metallic Li.

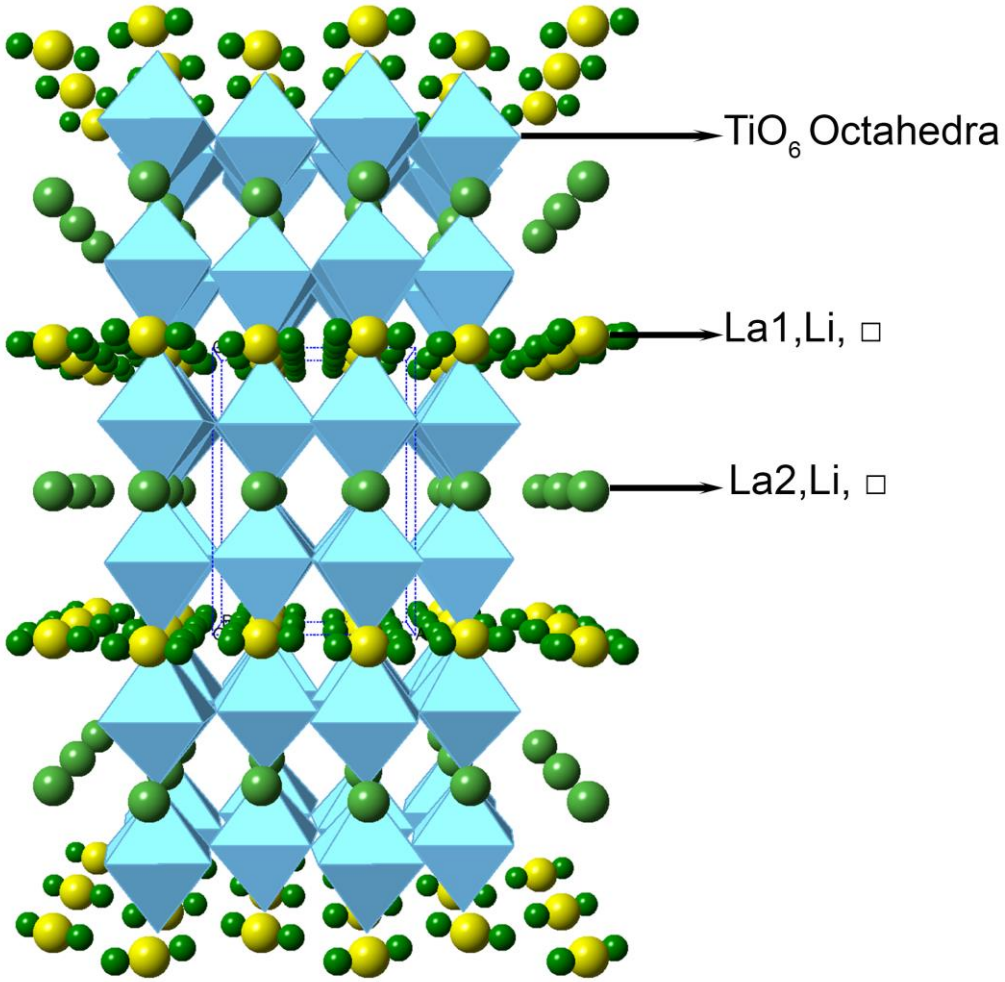

Figure 1.4. Idealized crystal structure of LLTO perovskite. The Li and La atoms and vacancies are distributed over A-sites in yellow and green spheres, the polyhedra represent TiO_6 units.

1.6.2.2 NaSICON-Type

Another type of Li-ion conductor is an extension of the crystal structure reported by Hagman *et al*. with composition $NaA_2^{IV}(PO_4)_3$ (A^{IV}=Ge, Ti, and Zr) known as NaSICON.[37-39] The NaSICON type Li-ion conductor has a similar composition with the general formula $LiA_2^{IV}(PO_4)_3$ (A^{IV}=Ge, Ti, and Zr).[40] The structure of these materials can be described as $[A_2P_3O_{12}]^-$ frameworks containing AO_6 octahedra and PO_4 tetrahedral (Figure 1.5). These polyhedral frameworks form 3D interconnected channels where the mobile alkali ions are

distributed and can move from site to site. Ti containing NaSICON ($Li_2Ti_2(PO_4)_3$ has found to possess the maximum ionic conductivity.[40] Furthermore, Aono *et al*., reported substitution of trivalent cations such as Al^{3+} for Ti^{4+} can improve the ionic conductivity considerably.[40] The substitution of Ti^{4+} by smaller Al^{3+} cations reduces unit cell dimensions of the NaSICON framework and enhances ionic conductivity by about three orders of magnitude ($4x10^{-3}$ $S.cm^{-1}$).[40] However, despite the high ionic conductivity, LATP like LLTO is also electrochemically unstable with respect to Li.

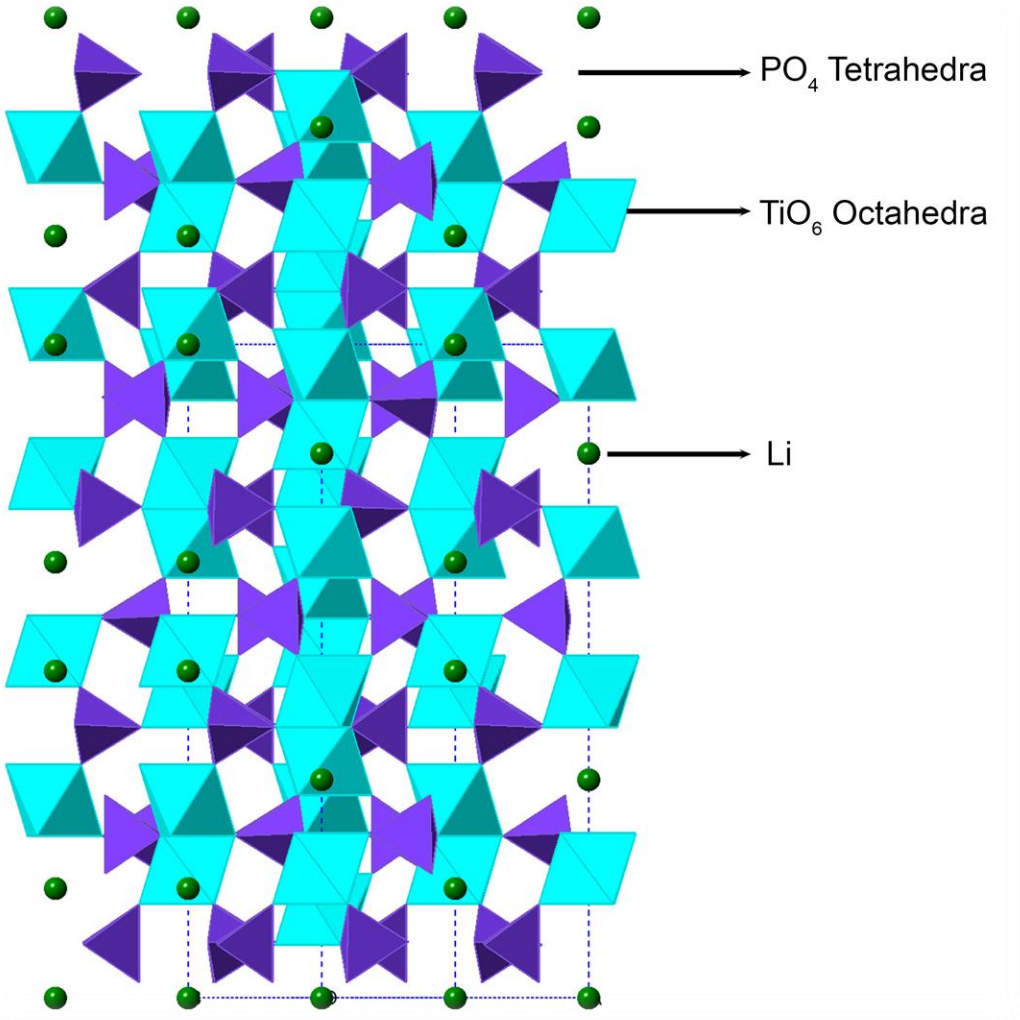

Figure 1.5. Crystal structure of $Li_2Ti_2(PO_4)_3$ based on the rhombohedral NaSICON structure. Green spheres represent possible Li sites. Dark and light blue are the P and Ti atomic sites, respectively.

1.6.2.3 LiSICON and thio-LiSICON-Type

LiSICON with the $Li_{14}Zn(GeO_4)_4$ composition was first introduced by Hong et al. (Figure 1.6).[41] The LiSICON structure is comprised of corner-sharing tetrahedra that contains two interstitial sites occupied by Li^+ ions in the range $-0.36 < x < +0.87$ for $Li_{2+2x}Zn_{1-x}GeO_4$.[42] These occupied interstitial sites are the basis for ionic conduction. $Li_{14}ZnGe_4O_{16}$ exhibits ionic conductivity of 0.13 $S.cm^{-1}$ at 300°C. However, LiSICON-type compounds based on oxides have much lower ionic conductivity in comparison with other type of Li-ion conductors at room temperature ($3x10^{-7}$ $S.cm^{-1}$). The lower ionic conductivity at lower temperature can be explained by the trapping of mobile Li ions in the immobile sublattice via the formation of defect complexes.[43]

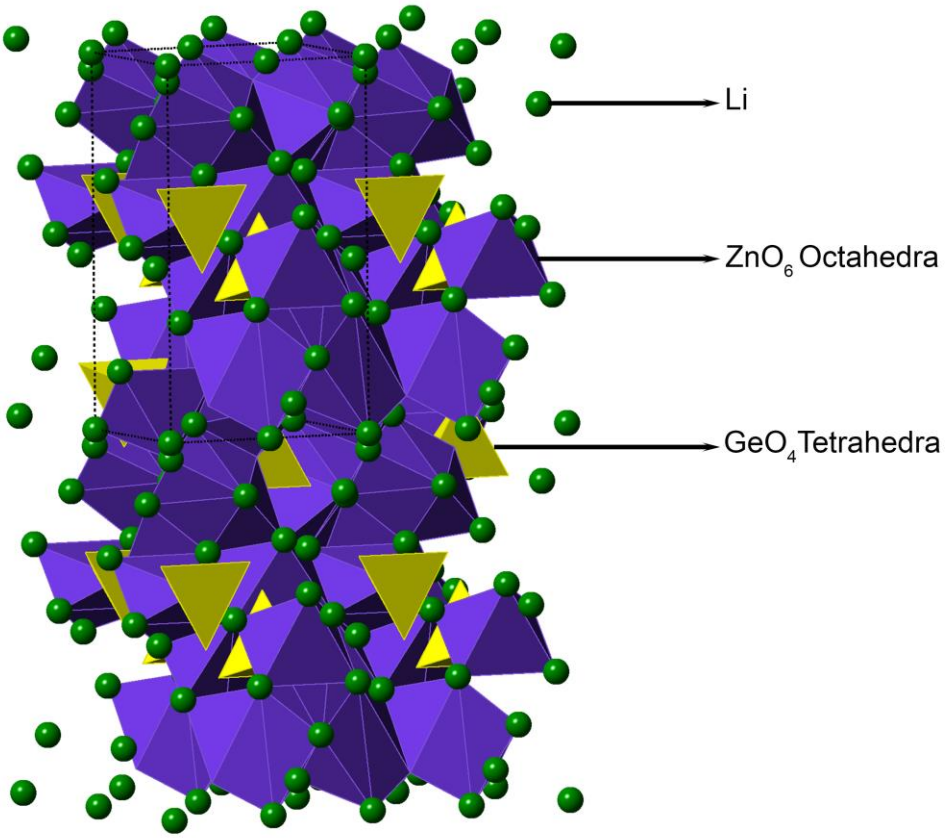

Figure 1.6. $Li_{14}Zn(GeO_4)_4$ with LiSICON crystal structure. Green spheres represent the possible Li sites. Dark blue and yellow Zn and Ge polyhedra**.**

1.6.2.4 Garnet-Type

A new family of Li-ion conductors with the general structural formula of $Li_5La_3M_2O_{12}$ (M= Ta^{5+}, Nb $^{5+}$) have been discovered by Hyooma *et al.*[44] The initial work on $Li_5La_3Ta_2O_{12}$ and $Li_5La_3Nb_2O_{12}$ identified these materials as promising candidates with a total ionic conductivity of $4x10^{-5}$ $S.cm^{-1}$.[45] Later, in 2007 Murugan *et al.* reported a new formulation of a garnet electrolyte with nominal composition $Li_7La_3Zr_2O_{12}$ (LLZO) and higher total ionic conductivity in the order of 10^{-4} $S.cm^{-1}$ (Figure 1.7).[46] For the case of LLZO two polymorphs of tetragonal and cubic symmetry exist.[47] The cubic LLZO polymorph has the highest ionic conductivity,[48] whereas the tetragonal polymorph conductivity is two orders of magnitude lower.[49] Thus, the cubic polymorph of LLZO is preferred over the tetragonal phase. The current generation of garnet electrolytes uses elements such as La, Ta, Al and Zr that are electrochemically stable with metallic Li. Thus, LLZO could enable the use of metallic Li anodes. The combination of high ionic conductivity and electrochemical stability with metallic Li has inspired new investigations into the fundamental properties of the garnet-type solid-state electrolytes.

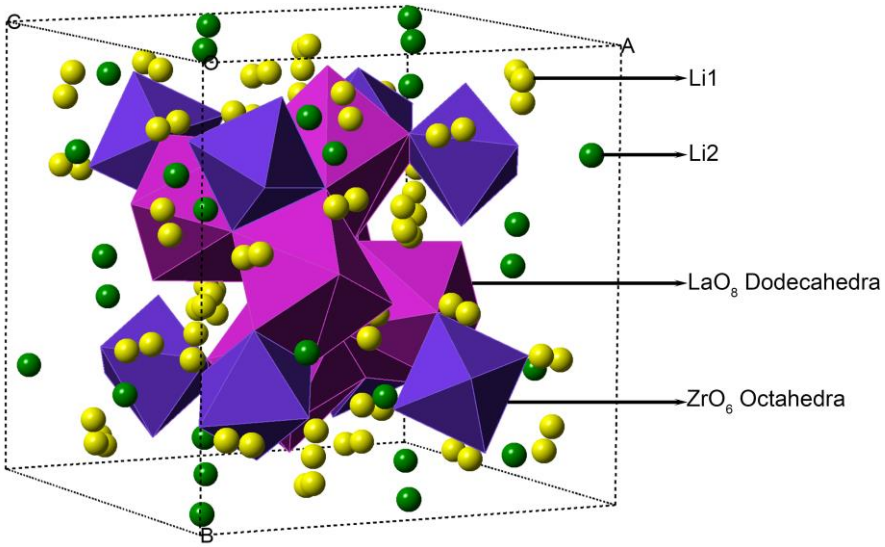

Figure 1.7. The crystallographic structure of cubic LLZO-Garnet consists of a skeleton framework of stable oxide polyhedra (La and Zr) permeated by a percolative network of mobile cations and vacancies.

A summary of the SSE discussed and their key parameters are listed in Table 1.2. The key features are high ionic conductivity on the order of 10^{-4} S.cm^{-1} at room temperatures and stability against metallic Li. As mentioned above, several SSE such as perovskite and NaSICON-type have demonstrated high ionic conductivity, however are not stable against metallic Li. Therefore, they are unable to meet the overall requirements needed for their use against metallic Li. On the other hand, the family of garnet-type SSE has drawn significant attention due to their combination of high ionic conductivity ($1x10^{-3}$ S.cm^{-1} at 298K),[50] and stability against metallic Li.[51] It is worth noting that stability against metallic Li also includes the stability toward Li dendrite initiation during cycling. Monroe *et al*. proposed a mathematical model to predict the electrochemical stability of SSE against metallic Li dendrite penetration.[52] Monroe *et al.* proposed approximately twice the shear modulus of metallic Li (4.2 GPa) is required for a SSE to suppress dendrite initiation. Thus, the shear modulus has been defined as another important criterion for selection of promising SSE candidates. It has been shown that LLZO has adequate shear modulus (61 GPa) to suppress Li dendrite penetration according to the Monroe *et al.* predictive model.[53-54] While these features suggest that garnet is a very promising SSE, additional research and development is needed for translation from the lab into viable technology.

This study proposes that LLZO garnet-type material is a promising SSE candidate for its use in SSB. Although LLZO SSE is expected to be compatible with metallic Li and enable the increase in high energy density, several key technical challenges remain. In the following sections, fundamental and applied aspects related to the integration of LLZO into SSB will be discussed.

Table 1.2. Summary of Li-ion solid electrolyte materials.

Electrolyte Type	Conductivity ($S.cm^{-1}$)	Advantages	Disadvantages
Polymer[55] (polyethylene oxide)	10^{-4} (65-78ºC)	• Stable with Li metal • Flexible • Easy to produce a large-area membrane	• Limited thermal stability • Low oxidation voltage (<4V)
LiPON[28-29]	10^{-6}	• Stable with Li metal • Stable with cathodes	• Difficult to scale up.
Perovskite[36]	$>10^{-3}$	• High electrochemical stability	• Not stable against Li metal • Brittle • High grain boundary resistance
NaSICON[39, 56]	10^{-3}	• High electrochemical stability • Suitable for high voltage solid electrolyte	• Not stable against Li metal • Brittle • High grain boundary resistance
Thio-LISICON[42]	10^{-4}-10^{-3}	• Low grain-boundary resistance	• Low oxidation stability • Sensitive to moisture • Poor compatibility with cathode materials
Garnet[44, 46]	10^{-3}	• Stable with Li metal • Low grain-boundary resistance • Can be synthesized in air	• High temperature processing required

1.7 Research hypothesis

LLZO is a promising SSE to enable batteries employing metallic Li anodes, but there is a need for comprehensive kinetic characterization of the charge/discharge behavior. Moreover, the lack of fundamental understanding of the factors controlling the high interfacial resistance and maximum tolerable current density (critical current density, CCD) impede the translation of this technology into viable commercial battery. Acquiring a fundamental understanding of the underlying mechanisms that control each of these aspects could guide future efforts to further accelerate the development of solid-state electrolytes and their integration into SSBs for their use in EVs.

The overarching scientific hypothesis of this thesis is that *atomistic and microstructural defects such as porosity, grain boundaries, interfaces, and surface impurities govern the stability against Li dendrite propagation in polycrystalline LLZO and consequently control the maximum tolerable current density (critical current density, CCD)* (Figure 1.8). Thus, the goal of this work is to translate this fundamental knowledge into engineering strategies to enable the development of LLZO membrane technology capable of withstanding current densities relevant to the PHEV/EV drive cycle ($\geq$ 1 mA.cm^{-2}).

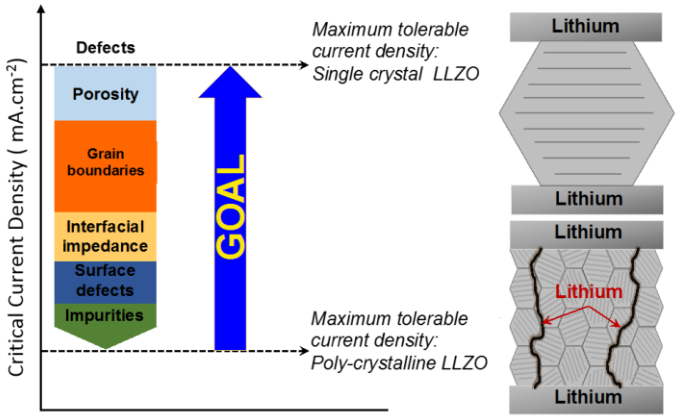

Figure 1.8. Defects in polycrystalline LLZO will reduce the critical current density. Above the critical current density, Li metal propagates toward the counter electrode.

1.8 Thesis goals

There are a few reports in literature that elucidate the fundamental operation of the Li-LLZO interface. This thesis focuses on the details of surface chemistry and microstructure to address the major challenges in the development and use of LLZO to enable metallic Li. The overall goal of this thesis is multi-pronged: first, to understand the Li-LLZO interface stability and kinetics and second develop methodologies to engineer the Li-LLZO interface and LLZO microstructure to improve the stability, especially at high current density (Figure 1.9).

1.8.1 Understanding the origin of high interfacial impedance

Recent reports determined that the Li-LLZO interfacial impedance was in the hundreds of $\Omega.cm^2$ at room temperature, which is significantly higher compared to conventional LIBs (10-100 $\Omega.cm^2$ total cell impedance at room temperature).[57-59] The origin of this high interfacial ristance is not understood and requires more investigation. This thesis aims to clarify the effects of relative humidity and air exposure time with changes in LLZO surface chemistry and Li–LLZO interfacial impedance using a combination of computational modeling and experimental measurements.

1.8.2 Enabling stable and low impedance Li-LLZO interfaces

Achieving stable and low interfacial impedance is crucial to improve the electrochemical performance of SSBs. By understanding the origin of interfacial impedance, strategies to reduce it can be developed. If a stable and low-impedance Li-LLZO interface can be achieved, evaluation of the Li metal penetration phenomenon is made possible.

1.8.3 Understanding mechanisms governing the maximum tolerable current density in LLZO

Cycling the Li-LLZO interface >~0.2 $mA.cm^{-2}$ typically results in cell short-circuiting.[59-63] The purpose of this thesis is to conduct detailed experimental and theoretical investigations to

understand the role that defects play in governing the stability and transport through the Li-LLZO interface and in LLZO. This dissertation emphasizes microstructural defects and surface chemistry and how they affect the CCD. To this end, novel ceramic processing technology was developed to precisely control the microstructure and surface chemistry to enable correlation between mechanical and electrochemical behavior.

The knowledge gained could facilitate the development of polycrystalline LLZO membrane technology that can sustain current densities approaching the values for defect-free single crystals.

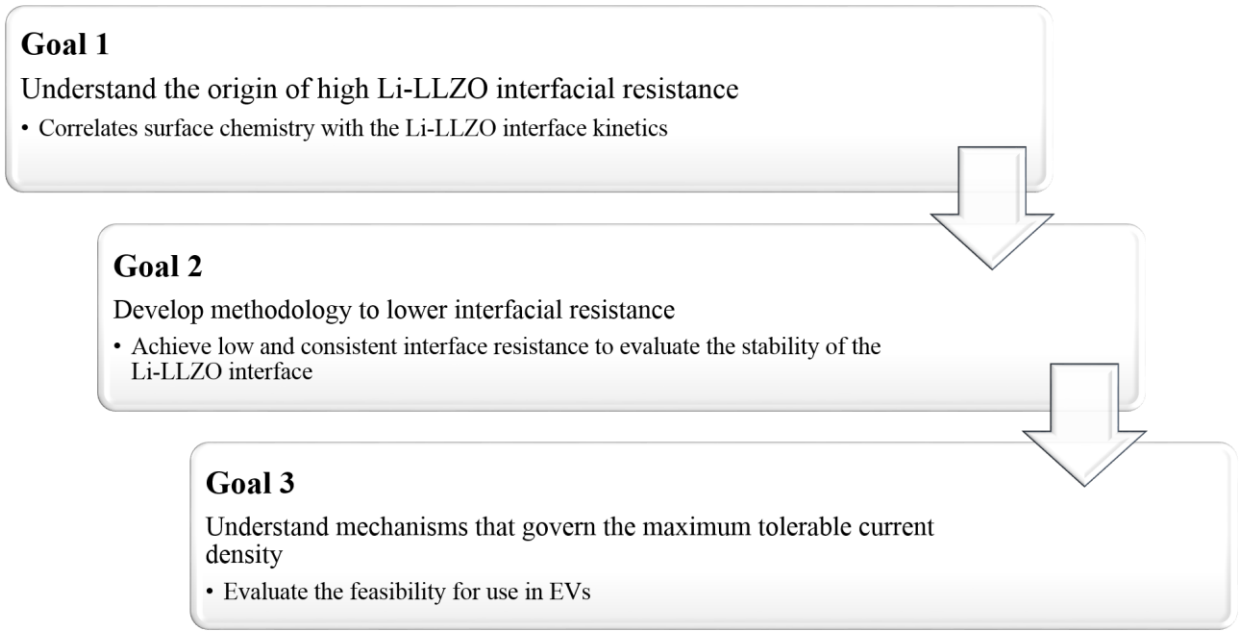

Figure 1.9. The three main goals of this thesis.

CHAPTER II

Experimental methods

2.1 Introduction

$Li_7La_3Zr_2O_{12}$ (LLZO) is considered a promising solid-state electrolyte (SSE) due to its high ionic conductivity and stability against metallic Li. However, LLZO has two polymorphs; the tetragonal phase ($I4_1/acd$ space group) and cubic phase ($Ia\bar{3}d$ space group).[64] Tetragonal-LLZO (*t*-LLZO) has lower ionic conductivity $1.6x10^{-3}$ – $2.3x10^{-2}$ $mS.cm^{-1}$,[65-66] whereas cubic-LLZO (*c*-LLZO) offers two orders of magnitude higher ionic conductivity 0.5 - ~1.0 $mS.cm^{-1}$, hence the challenge is stabilizing *c*-LLZO. The tetragonal garnet structure is the thermodynamically stable phase of LLZO containing stoichiometric Li (7 moles per formula unit LLZO). However, by introducing supervalent cations such as Al or Ga for Li and Nb and Ta for Zr,[50, 58, 60, 67-69] the Li sub-lattice goes through an order-disorder transition and relaxes into *c*-LLZO. Experimental studies verified by computation suggested that a critical Li vacancy concentration in a range of 0.4-0.5 per LLZO formula unit is required to stabilize the cubic phase.[70] For example, Geiger *et al.* synthesized LLZO garnet in an alumina crucible and determined that Al originating from crucible stabilized *c*-LLZO.[67] In this case, the substitution of Li^+ by Al^{3+} in the 24d site produces Li vacancies to maintain charge neutrality according to Kroger-Vink notation ($Al_{Li}^{\cdot\cdot}=2V_{Li}^{\prime}$). In addition to stabilizing the cubic phase, the existence of higher Li vacancies enhances Li-ion mobility, which results in higher ionic conductivity.

Similarly, Rangasamy *et al.*, established the critical Al concentration to stabilize the cubic phase as 0.24 mole resulting in ~ 0.48 mole of vacancies per LLZO formula unit.[50]

In this thesis, LLZO with the nominal composition of $Li_{6.25}Al_{0.25}La_3Zr_2O_{12}$ was studied based on its potential to enable membrane technology exhibiting the unique combination of room temperature high Li-ion conductivity, and stability against metallic Li. Addition of 0.25 mole Al controlled the amount of Li content and vacancies to achieve *c*-LLZO. A brief overview of the experimental procedures involved in synthesizing *c*-LLZO powder with high purity and rapid induction hot-pressing (RIHP) densification will be discussed. An example of processing is given by correlating the hot-pressing temperature with the electrochemical behavior.

2.2 Experimental

2.2.1 Synthesis, and powder processing

Cubic Al-doped LLZO with the nominal composition $Li_{6.25}Al_{0.25}La_3Zr_2O_{12}$ was prepared using a solid-state synthetic technique. Li_2CO_3 (1 µm, Alfa Aesar, Ward Hill, MA), $La(OH)_3$ (1 µm, Alfa Aesar, Ward Hill, MA), Al_2O_3 (0.05 µm, Mager Scientific Inc., Dexter, MI), and ZrO_2 nanopowder (30-60 nm, Inframat, Advanced Materials, Manchester, CT) were weighed in appropriate ratios. 0.25 mole of Al was added to stabilize the cubic phase at room temperature. Additionally, 5 wt.% excess Li was added to the mixture to compensate for Li loss during calcination to avoid formation of the Li deficient phase known as pyrochlore ($La_2Zr_2O_7$).[50, 71] The powder mixture was thoroughly mixed with a planetary ball mill (PM 100; Retsch, Haan, Germany) in an agate jar (500 ml) and 45 agate balls of 10 mm diameter for 8 hours at 350 rpm. To maintain the temperature during mixing, the precursors were mixed in a sequence consisting of 5-minutes of milling followed by 5 minutes of rest. This sequence was repeated for 48 cycles. The powder mixture was collected and cold-pressed into 25.3 mm diameter pellets using a

stainless-steel die (MTI Corporation, Richmond, CA) with 8000 N force for 2 min. The cold-pressed pellets were placed in a tube furnace (Carbolite LTD, Derbyshire, UK) and calcined at 1000^{o}C for 4 h under 2 L.min^{-1} flowing dry air (<3 ppm moisture, Cryogenic Gases, Detroit, MI). The calcination was carried out in MgO boats to prevent adventitious doping of the LLZO. Figure 2.1 shows a schematic of the solid-state synthesis procedure as explained above. After calcination, the pellets were manually ground using an agate mortar and pestle. The ground powders were passed through a 75 µm sieve to obtain a consistent particles size distribution. After grinding and sieving, the calcined powder was characterized with X-ray diffraction (explained in characterization section) to evaluate the phase purity.

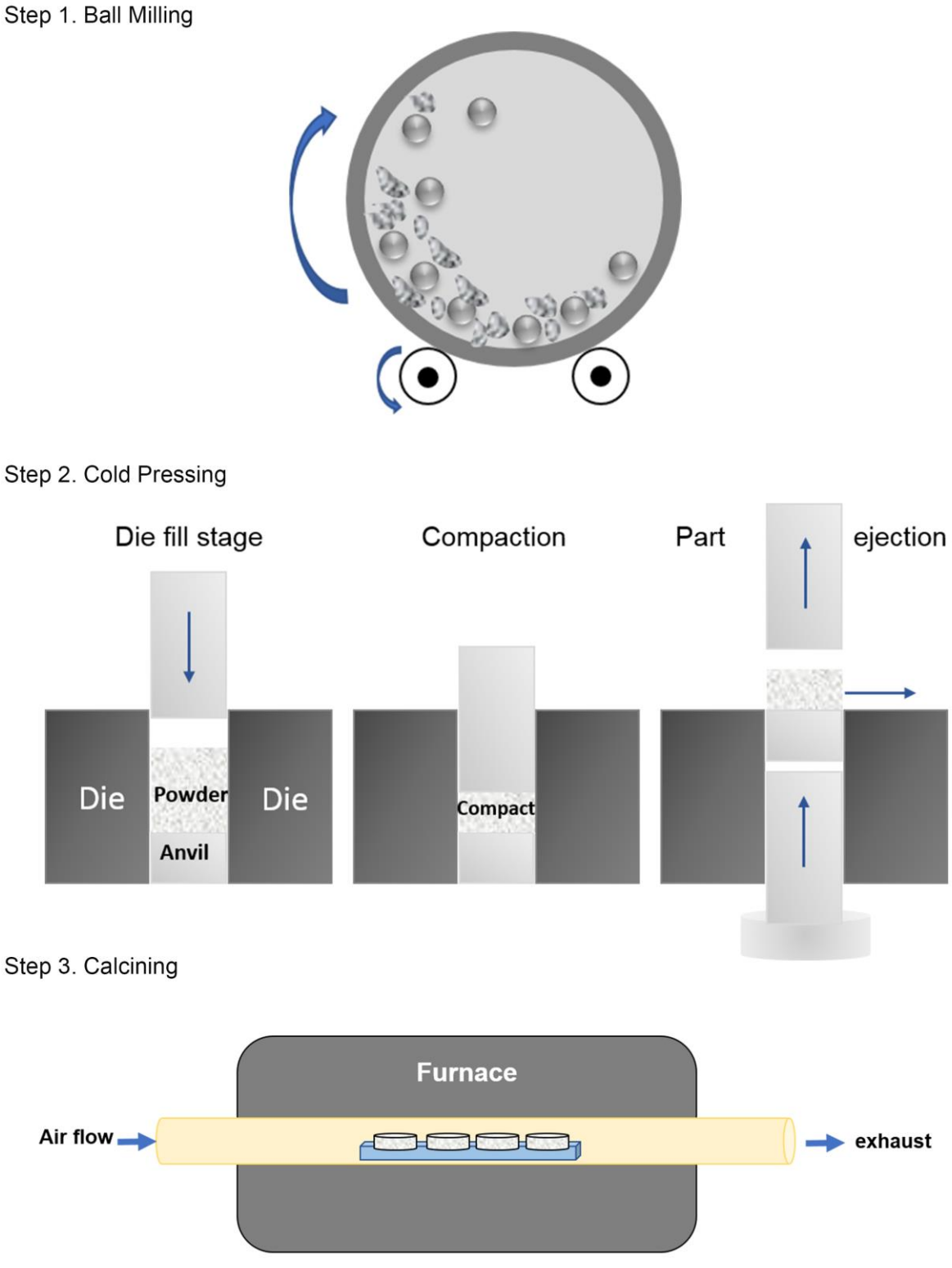

Figure 2.1. A schematic illustration of the solid-state synthesis procedure utilized for the preparation of garnet-type powder**.**

2.2.2 Powder densification

To use LLZO as a SSE membrane, the powder must be densified into a rigid, monolithic body. The driving force for densification is the reduction of surface energy, which results from the elimination of solid-vapor interfaces and the creation of grain boundaries between particles. For densification to occur, the interparticle area should increase by neck growth, followed by solid-state diffusion toward pores that are coincident with grain edges. Consequently, vacancies should transport away from the pores to a sink such as grain boundary. Typically, factors such as temperature, time, and green density (density of compacted powder), control sintering kinetics. Table 2.1 summarizes the effect of each parameter.

Table 2.1. Factors affecting solid-state sintering

Factors	Effects
Time	Longer times at temperature increase density
Temperature	Higher temperature enhances sintering kinetics and bulk diffusion
Green density	Higher green density typically results in higher final density
Green microstructure uniformity	Eliminating agglomerates in the green body results in better densification

The simultaneous application of temperature and pressure can also enhance densification. If the applied pressure is uniaxial, the process is referred to as hot-pressing, whereas if the pressure is applied isostatically, the process is referred to as hot-isostatic pressing. The application of pressure causes a net flux of vacancies from the neck to the grain boundaries and leads to densification. In addition, hot-pressing can be advantageous in reducing Li loss since densification is accelerated compared to conventional pressure-less sintering.

When hot-pressing, the powder is loaded in a die, heated and pressed for several minutes to several hours. In this thesis, rapid induction hot-pressing (RIHP) was used to achieve high relative densities. RIHP relies on the unique characteristics of induction heating through radio

frequency coupling. A basic RIHP apparatus is shown in Figure 2.2; a radio frequency power supply sends an AC current through an inductor which is often a copper coil to heat a work piece or susceptor (graphite or metal die) that resides in the inductor. In this process, as shown schematically, there is no direct contact between the inductor and the susceptor/die. In the next section, the effect of hot-pressing parameters on the microstructure, density and ionic conductivity of LLZO will be shown.

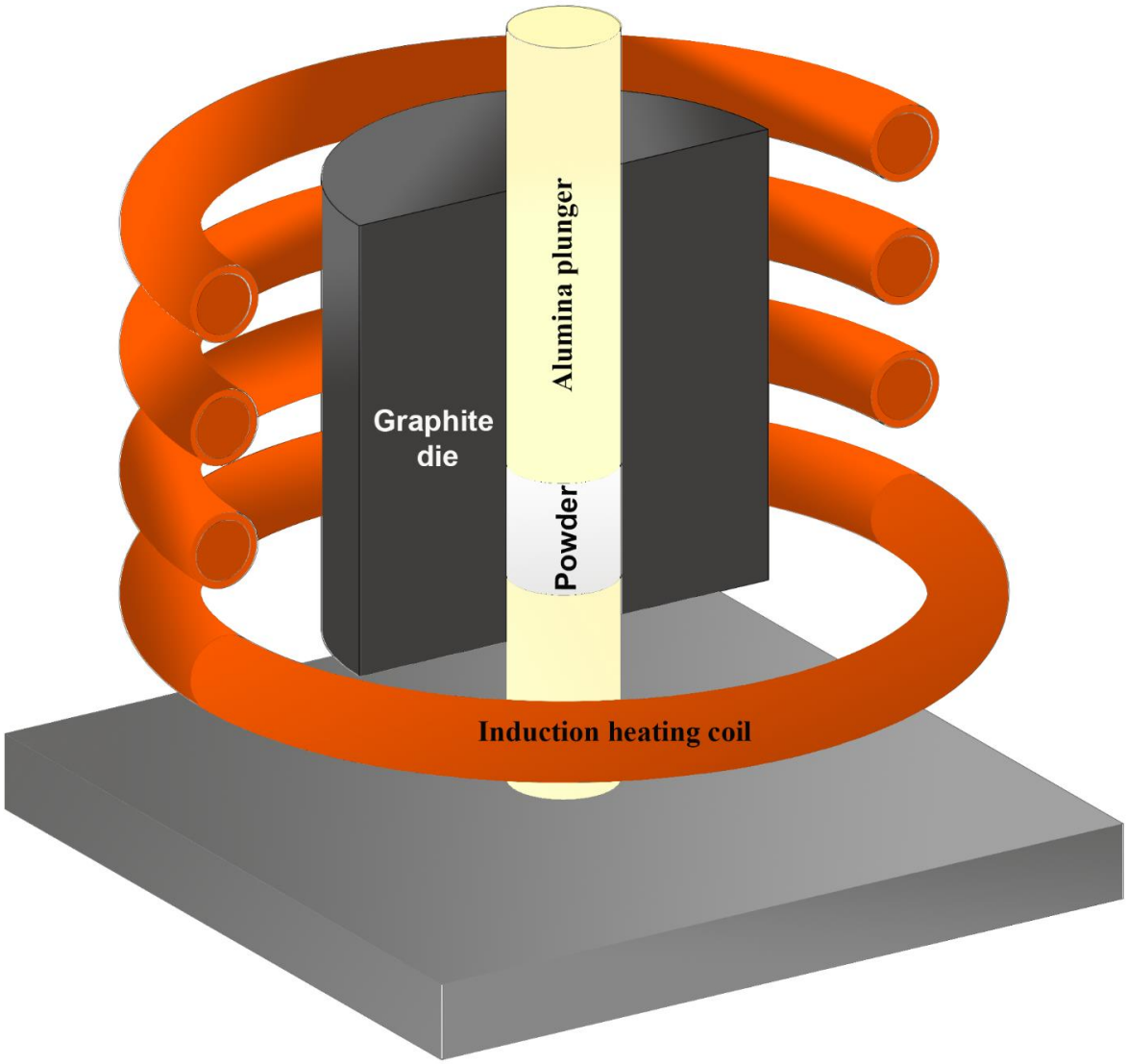

Figure 2.2. Schematic of the cross-section of a graphite die with powder for the hot-pressing using rapid induction hot-pressing technique.

2.2.2.1 Rapid induction hot-pressing (RHIP)

The LLZO powders were hot-pressed into pellets with 12.7 mm diameter using rapid induction hot press (RIHP, Across International, Livingston NJ) in a graphite die under argon flow. To evaluate the effect of temperature on the microstructure and relative density of LLZO, a constant pressure of 62 MPa was used while the RIHP temperature was varied between 900ºC-1300ºC in 50ºC increments. For all hot-pressing, the maximum temperature was reached within 5 minutes and held for 1-4 h and cooled down at 5 C.min^{-1}. The hot-pressed pellets were cut into 1± 0.2 mm thick disks using a diamond saw in mineral oil (Buehler, Lake Bluff, IL). Disks were polished using 400 and 600 grit sandpaper (Norton Abrasives, Worcester, MA) using a lapping fixture (South bay Technologies, San Clemente, CA) to ensure both faces were parallel. After grinding, the LLZO disks were transferred to an argon-filled glovebox with <0.1 ppm oxygen. The process flow chart for LLZO synthesis and densification is shown in Figure 2.3.

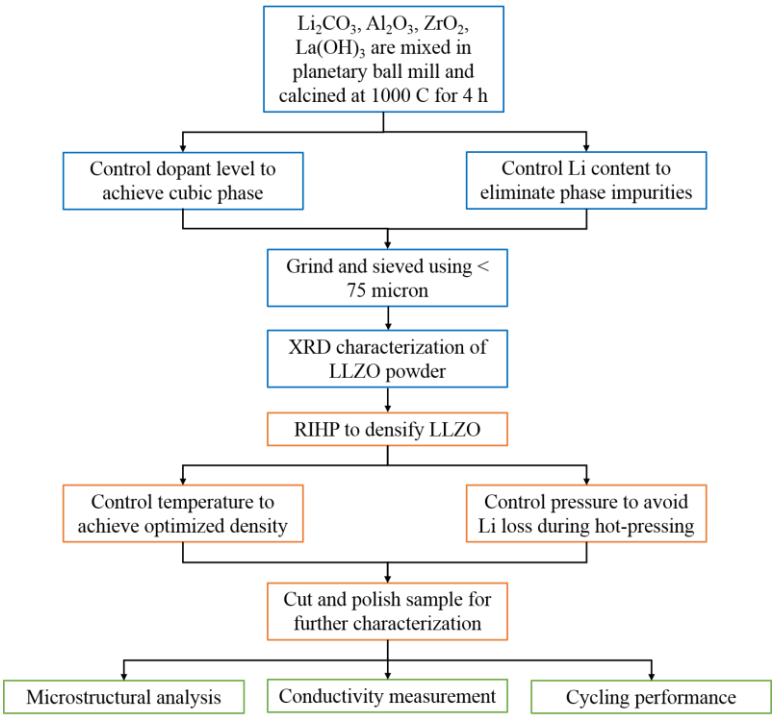

Figure 2.3. Process flow chart for LLZO synthesis (blue) and densification (orange), characterization (green**).**

2.2.3 Density measurements

The density of each hot-pressed pellet was determined by measuring the mass and its geometric volume (Density = mass/volume). The relative density of each hot-pressed pellet was measured by dividing the geometrical density with the theoretical density (5.17 $g.cm^{-3}$). If impurities are present, the theoretical density ($\rho_{theoretical}$) can be calculated using the rule of mixtures in Equation 1:

$$\frac{1}{\rho_{theoretical}} = \sum \frac{W_i}{\rho_i} + \frac{W_m}{\rho_m} \quad (1)$$

where q_i is the density of secondary phase i, W_i is the weight fraction of secondary phase i, q_m is the density of the matrix (LLZO), and W_m is the weight fraction of the matrix (LLZO).

2.2.4 Phase purity analysis

The phase purity of the synthesized LLZO powder and hot-pressed pellets were determined using X-ray diffraction (XRD, Rotating Anode X-Ray Diffractometer, Rigaku, Tokyo, Japan) with Cu K_α radiation (λ=1.54 Å) over a range of 15º to 65º 2θ and a 0.02º step width. The analysis of X-ray diffraction patterns was carried out using Bragg's law and Jade software (Equation 2):

$$n\lambda = 2d\ sin\theta \quad (2)$$

where n is an integer (1, 2, 3, ...), λ is the wavelength of the incident beam, d is the interatomic spacing, and θ is the angle of the diffracted beam. This equation is used to create an XRD pattern that plots intensity as a function of 2θ. Rietveld structural refinements of the XRD patterns were performed to determine the weight fraction of secondary phases.

2.2.5 Microstructural analysis

The microstructure of the hot-pressed pellets was examined by cross sectional analysis on fracture surfaces using scanning electron microscopy (SEM, a FEI Nova 200 Nano lab Dualbeam SEM microscope at accelerating voltage 10 kV).

2.4.4 Electrochemical impedance spectroscopy

The effect of porosity on the ionic conductivity and contribution of bulk and grain boundary in total resistivity of hot-pressed pellets was evaluated using electrochemical impedance spectroscopy (EIS) between 1 Hz to 7 MHz using a 100 mV perturbation amplitude (VMP300, Bio-Logic, Knoxville, TN). Gold was sputtered on each face of the hot-pressed pellet as a blocking electrode.

Equivalent circuit modeling was used to separate the bulk and grain boundary resistivity. First, each data set was normalized to the geometric dimensions as shown in Equation (3):

$$\rho = R \times \frac{A}{l} \quad (3)$$

where R is the resistance (Ω), A is pellet area (cm^2), l is the thickness of pellet (cm) and ρ is the resistivity of the pellet (Ω.cm). The modified equivalent circuit model developed by Huggins was used for modeling the data (Figure 2.4).[72] In this model, a constant phase element (CPE = $\frac{1}{Q(j\omega)^{\alpha}}$) was used to account for any dispersion in the time constant. The values for a CPE should be in the range of 10^{-12} $F.cm^{-2}$ for the bulk and 10^{-9} $F.cm^{-2}$ for the grain boundaries.[73] The ideality of the CPE is represented by the coefficient α. The data fitting and circuit modeling was done with a software package EC-Lab V10.44.

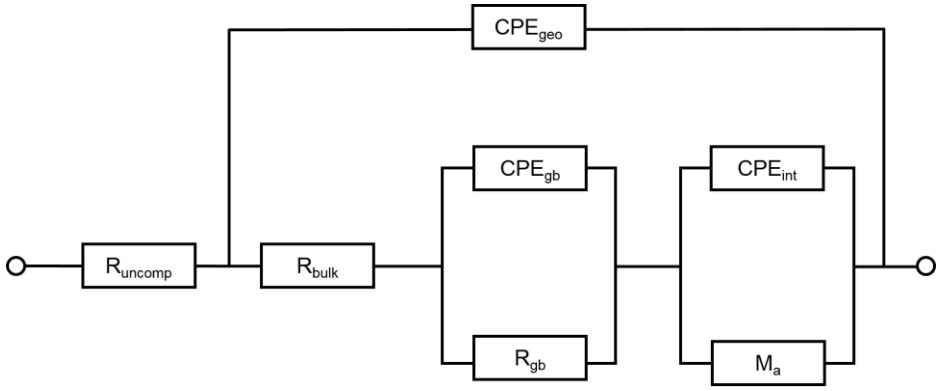

Figure 2.4. The equivalent circuit model used to model the EIS data. R and CPE represent resistors and and constant phase elements.

2.3 Results and discussion

2.3.1 Phase purity

The XRD patterns of the LLZO powder, hot-pressed LLZO pellet at 1100°C hot-pressing temperature and the reference pattern for cubic LLZO are shown in Figure 2.5. A comparison of the XRD patterns for calcined powder and hot-pressed pellet with that for the reference cubic LLZO suggests that pellets were predominantly cubic LLZO with no observable second phases such as pyrochlore ($La_2Zr_2O_7$).

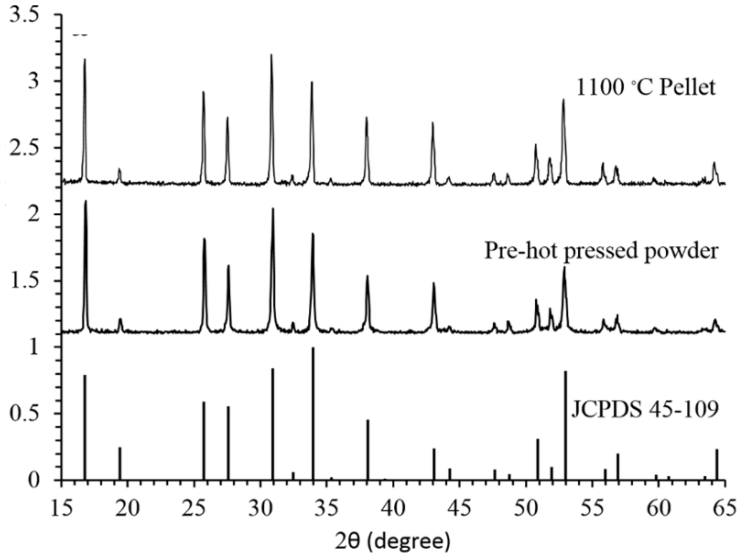

Figure 2.5. X-ray diffraction patterns of $Li_{6.25}Al_{0.25}La_3Zr_2O_{12}$ calcined powder and hot-pressed pellets pressed at 1100°C.

2.3.2 Microstructure

The microstructural evaluation and fracture surfaces of all hot-pressed LLZO pellets along with SEM images of initial powder are shown in Figure 2.6. From SEM images in Figure 2.6, several observations can be made. First, increasing the hot-pressing temperature reduced the porosity and hence increased the density. Second, a transition from intergranular to intragranular fracture was observed by increasing the hot-pressing temperature and relative density of LLZO pellets. At the highest relative density of 98.6%, for LLZO pellet hot-pressed at 1100C (Figure 2.6f), the fracture mode was almost entirely intragranular. This is an indication of improved grain-to-grain adhesion in pellets with higher relative density. Third, Figure 2.6f indicates LLZO can be consolidated to high theoretical density without the use of a sintering aids. As expected, increasing the hot-pressing temperature increased the relative density (Table 2.2). In general, hot pressing at 1050 and 1100°C yielded higher relative density.

Table 2.2 Summary of microstructural evolution as a function of RIHP temperature.

Temperature℃	900	950	1000	1050	1100
Relative density (%)	80	85	92	95	98.6

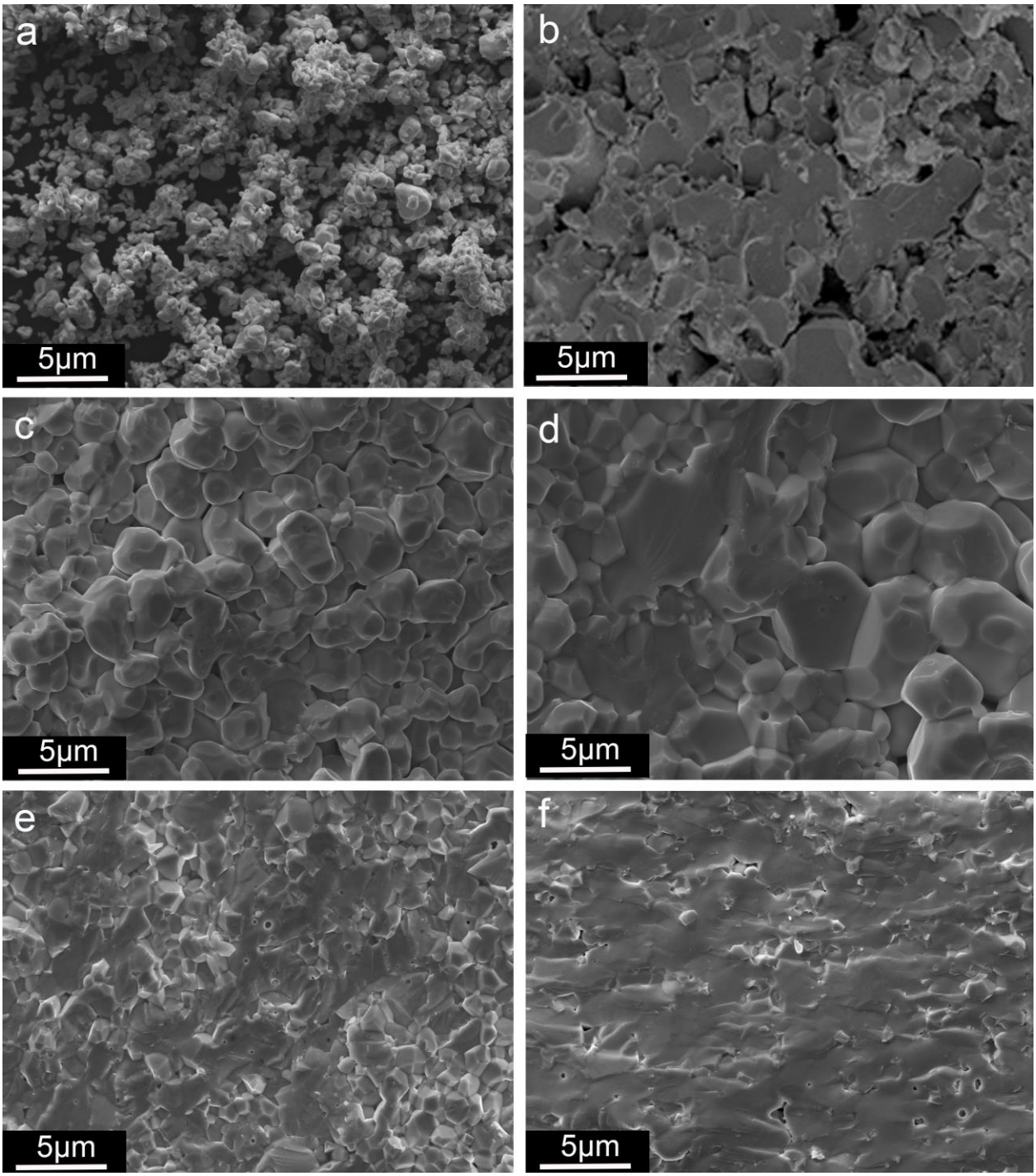

Figure 2.6. Secondary electron SEM images of: a) as calcined LLZO powder, and fracture surfaces of LLZO hot-pressed at different temperatures: b) 900°C (RD= 80%), c) 950°C (RD= 85%), d) 1000°C (RD=92%), e) 1050°C (RD=95%), and f) 1100°C (RD=98.6%).

2.3.3 Electrochemical impedance spectroscopy

Electrochemical characterization EIS was conducted on all the hot-pressed pellets to evaluate the effect of the microstructure and relative density on the ionic conductivity. Figure 2.7 shows the Nyquist plot of EIS data at room temperature for all LLZO hot-pressed between 900-1100ºC. The Nyquist plots can be separated into three distinct regions:

1) The bulk resistivity at higher frequencies
2) The grain boundary resistivity in the mid frequency regime
3) Vertical tail related to Li-ion blocking electrode behavior in the lowest frequency regime

The results of the impedance data fitting including Q and α values and the contribution of grain boundary resistance, bulk, and total ionic conductivity is summarized in Table 2.3. The total ionic conductivity is a sum of the bulk and grain boundary contribution.

From the results presented in Figure 2.7 and Table 2.3, it is apparent that the contribution of the grain boundary resistance is lower as the hot-pressing temperature is increased. For LLZO pellets hot-pressed at higher temperature (T>1050 °C), the bulk and total conductivities are similar. This is expected since the higher hot-pressing temperature leads to higher relative density with higher grain-to-grain adhesion, thus the contribution of grain boundary resistance is significantly lower for LLZO with higher relative density. It is worth noting that the Q and α values for the grain boundary and bulk transport are relatively consistent with the values expected for LLZO with higher relative density. However, the Q and α values are deviating from the ideal values for lower density pellets, which could be correlated to the fact that grains are not as well connected when hot-pressing at lower temperature.

The reduction of grain boundary resistance has been observed here by increasing the hot-pressing temperature under a constant load. The higher hot-pressing temperature increases the

grain-to-grain adhesion leading to lower grain boundary resistance. The total ionic conductivity of hot-pressed LLZO as a function of RIHP temperature and relative density is shown in Figure 2.7f. This trend is associated with the observed decrease in grain boundary resistance in this study and it is consistent with previous data reported by David *et al*.[71] For LLZO with 80, 85, 92, 95, 98 % relative density, the total ionic conductivity was determined to be 0.009, 0.17, 0.31, 0.34 and 0.38 $mS.cm^{-1}$, respectively. These values are in good agreement with the values reported for Al doped LLZO.[46, 50, 71, 74] Based on the presented EIS data, it is apparent the LLZO pellet hot-pressed at 1100°C exhibited one of the lowest grain boundary resistance reported resulting in total conductivity nearly equal to the bulk conductivity.

Table 2.3. EIS data fitting for LLZO pellets hot-pressed between 900-1100 °C.

Sample	σ_{bulk}	Q_{bulk}	α_{bulk}	Q_{gb}	α_{gb}	σ_{total}
900°C	0.009	$2.8x10^{-11}$	0.81	$5.8x10^{-8}$	0.75	0.005
950°C	0.17	$1.4x10^{-11}$	0.97	$4.8x10^{-8}$	0.81	0.12
1000°C	0.31	$0.8x10^{-11}$	0.91	$3.8x10^{-8}$	0.98	0.27
1050°C	0.34	$1.6x10^{-11}$	0.99	$1.5x10^{-8}$	1	0.33
1100°C	0.39	$1.8x10^{-11}$	1	$1.9x10^{-8}$	1	0.38

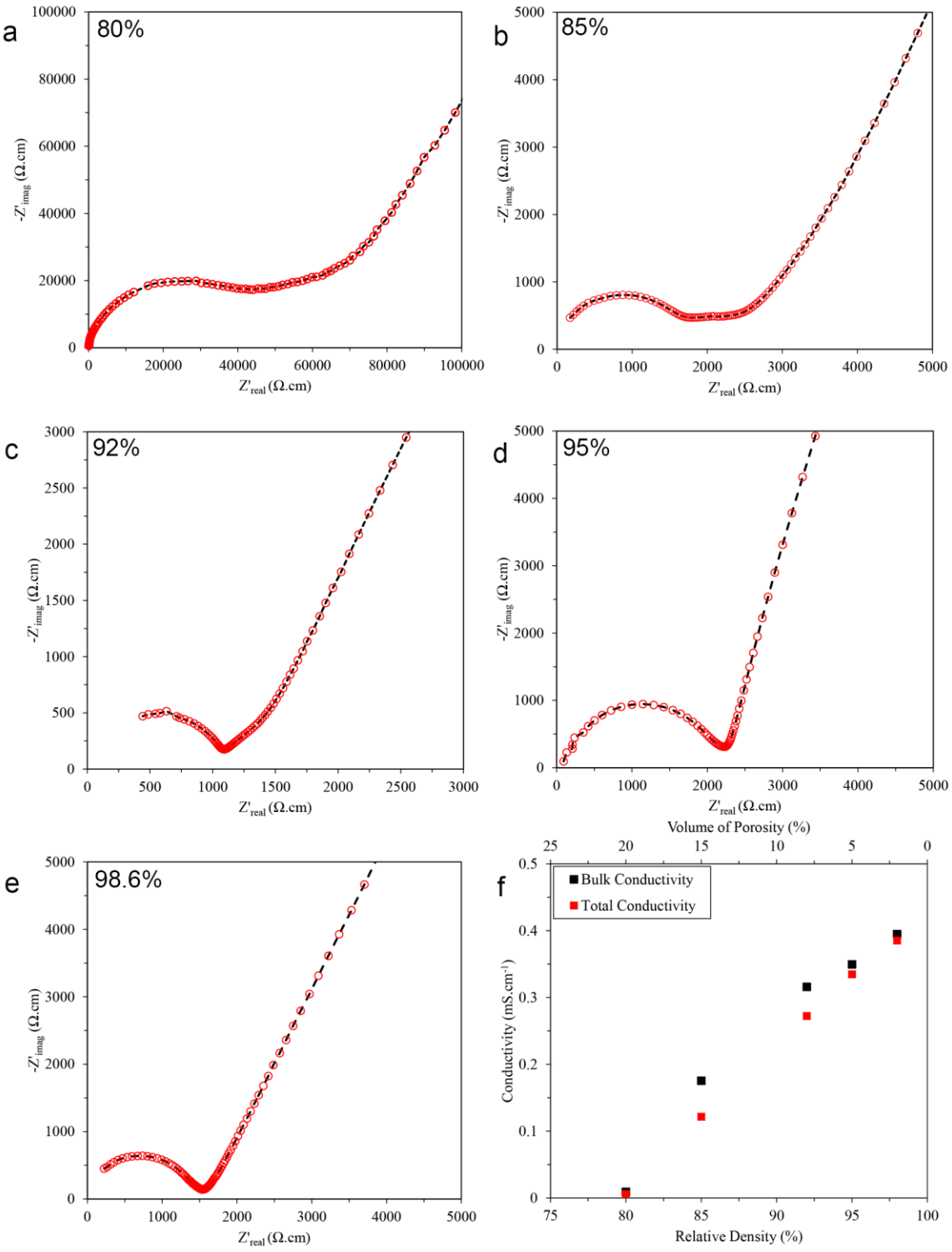

Figure 2.7. Electrochemical impedance spectroscopy plots of LLZO hot-pressed at different temperatures: a) 900°C, b) 950°C, c) 1000°C, d) 1050°C, and e) 1100°C. Markers indicate experimental data and the solid lines are simulated lines extrapolated from equivalent circuit modeling, and, f) the bulk, grain boundary and total resistivity as a function of RD%**.**

2.4 Conclusions

LLZO with the garnet structure is among the most promising SSE for its use in solid-state batteries. LLZO exists in a tetragonal and cubic polymorph, where the cubic phase exhibits around 2 orders of magnitude higher Li-ion conductivity. A critical Li vacancy concentration (0.4-0.5 per formula unit) is required to stablize the cubic phase of LLZO, which will be controlled by introducing dopants such as Al in the microstruture. In this study, the cubic Al-doped LLZO powder was prepared using a solid-state synthetic technique and it was densified using hot-pressing technique. Furthermore, a systematic study of the effect of hot-pressing temperature on the microstructure and Li-ion transport of Al-doped, cubic LLZO was performed. It was determined that hot-pressing at lower temperature ($T \leq 1000°C$) resulted in lower relative density and lower total ionic conductivty. On the other hand, the pellets hot-press at higher temperature between 1050°C and 1100°C had significantly higher relative densities and higher total ionic conductivities at room temperature. The higher ionic conductivities mainly resulted from the differences in grain-boundary resistance. Thus, LLZO with nominal composition of $Li_{6.25}Al_{0.25}La_3Zr_2O_{12}$ and hot-pressed at 1100°C with relative denisty ~98% was chosen for further investigatiions in the next chapters.

CHAPTER III

Characterizing the Li-$Li_7La_3Zr_2O_{12}$ interface stability and kinetics as a function of temperature and current density

3.1 Introduction

Li-ion battery technology has advanced significantly in the last two decades;[11, 23, 75] however, future energy storage demands will require safer, cheaper and higher performance electrochemical energy storage. While the primary strategy for improving performance has focused on electrode materials,[23] the development of new solid-state electrolytes (SSE) has been overlooked as a potential means to create a step change in energy storage performance and safety. Solid-state batteries (SSB) employing metallic Li anodes are an example of an advanced energy storage technology. Indeed, the role that SSE will play in enabling SSB is clear, but relatively few have been identified as promising candidates. Recently, zirconium-based garnet electrolyte, with the formulation $Li_{6.28}La_3Al_{0.3}Zr_2O_{12}$(LLZO), was reported to have the unique combination of high room temperature Li-ion conductivity, stability against metallic Li, and moderate stability in air.[46] It is believed that lanthia and zirconia form a chemically stable atomic framework that is not decomposed upon contact with metallic Li.[46, 76] The shear modulus is another important parameter that is used to predict the stability of the Li-SSE interface.[52] According to Monroe *et al*. the SSE must be approximately twice the shear modulus of metallic

Li (G_{Li} = 4.2 GPa)[77] to suppress Li dendrite initiation.[52] Ni *et al*. determined the shear modulus of LLZO to be 61 GPa using resonant ultrasound spectroscopy.[53] Likewise, according to the model developed by Monroe *et al*., LLZO exhibits a more than adequate shear modulus to suppress Li dendrite initiation.

Recently, Ohta *et al*. observed negligible capacity fade in an all solid-state Li-LLZO-$LiCoO_2$ cell after 100 cycles.[60] Kotobuki *et al.* also showed it is feasible to cycle a Li-LLZO-$LiCoO_2$ cell.[78] Conversely, Ishiguro *et al*. observed abrupt swings and a sudden drop in voltage during direct current (DC) polarization tests at $\geq$ 0.5 mA.cm^{-2} at room temperature.[62] Moreover, it is believed that the current density is an external variable that affects the on-set of short-circuiting. Although it was not confirmed with post-test materials characterization, it was suggested that the short-circuit could have resulted from Li dendrite formation and propagation.[61-62, 78]

Previously, Gibson *et al.* characterized the Na-sodium beta alumina (Na-SBA) interface behavior as a function of temperature.[79] It was determined that the interfacial resistance decreased with increasing temperature. In addition, Virkar *et al.* studied the effect of temperature on the maximum sustainable current density (or critical current density, CCD), associated with the initiation and propagation of Na metal dendrites, in Na-SBA and Na-NaSICON cells.[80] It was determined that the CCD significantly decreased below the Na melting temperature. We believe the observations made by Gibson *et al*. and Virkar *et al.* in Na-SBA cells may also be observed in Li-LLZO cells, i.e. the Li-LLZO interfacial resistance and stability should be strongly correlated to temperature.[79-80] Thus, the purpose of this work was to investigate the effect of temperature and current density on the stability and kinetics of the Li-LLZO interface. Owing to the complications in fabricating and operating molten Li anode cells, the maximum

cell temperature was kept below the Li melting point (180°C).[77] Electrochemical impedance spectroscopy (EIS) was used to study the individual resistive elements that comprise the total Li-LLZO-Li cell resistance. DC cycling was used to determine the CCD as a function of temperature (30 – 175°C). Additionally, post-test microscopy was used to observe the LLZO surface after cycling. The goal of this work is to better understand the Li-SSE interfacial stability at current densities relevant to vehicle electrification (> 1 $mA.cm^{-2}$).

3.2 Experimental

3.2.1 Powder synthesis and pellet processing of solid-state electrolyte

Cubic $Li_{6.25}La_3Zr_2Al_{0.25}O_{12}$ (LLZO) was prepared using a solid-state synthetic technique explained in chapter 2 section 2.3. The calcined powders were hot-pressed using a rapid induction hot-press technique at 1100°C for 1 hour under constant uniaxial 62 MPa pressure. In this study, the LLZO pellets were 1.00 ± 0.20 mm thick and 12.7 mm in diameter.

3.2.2 Materials characterization

Powder X-ray diffraction (Bruker, D8 DaVinci diffractometer equipped with CuK_α X-ray radiation) was used to characterize the LLZO phase purity before and after hot pressing. Cross sectional analysis was performed on fracture surfaces using scanning electron microscopy (Carl Zeiss EVO LS25), to characterize microstructural features such as porosity, grain boundary integrity, and grain size. After cycling, the cells were disassembled and the short-circuited LLZO was removed for analysis. SEM/FIB/EDS were performed on a FEI Nova 200 Nano lab Dualbeam SEM/FIB microscope (accelerating voltage: 0.2–30 kV (electrons), up to 30 kV (ions)) and on a FEI Helios Nanolab 650 Dualbeam SEM/FIB microscope (accelerating voltage: 50V–30 kV (electrons), 0.5 kV–30 kV (ions) beam current: 0.8 pA–26 nA (electrons), 0.1 pA–65 nA (ions). LLZO for SEM/FIB/EDS analysis were wet polished with a series of sand paper grits,

with a final polishing using a 1 mm diamond paste. A physical electronics Auger Nanoprobe 680 microscope (spatial resolution - 50 nm; energy resolution - 0.3% of the electron energy) was used to probe elements in LLZO. The cycled LLZO specimen was coated with a thin Au layer before SEM/EDS/AES analysis to increase electron conductivity.

3.3.3 Electrochemical characterization

To characterize the effect of temperature on Li-LLZO-Li cells, several procedures were developed to limit variability between cells. To maintain a consistent surface finish, all LLZO pellets were dry polished with 400 followed by 600 grit SiC sandpaper (Norton Abrasives) in an argon filled glovebox (0.1 ppm O_2 and 1 ppm H_2O). Solid-state symmetric cells were assembled by placing LLZO pellets between two Li foil (Alfa Aesar) disks. Li foil disks were scraped to remove the oxide layers on the surface. A custom load frame was built and instrumented with a load cell to apply and maintain 350 kPa of stack pressure. To prevent the Li anodes from short-circuiting along the LLZO pellet periphery while under pressure, 100 μm thick polytetrafluoroethylene (PTFE) washers with 12.7 mm outer diameter and 7.8 mm inner diameter were used. The open area in the PTFE washers reduced the contact area between Li and LLZO from 1.22 cm^2 to 0.48 cm^2 per face. The LLZO Ohmic and interfacial resistances (the Li-LLZO interfacial resistance normalized per unit area) at the Li-LLZO interface were characterized using electrochemical impedance spectroscopy (EIS) between 1 Hz to 7 MHz using a potentiostat/galvanostat (Bio-logic SP200). The measurements were conducted at various temperatures between 30 and 175°C. In this study, 175°C (just 5°C below melting point of metallic Li) was chosen as the maximum temperature because the use of molten Li would make the testing conditions more complex.

To characterize the effect of temperature on the critical current density, direct current (DC) cycling of Li-LLZO-Li symmetric cells was conducted between 30 and 160°C using the following procedure: (1) ten formation cycles (1 h per cycle) at +/- 10 μA.cm^{-2} at 175°C to ensure good contact between the Li electrode and the LLZO electrolyte, (2) reduce the temperature to various dwell temperatures ranging from 160°C down to room temperature (30°C) for galvanostatic cycling, and (3) galvanostatically cycle cells at various current densities (1 hour per cycle) with a rest period of 10 min between each current step.

3.3 Results and discussion

3.3.1 XRD and SEM analysis

The XRD patterns of the LLZO powder and pellet after hot pressing at 1100°C are shown in Figure 3.1a. After calcining and hot pressing, only single phase cubic LLZO was present. A representative microstructure of a LLZO fracture surface indicates the porosity was relatively low, which was consistent with the measured 97±1% relative density (Figure 3.1b). It is observed that the fracture mode was mostly transgranular; evidence of relatively high grain boundary adhesion, which is typically correlated with relatively low grain boundary resistance (< 10% of the total resistance).[71]

3.3.2 Electrochemical measurements

The temperature dependence of Li-LLZO-Li cell kinetics was determined using electrochemical impedance spectroscopy (EIS). The Li-LLZO charge interfacial resistance and total LLZO resistances were measured for each temperature (Figures 3.2a-b). Figure 3.2a shows the Li-LLZO interfacial resistance during heating and cooling. EIS analysis clearly indicates a reduction in Li-LLZO charge transfer with increasing temperature from 30 to 175°C. The lower values for charge transfer at each temperature during cooling in comparison with the values

during heating shows the permanent reduction in charge-transfer-resistance. We believe the permanent reduction results from improved wetting and contact between Li and LLZO, which would agree with similar observations of the Na-sodium beta alumina electrolyte interface.[79, 81-82] The minimum Li-LLZO interfacial resistance (2.7 $\Omega.cm^2$) was observed at 175˚C.

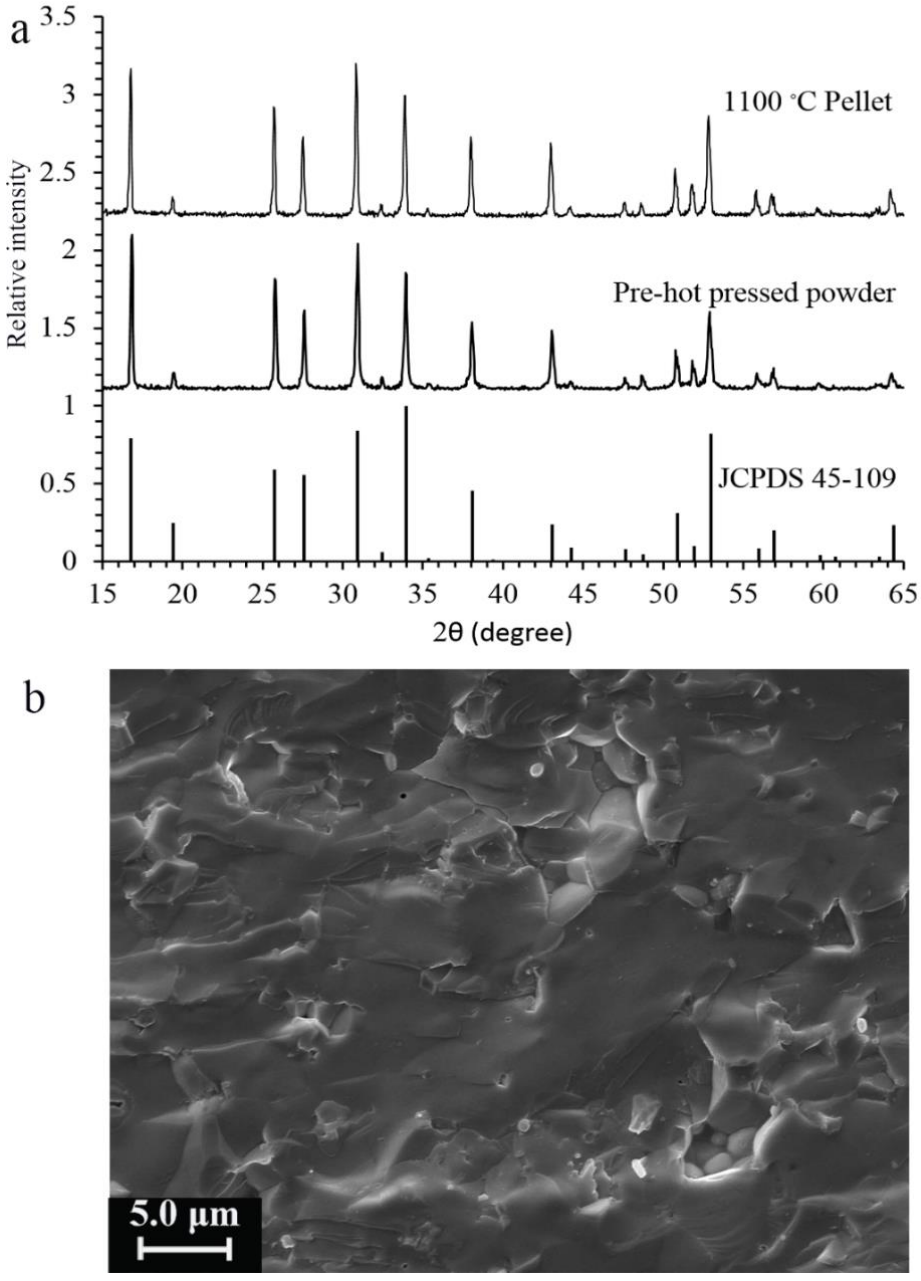

Figure 3.1. a) XRD patterns of LLZO calcined powder and pellet hot pressed at 1100◦C, JCPDS 45-109 is a reference for cubic garnet, b) secondary electron SEM image of an LLZO pellet fracture surface.

The reciprocal total LLZO resistance values were fitted using the Arrhenius equation (1):

$$R^{-1}T = Aexp\,(^{-E_a}/_{K_bT}) \quad (1)$$

where A is the pre-exponential factor, T is the absolute temperature, E_a is the activation energy, and k_b is Boltzmann's constant. The LLZO activation energy (total including grain and grain boundary resistances), was determined to be 0.28 eV, which is consistent with previously reported values.[46, 50, 83] Figure 3.2c shows representative Nyquist plots at 30˚C before and after preconditioning at 175˚C. The Nyquist plots consist of two distinct resistive components; one at relatively high frequencies (7 MHz - 500 kHz) and a second in the lower frequency region (500 kHz - 1 Hz). The high and low frequency semi-circles are attributed to Ohmic drop through the LLZO pellet, and Li-LLZO interface resistance, respectively.

The EIS spectrums were modeled using an equivalent circuit to determine the separate resistive phenomena where, R and CPE refer to resistance and constant phase element, respectively. The calculated capacitance values refined from the equivalent circuit for the total (bulk and grain boundary) LLZO and interfacial resistances range 10^{-12} to 10^{-8} F.cm^{-2} and 10^{-7} to 10^{-5} F.cm^{-2}, respectively.[72] These values are within the range of the expected capacitance values for these physical processes, thus validating our assignment of the two semi-circles in Figure 3.2c.[72-73] From Figure 3.2, several observations can be made. First, it is apparent that the LLZO total resistance has remained constant (171 Ω.cm^2) upon heating, preconditioning at 175˚C, and cooling (Figure 3.2d). This was expected since LLZO does not degrade in this temperature regime. Additionally, the total conductivity was calculated to be 0.46 mS.cm^{-1} for LLZO, which is in good agreement with previous data for hot-pressed Al doped LLZO.[46, 58] Second, the charge transfer resistance irreversibly decreased after preconditioning and cooling the cell temperature to 30˚C. Initially, the Li-LLZO interfacial resistance was 5822 Ω.cm^2 at 30˚C, but after heating to

175˚C and preconditioning the charge transfer dramatically decreased to 514 Ω.cm^2 upon cooling to 30˚C; a > 10-fold decrease. The interfacial resistance values were determined by dividing the low frequency (larger) semicircle diameters by a factor of two since the cells employed two Li anodes of equal area. At room temperature, an interfacial resistance of 514 Ω.cm^2 was measured, which matches the specified values for Li-LLZO interface (530 Ω.cm^2) as reported by Ohta *et al.*[60] However, despite the dramatic reduction in interfacial resistance, it remains relatively high compared to state-of-the-art (SOA) Li-ion technology that typically exhibits cell impedances in the tens of Ω.cm^2.[84] Detailed studies are needed to further reduce the Li-LLZO charge transfer resistance.

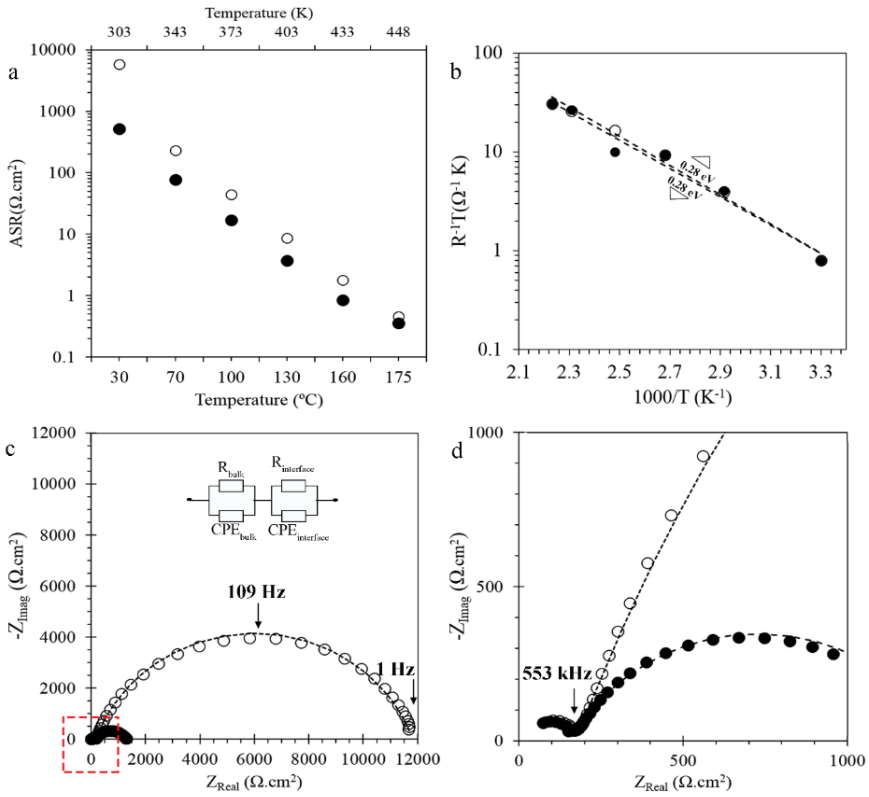

Figure 3.2. a) The Resistance of the Li-LLZO interface ($R_{Li\text{-}LLZO}$) as a function of temperature during heating (○) and cooling (●), b) the logarithm of the total LLZO resistance as a function of inverse temperature during heating (○) and cooling (●), c) representative Nyquist plots for Li-LLZO-Li cells at room temperature before (○), and after (●) preconditioning at 175˚C, d) the Nyquist plots in the dotted square region in c with focus on higher frequency range. Markers indicate experimental data and dotted lines represented the equivalent circuit modeling data for the Li-LLZO-Li cells.

The Li-LLZO interface stability was characterized as a function of current density and temperature using Li-LLZO-Li cells galvanostatically cycled between 30 and 160°C (Figure 3.3). From Figure 3.3, several observations can be made. First, for each temperature, Ohmic behavior was observed at lower current densities, followed by deviation from Ohmic behavior at higher current densities. Ohmic behavior refers to Ohm's Law (Equation 2):

$$V = IR \tag{2}$$

where the applied current (I) results in a stable Li-LLZO-Li cell voltage (V) based on the cell resistance (R). When cycling at 30 and 70°C, deviation from Ohmic behavior was marked by a subtle linear decrease in cell voltage followed by a sudden drop to ~ 0 V (Figures 3.3a, b). For the cells cycled at 30 and 70°C, the sudden drop to 0 V occurred at 50 and 200 $\mu A.cm^{-2}$, respectively. In comparison, when cycling at 100, 130 and 160°C the deviation in Ohmic behavior was marked by a non-linear increase in cell potential, followed by a sudden drop in potential (Figures 3.3c-e). For the cells cycled at 100, 130 and 160°C, the sudden drop to 0 V occurred at 800, 3500, and 20000 $\mu A.cm^{-2}$, respectively. Correlation between the two different mechanisms that deviate from Ohmic behavior is not known now; however, future work will investigate this phenomenon. Regardless, a drop to 0 V in all Li-LLZO-Li cells was apparent in the respective current ranges tested between 30 and 160°C. In this study, "critical current density" (CCD) is defined as the current density at which the cell voltage dropped to 0 V. Second, regardless of the type of deviation from Ohmic behavior, the CCD significantly increased with increasing temperature. The CCD is plotted as a function of temperature in Figure 3.3f. We believe that increasing the temperature improved wetting and contact between Li and LLZO, thus reducing interfacial resistance. Reducing the interfacial resistance likely resulted in

more uniform current density, thus increasing the CCD. Similar observations were made in Na-SBA cells cycled by Virkar *et al*.[85]

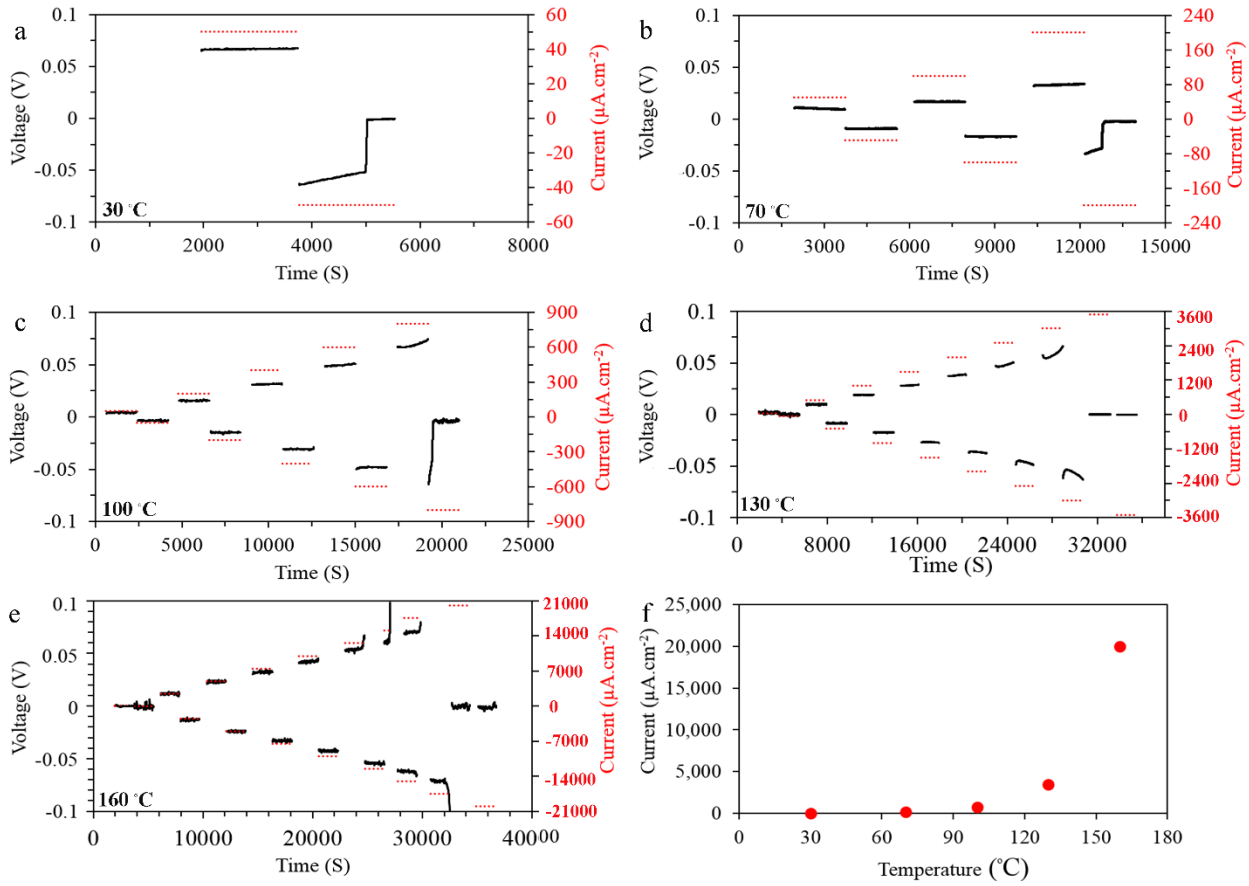

Figure 3.3. Galvanostatic cycling of Li-LLZO-Li cells at a) room temperature (30°C), b) 70°C, c) 100°C, d) 130°C, and e) 160°C. The critical current density vs temperature for Li-LLZO-/Li cells (f).

3.3.3 Post mortem analysis.

Figure 3.4a shows the EIS behavior of a Li-LLZO-Li cell before and after the cycling at 30°C, where the CCD was exceeded. The EIS data before DC cycling shows two distinctive semicircles between 7 MHz - 500 kHz and 500 kHz - 1 Hz, like Figure 3.2c. In contrast, the EIS data are clustered near the origin after the CCD was exceeded, indicating an electronic short circuit had occurred. XPS analysis suggests that the dark linear spots or regions have a more metallic Li character compared to the white or normal LLZO areas in the cycled pellet. These

spots are initiated and propagated from the Li plating face to the counter Li electrode. The Figure 3.4b insets show the distinct linear morphology (LLZO pellet face) and that the trajectory of the Li spots (LLZO cross-sectional fracture surface) follows the Li-ion current path between Li electrodes.

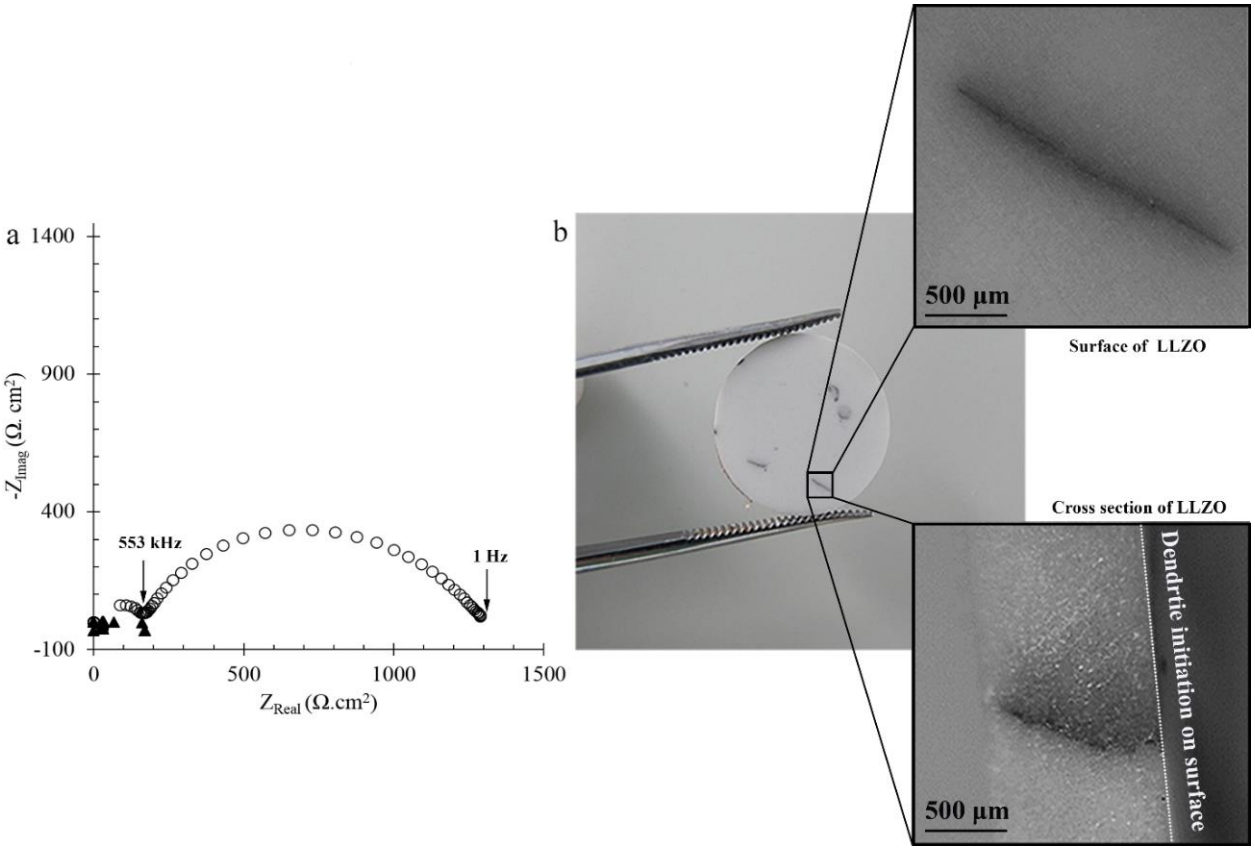

Figure 3.4. a) EIS data of a Li-LLZO-Li cell cycled at room temperature: before (○) and after the CCD was exceeded (▲); b) optical images of the dark spots that appeared in the cycled LLZO pellet: top face (top right), and cross-sectional fracture (bottom right) surfaces.

Assuming the features were metallic Li, attempts were made to determine if they propagated inter or transgranularly, Figure 3.5. To do so, a bending moment was applied to the pellet to cause fracture near or along the feature. Immediately after fracture, one half of the specimen was transferred into an SEM (Figure 3.5a). An SEM micrograph of the fractured surface is presented in Figure 3.5b, where a designated area B is enlarged and shown in Figure 3.5c. A distinguishable web-like structure was observed on particular regions of the fractured surface. In

higher magnification SEM image (Figure 3.5d), the web structure generally defined hexagonal-like features. Moreover, the LLZO predominately exhibited transgranular fracture, which is consistent with what was previously observed in fracture toughness analysis on LLZO of comparable relative density. Figure 3.5e presents the diameter distribution statistics of the web structure. The average diameter of the web structure was estimated to be 2.6 ± 0.7 μm, like the average grain size of LLZO, 2.8 ± 0.8 μm. In addition, the formation of the web structure appeared to be superimposed on the grain boundaries, implying that the web structure formed at the grain boundaries (intergranularly). The web structure was unavoidably exposed to air during specimen transfer between different analytical microscopes. Figure 3.5f depicts an SEM micrograph of the same web structure shown in Figure 3.5c, but after the exposure to air occurred during sample transfer. Higher magnification SEM images of the web structure in Figure 3.5f are shown in Figures 3.5g-h, from which porous reaction layers were observed on the web structure and the thickness of the web wall slightly increased. This indicated that the web structure was highly reactive in air compared to LLZO; consistent with the hypothesis that the web structure consisted of metallic Li.

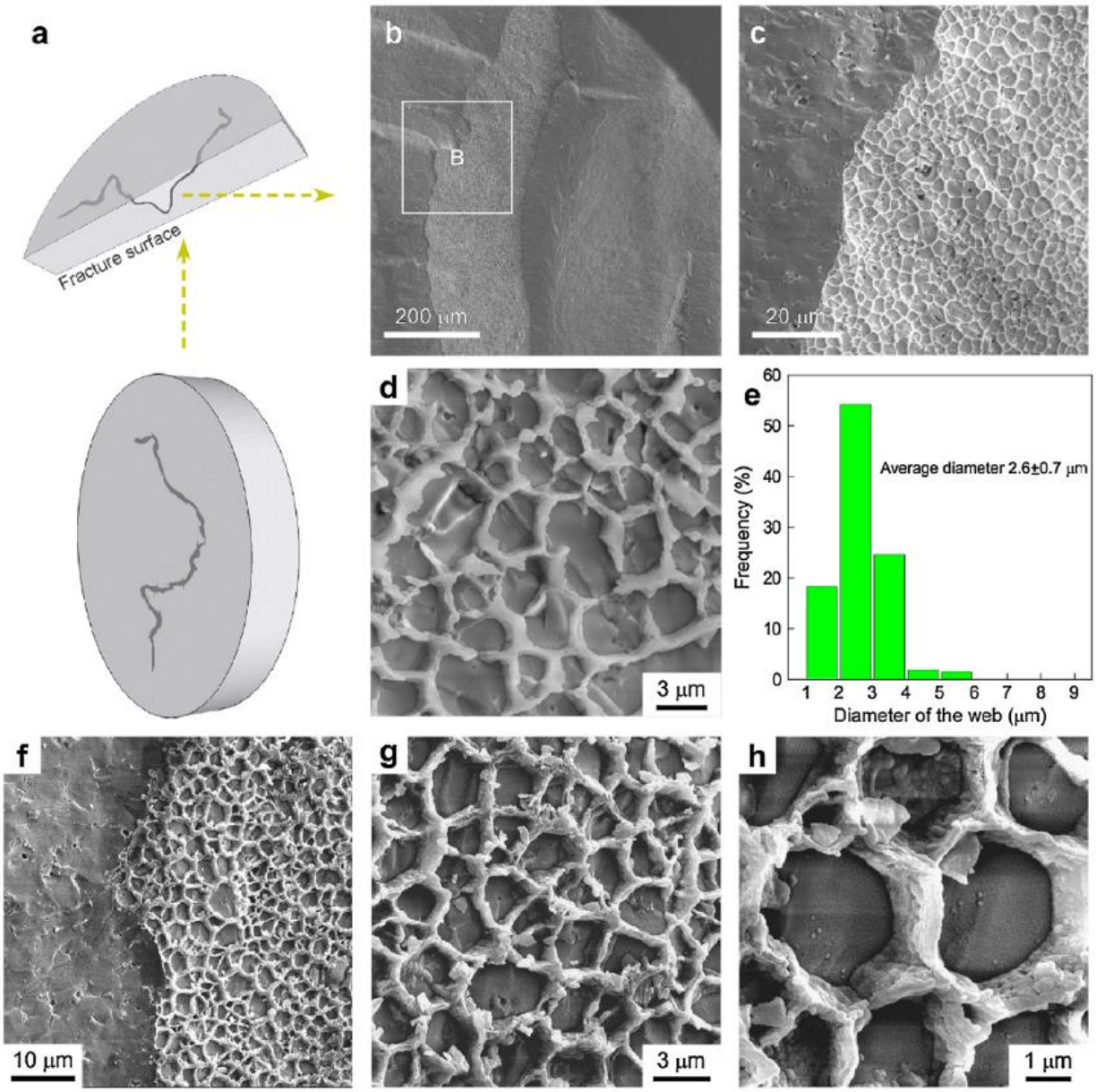

Figure 3.5. SEM micrographs of the web structure in cycled LLZO (a) illustration of a fractured surface through a black linear feature, (b) SEM image of a fracture surface, (c) enlarged SEM micrograph of the boxed area B in (a), (d) higher magnification SEM image of the web structure in (c), and (e) statistical distribution of the average hexagon-like diameters defined by the web structure. (f), (g) and (h) are successively amplified SEM images of the web structure after exposure to air.

AES is an analytical technique used to characterize the elemental makeup of the first few atomic layers (0.5–5 nm) of a surface using high spatial resolution (50 nm point-to-point), and precise chemical sensitivity. We investigated the surface chemical composition of the web structure by AES. An AES-SEM micrograph of the web structure is presented in Figure 3.6a, where Auger element mapping of Li was carried out, as shown in Figure 3.6b. The Li concentration in the web structure was much higher (bright contrast) than that in the LLZO matrix (dark contrast). In addition, an AES line scan for Li was performed in a different area, along line ABCD in the SEM micrograph shown in Figure 3.6c. Well-defined Li peaks were observed along line segment BC, where the line scan path from point B to C was located on the web structure. In contrast, almost no Li peaks were observed along line segments AB and CD, which was primarily believed to be LLZO. On the other hand, the Au line-scan spectrum along the line ABCD was nearly invariant. In general, the elemental distribution results (e.g., the distribution of Li and Zr) from AES were consistent with those from EDS. Therefore, based on the EDS and AES analysis, the grain consisted of LLZO garnet and the grain boundaries were saturated with Li metal. We believe this is the first report to directly measure the formation of metallic Li in LLZO.

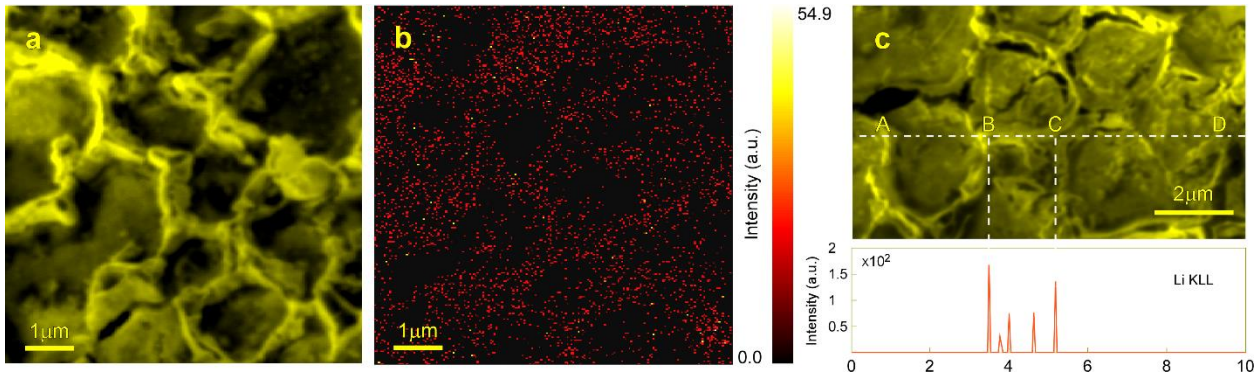

Figure 3.6. Auger analysis of the web structure (a) SEM image of the web structure, (b) Li mapping, (c) SEM image of the web structure and corresponding Auger line scan spectrum of Li along line ABCD.

The web structure closely resembled the LLZO microstructure in that the hexagonal shapes defined by the metallic Li mimicked grains in hot-pressed LLZO. In addition, the hexagonal feature diameters were close to the diameter of LLZO grains. Based on these observations, we believed the Li web structure was generally observed along the LLZO grain boundaries. Thus, Li plated intergranularly through the LLZO electrolyte grain boundaries causing the grains to fracture transgranularly as shown schematically in Figure 3.7b. Sudo et al. speculated that the black spots on the short-circuited LLZO surface was Li, growing through the grain boundaries or voids in LLZO.[59] Ren et al., using backscattered electron SEM and EDS, indicated that Li grew through grain boundaries and interconnected pores in short-circuited LLZO.[61] Though previous work certainly points to the formation Li metal propagation through LLZO, we believe that through the combination of precise microstructural control, striking SEM imagery, and the spatial resolution offered using Auger spectroscopy, this article is the first to confirm that Li propagates along grain boundaries in short-circuited LLZO. We believe this information will play a key role in elucidating Li metal propagation in polycrystalline solid electrolytes and can be used to establish strategies to stabilize the Li–solid electrolyte interface upon charging.

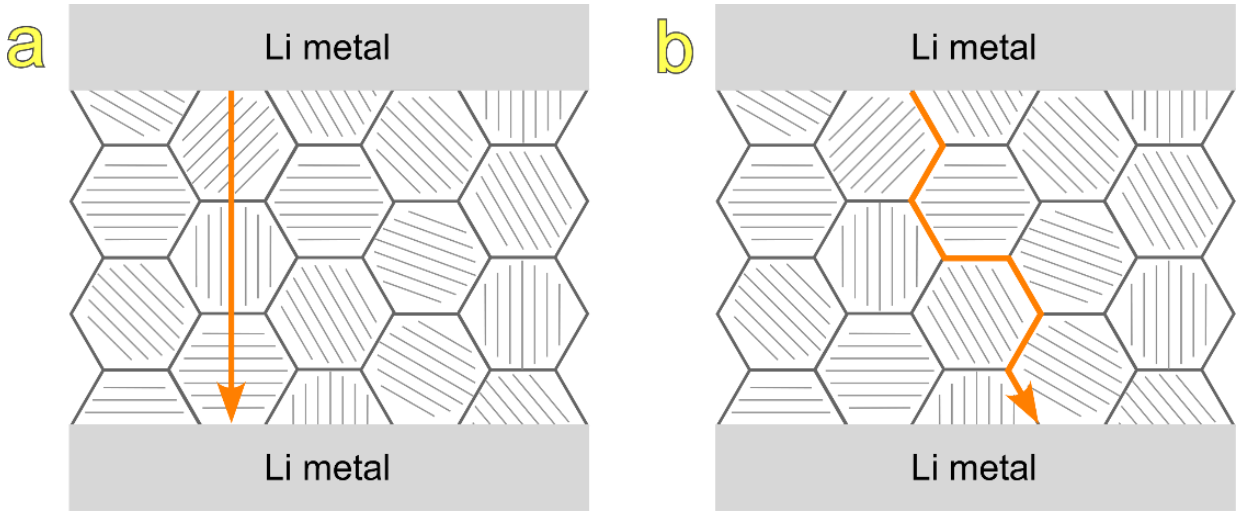

Figure 3.7. Illustration of Li metal plating through polycrystalline LLZO solid electrolyte (a) transgranular, (b) intergranular.

3.4 Conclusions

In this study, we demonstrated that temperature and current density significantly affect the Li-LLZO interface kinetics and stability between 30 – 175˚C. First, it was shown that the Li-LLZO interface resistance decreased with increasing temperature reaching a minimum value of 2.7 $\Omega.cm^2$ at 175˚C; just below the melting point of Li (180˚C). Second, the room temperature Li-LLZO interface resistance decreases dramatically from 5822 (as-assembled) to 514 $\Omega.cm^2$ by heating Li-LLZO-Li cells to 175˚C and cooling to room temperature. We believe heating, under constant pressure (350 kPa) improved contact between Li and LLZO to reduce the interfacial resistance. Third, it was shown that the maximum sustainable current density (or critical current density – CCD) increases significantly with increasing temperature. The CCD values as a function of temperature were 50, 200, 800, 3500 and 20000 $\mu A.cm^{-2}$ at 30, 70, 100, 130, and 160˚C, respectively. Furthermore, the formation of metallic Li spots was observed when the CCD was exceeded. We showed direct evidence for the first time that Li preferentially propagated intergranularly through LLZO grain boundaries and resulted in metallic short-circuiting of the Li-LLZO-Li symmetric cells during cycling. The results of this study are essential in understanding Li metal propagation in polycrystalline solid electrolytes and leading to potential strategies for stabilizing Li–solid electrolyte interface during charging. Overall, we believe the results of this study will help better understand the Li-LLZO interface stability to enable the use of batteries employing Li metal anodes and to improve the stability of the Li–solid electrolyte interface, future efforts should focus on engineering grain boundary structures to suppress Li filament propagation in polycrystalline solid electrolytes.

CHAPTER IV

Impact of air exposure and surface chemistry on the Li-$Li_7La_3Zr_2O_{12}$ interfacial resistance

4.1 Introduction

The energy density and safety of batteries are critical factors in the commercialization of electric vehicles (EVs). Li-ion batteries are the incumbent battery chemistry. The implementation of EVs will benefit immensely, however, from an increase in energy storage density, beyond what is possible with Li-ion cells. One approach to achieve this goal is to use metallic Li as the anode. Compared to conventional graphite-based anodes (volumetric capacity 330 $mAh.cm^{-3}$), a metallic Li anode would enable an eightfold increase in the volumetric capacity (2760 $mAh.cm^{-3}$). This would lead to batteries with energy densities exceeding 1000 $Wh.\ l^{-1}$, or a 100% improvement over Li-ion cells.[8]

Despite these benefits, non-uniform deposition and dendrite formation at the anode during cycling has limited the use of metallic Li when paired with liquid electrolytes. The coupling of solid-state electrolytes (SSE) with metallic Li anodes has recently emerged to potentially resolve the dendrite issue. For example, the garnet-type Li-ion conductor, $Li_7La_3Zr_2O_{12}$ (LLZO), exhibits a unique combination of high ion conductivity (1 $mS.cm^{-1}$ at 298 K) and wide electrochemical window.[46, 51] Additionally, LLZO has a shear modulus that is 14 times higher than metallic Li, suggesting that it could act as a physical barrier to suppress dendrite formation.[52]

While LLZO exhibits favorable transport and mechanical properties, its stability in air, and the consequences for air exposure on resistance at LLZO-electrode interfaces, are not well understood. To compete with conventional Li-ion batteries, the Li-LLZO interfacial resistance should be lower than 100 $\Omega.cm^2$.[86-90] Recent experimental and theoretical studies indicate LLZO indeed reacts with air, although subtly, but enough to dramatically affect the interface resistance.[65, 91-94]

Different pathways have been proposed to describe the reaction between air and LLZO. Studies on $Li_5La_3M_2O_{12}$ (M=Nb, Ta) and $Li_7La_3M_2O_{12}$ (M=Sn, Zr) exhibited spontaneous Li^+/H^+ ion exchange when exposed to water.[60, 95] It was shown that water reacts with LLZO to form LiOH either as a surface film (when exposed to moist air), or as a precipitate in solution (when immersed in water). This LiOH would subsequently react with CO_2 in air to form Li_2CO_3.[95-96] Conversely, other studies reported a single-step reaction pathway where the garnet reacts directly with water and CO_2 to form Li_2CO_3.[91, 94] More recently, Cheng *et al*. reported that LLZO reacts with water to form Li deficient garnet and LiOH, without Li^+/H^+ ion exchange.[91] Cheng *et al.* suggested that Li_2CO_3 formation can either occur through CO_2 absorption by LiOH or the direct reaction of LLZO with CO_2. It was suggested that direct reaction of LLZO with CO_2 is the energetically-preferred reaction pathway. Additionally, Cheng *et al*. reported the presence of Li_2CO_3 as an insulating layer on the LLZO surface after processing in air led to high interfacial resistance at the Li-LLZO interface.[91]

Though previous work confirms LLZO reacts with air, it is clear that consensus regarding the reaction pathway has not been achieved. Clarifying the reaction pathway and how the reaction products affect the Li-LLZO interface resistance will facilitate technological maturation. Moreover, a better understanding of the effect of relative humidity (RH) and exposure time on

the extent and consequences of these reactions would be very helpful. Such information could be useful in developing a methodology to achieve consistent Li-LLZO interfacial resistance during assembling of solid-state cells.

This study aims to clarify the effects of RH and air exposure time with changes in LLZO surface chemistry and Li-LLZO interfacial resistance using a combination of computational modeling and experimental measurements. First, density functional theory (DFT) was used to investigate the reaction between LLZO and air. Previous DFT calculations examined the carbonation of LLZO via formation of LiOH or by direct reaction of LLZO with CO_2.[97] The present study takes a different approach by exploring a hydration/carbonation reaction pathway that involves Li^+/H^+ ion exchange;[98] such ion exchange has been demonstrated to be facile, for example, in aqueous environments.[96, 98] In addition, comparisons are made with pathways involving direct reaction of LLZO with CO_2 and H_2O. Our DFT calculations indicate that the Li^+/H^+ ion exchange pathway is a thermodynamically favorable route for the formation of a Li_2CO_3 layer on the surface of LLZO. On the other hand, direct hydration and carbonation of LLZO is found to be thermodynamically unfavorable.

Experimental measurements were performed on LLZO samples exposed for up to 240 h in air with relative humidities (RHs) comparable to; that found in ambient air (RH ~ 50%) and in Li-ion battery fabrication dry room air (RH ~ 0.5%). The resulting changes in surface chemistry were characterized using X-ray photoelectron spectroscopy (XPS), scanning electron microscopy (SEM), Raman spectroscopy, and transmission electron microcopy (TEM). These analyses suggest a reaction pathway resulting in the formation of a Li_2CO_3 contamination layer on LLZO. Moreover, the growth rate of Li_2CO_3 on LLZO correlates with air exposure time and RH.

The impact of surface contamination on the Li-LLZO interfacial resistance was explored by electrochemical impedance spectroscopy (EIS). We observe that contamination layers formed on the LLZO surface changed the chemistry of the Li-LLZO interface and contribute to an increase in the interfacial resistance. For example, air exposure for 240 h resulted in a significant increase in resistance, from 54 (no exposure) to ~3000 and ~37,000 $\Omega.cm^2$ for air with 0.5 and 50% relative humidity, respectively. Thus, higher RH has a profound effect on Li-LLZO interfacial resistance.

Through combined theory, materials characterization, and electrochemical analysis, LLZO reactivity with air as a function of time and relative humidity is elucidated. It will be shown that LLZO can withstand exposure to ambient air while maintaining Li-LLZO interface resistances comparable to other reports. The knowledge gained could enable fabrication of solid-state batteries in ambient air, which would significantly simplify and reduce the cost of production.

4.2 Experimental

4.2.1 Powder synthesis and pellet processing of solid-state electrolyte

Cubic Al-doped LLZO with nominal composition of $Li_{6.25}Al_{0.25}La_3Zr_2O_{12}$ was prepared using solid-state synthetic technique explained in chapter 2 section 2.3. After grinding and sieving, the calcined powder was hot-pressed into pellets with 12.7 mm diameter at 1100℃ and 62 MPa pressure for 1 h under argon flow by rapid induction hot press (RIHP, Across International, Livingston NJ) in graphite die to achieve 97 ± 1% relative density and eliminate the effect of volume percent of porosity on the results. The hot-pressed pellets were cut into 1 ± 0.2 mm thick samples using diamond saw (Buehler, Lake Bluff, IL). Samples were mechanically polished using 400 grit sandpapers (Norton Abrasives, Worcester, MA) to ensure both faces were parallel, then all the LLZO were transferred to an argon-filled glovebox with <0.1 ppm

oxygen level. To characterize the stability of LLZO against air and moisture, each sample was dry-polished with 400, 600, 1500 and 2000 grit SiC sandpapers inside an argon-filled glovebox to remove the entire contamination layer formed during processing and achieve a well-defined fresh surface, which had not been in contact with air before. Then, the LLZO were exposed to ambient air with 50% relative humidity (RH) and dry air with 0.5% RH, and -40℃ dew point for duration between 0 to 240 h.

4.2.2 Calculations

The thermodynamics of the hydration and carbonation of LLZO were examined using first-principles calculations. All calculations were conducted using density functional theory (DFT) with a plane wave basis set, as implemented in the Vienna *Ab initio* Simulation Package (VASP).[99] Core-valence electron interactions were treated using the projector augmented wave (PAW) method.[100-101] The generalized gradient approximation (GGA) of Perdew, Burke, and Ernzerhof (PBE) was used for the exchange-correlation energy.[102] The convergence criterion for the electronic self-consistency loop was set to 10^{-5} eV, and ionic relaxations were converged to a force tolerance of less than 0.03 eV.$Å^{-1}$. An energy cutoff of 600 eV was used for the plane wave basis and the Brillouin zone was sampled using the Monkhorst−Pack scheme. A 2 × 2 × 2 k-point grid was used for LLZO, and 12 × 12 × 12 k-point mesh was used for crystalline LiOH, Li_2O, and Li_2CO_3.

The conventional cubic unit cell of $Li_7La_3Zr_2O_{12}$ (8 formula units, 192 atoms) was adopted as the simulation cell.[54] Lithium was distributed on the partially-occupied 24d and 96h Li-sub lattice sites according to an algorithm that minimizes occupancy of electrostatically-unfavorable first nearest-neighbor sites.[54] An earlier study showed negligible energy differences (<1.5 meV.$atom^{-1}$) amongst several LLZO structures generated using this procedure.[54, 103] The LLZO

structure having the lowest total energy (with 13 and 43 atoms occupying the 24d and 96h Li sites, respectively) was adopted for subsequent calculations.

Calculations on hydrogen-doped LLZO were performed by substituting hydrogen atoms for selected Li atoms. A prior experimental study of proton exchange in LLZO reported that proton substitution preferentially occurs on the 96h sites.[103-104] Our DFT calculations are consistent with the site preference observed experimentally: At low proton concentrations (2% and 9% Li^+/H^+ exchange) 96h sites are weakly favored over 24d sites by 1 to 8 meV per atom. At higher concentrations (~ 63% Li^+/H^+ exchange) the preference for the 96h sites increases to ~20 meV per atom.

The molecular species H_2O and CO_2 were simulated within cubic simulation cells with dimensions of 8 Å; crystal structures for LiOH, Li_2O, and Li_2CO_3 were taken from experimental data.[103, 105] The optimal lattice parameters for all computational cells were obtained by fitting total energy *vs.* volume data to the Murnaghan equation of state.[106]

The Gibbs free energies of gas and liquid phases were obtained using equations (1) and (2):

Gas phase: $G(T) = E_{0\mathrm{K(g)}}^{\mathrm{DFT}} + \Delta H(T) - TS_{\mathrm{(g)}}^{\mathrm{expt}}(T)$ (1)

Liquid phase: $G(T) = E_{0\mathrm{K(g)}}^{\mathrm{DFT}} + \Delta H(T) - \Delta H_{\mathrm{vap}}^{\mathrm{expt}}(T) - TS_{\mathrm{(l)}}^{\mathrm{expt}}(T)$ (2)

Here $E_{0\mathrm{K(g)}}^{\mathrm{DFT}}$ is the total energy of an isolated gas phase molecule at zero Kelvin, $\Delta H(T)$ is the enthalpy difference for the molecule associated with a temperature change between 0K and a given temperature T, $S_{\mathrm{(i)}}^{\mathrm{expt}}$ is the experimental gas (i=g) or liquid (i=l) phase entropy at temperature T,[107] and $\Delta H_{\mathrm{vap}}^{\mathrm{expt}}(T)$ is the experimental enthalpy of vaporization.[108] The ideal gas approximation was used to estimate the enthalpy difference, $\Delta H(T) \approx nk_{\mathrm{B}}T$, where n is 7/2 for linear molecules (i.e., CO_2) and 4 for nonlinear molecules (i.e., H_2O), respectively. The pressure

was set to 1 atm. Finally, the Gibbs free energies of solids were approximated as the DFT total energy, $G \approx E_{0\mathrm{K}}^{\mathrm{DFT}}$.

4.2.3 Materials characterizations

The formation and morphology of contamination layers after air exposure was examined using scanning electron microscopy, and their elemental composition was determined by energy-dispersive X-ray spectroscopy (SEM/EDS, FEI Nova 200 Nano Lab Dualbeam, Hillsboro, OR) at an accelerating voltage of 10 kV and a working distance of 5 mm.

Raman spectroscopy (Renishaw inVia Raman microscope, Hoffman Estates, IL) was performed using a 532 nm laser, 2400 lines per mm holographic grating and 50X magnification using power of 100 mW to determine the surface composition and chemistry. All the intensity profiles were normalized by the corresponding maximum values. Direct Classical Least Squares (DCLS) method was used to determine the quantitative analysis of Raman spectroscopy regarding the LLZO surface constituent properties. DCLS finds the combination of spectra from the pure components contained in the sample that more closely matches the Raman spectrum of the sample. Reference spectra for all the possible component of the surface (i.e. cubic LLZO, Li_2CO_3 and LiOH) were acquired. The DCLS method approximates the spectrum at each point in the map by adding the entire scaled reference spectrum. The scaling factors helped to get the best fit to the original map to show the distribution of each reference spectrum.

The subsurface composition based on the degree of air exposure was evaluated using scanning transmission electron microscopy (STEM) and electron energy loss spectroscopy (EELS). TEM technique (STEM/EELS, an aberration-corrected FEI Titan S 80-300 TEM/STEM, Hillsboro, OR) equipped with a Gatan Image Filter Quantum-865 operated at 300 kV. Z-contrast HAADF-STEM imaging was performed with a probe convergence angle of 30

mrad and a large inner collection angle of 65 mrad. EELS data were collected in STEM mode using a 5 mm aperture and a spectrometer collection angle of 40 mrad. Before being exposed to ambience air, a LLZO was split into two pieces to create a fresh surface for this study. After 24 h exposure, the cross-section surface then was coated with a ~ 40 nm gold layer followed with a thick tungsten layer on surface. The TEM specimen was then prepared by using a Hitachi NB-5000 dual (Focused Ion/Electron) beam microscope. When the specimen was properly prepared, it was transferred into a vacuum transfer TEM holder inside the FIB. The specimen is finally transferred to an FEI double tilt holder in a glove bag before being put in the TEM.

X-ray photoelectron spectroscopy (XPS) was performed with a Thermo Scientific Model K-Alpha XPS instrument. The instrument uses a monochromated, micro-focusing, Al K_α X-ray source (1486.6 eV) with a variable spot size (30-400 μm). Analyses of LLZO samples used the 400 μm X-ray spot size for maximum signal and to obtain an average surface composition over the largest possible area. The instrument has a hemispherical electron energy analyzer equipped with a 128 multi-channel detector system. The base pressure in the analysis chamber is typically 2×10^{-9} mbar or lower. LLZO samples were fixed to the sample holder using metal clips. Wide energy ranges survey spectra (0-1350 eV) were acquired at an analyzer pass energy of 200 eV. Narrow energy range core level spectra were acquired an analyzer pass energy of 50 eV. Argon-ion depth profiling was performed using a 2 kV argon-ion beam rastered over an area 1 X 2 mm and alternated with core level data acquisition cycles. The depth scale was calibrated using standard SiO_2 films to measure the argon-ion gun sputter rate (note that the depth scales shown are relative to the sputter rate of SiO_2). For depth profiling a rapid data acquisition mode was used that takes a series of "snapshots" of the core level of interest across the 128-channel detector. Charging was avoided by using a charge neutralization system that uses a combination

of low energy electrons and low energy argon ions for optimum charge compensation. The typical pressure in the analysis chamber with the flood gun operating was 2 x 10^{-7} mbar. Data were collected and processed using the Thermo Scientific Avantage XPS software package (v 4.61).

4.2.4 Electrochemical impedance measurements

The Li-LLZO-Li cell impedance as a function of exposure time and RH level was characterized by electrochemical impedance spectroscopy (EIS) technique between 1 Hz to 7 MHz using a 100 mV perturbation amplitude (VMP300, Bio-Logic, Knoxville, TN). The LLZO samples were transferred inside an argon-filled glovebox after air exposure for specific amount of time (0, 24, 120, 240 h) to eliminate further formation and the growth of contamination layer. Li foil (Alfa Aesar, Ward Hill, MA) was scraped using a stainless-steel spatula to remove the oxide surface layer and expose the fresh metallic Li surface. The LLZO was placed between two scrapped Li foil. Afterward, the stack was placed under uniaxial force of 365 kPa to achieve a better contact between Li and LLZO at the interface.

An equivalent circuit model was used for modeling the EIS data. The entire impedance spectrum for each cell was normalized to Li and LLZO contact area (1.26 cm^2) before the data modeling was performed. The EIS data was modeled using the equivalent circuit model shown in Figure 7a. In this model, a combination of a resistor and a capacitor in parallel are used to represent each component in the cell. Thus, three parallel combinations were used in the model representing the bulk and the grain boundary of LLZO, and the Li-LLZO interface. The ideal capacitors were replaced with constant phase elements (CPE) to account for any non-ideal behavior and dispersion in to the time constant. The ideality of The CPE is represented by the coefficient α (α=1 shows the component is behaving as an ideal capacitors) The Q values for the

CPE should be on the order of 10^{-12}, 10^{-8}, 10^{-6} F for bulks, grain boundaries and Li-LLZO interface, respectively. The data fitting and circuit modeling was done with a software package EC-Lab V10.44.

4.3 Results and discussion

4.3.1 First principle calculations

The thermodynamic driving force (i.e., the Gibbs free energy of reaction, ΔG) for the hydration and/or carbonation of LLZO was evaluated using DFT calculations for several plausible reaction pathways. The first pathway results in Li_2CO_3 formation, and proceeds via a two-step process that involves protonation of LLZO (i.e., Li^+/H^+ exchange) and the formation of LiOH as an intermediate:[96, 109]

Li^+/H^+ ion exchange: $Li_7La_3Zr_2O_{12} + x\,H_2O \rightarrow Li_{7-x}H_xLa_3Zr_2O_{12} + x\,LiOH$ (3a)

Carbonation of LiOH: $LiOH + \frac{1}{2}\,CO_2 \rightarrow \frac{1}{2}Li_2CO_3 + \frac{1}{2}\,H_2O$ (3b)

In a similar fashion, the second pathway also results in LLZO protonation and formation of Li_2CO_3, but proceeds through an Li_2O intermediate:

Li^+/H^+ ion exchange: $Li_7La_3Zr_2O_{12} + x\,H_2O \rightarrow Li_{7-2x}H_{2x}La_3Zr_2O_{12} + x\,Li_2O$ (4a)

Carbonation of Li_2O: $Li_2O + CO_2 \rightarrow Li_2CO_3$. (4b)

Finally, the energetics of direct hydration and carbonation of LLZO were also investigated:

Direct hydration: $Li_7La_3Zr_2O_{12} + x\,H_2O \rightarrow Li_{7-2x}La_3Zr_2O_{12-x} + 2x\,LiOH$ (5a)

Direct carbonation: $Li_7La_3Zr_2O_{12} + x\,CO_2 \rightarrow Li_{7-2x}La_3Zr_2O_{12-x} + x\,Li_2CO_3$ (5b)

Table 4.1 summarizes the calculated ΔG for reactions 3-5 with $x = 1/8$ at T = 298.15 K. (here $x = 1/8$ refers to the exchange of a single Li^+ for H^+ in the LLZO computational cell for reactions 3a-b, to the exchange of two Li^+/H^+ pairs for reactions 4a-b, and to the extraction of a single formula unit of Li_2O in reactions 5a-b.) Several configurations were examined for the

substitution and extraction of these species; the lowest energy configurations were used to evaluate Equations 3-5. Overall, pathway 3a-b (involving protonation of LLZO and formation of an LiOH intermediate) is predicted to be the most thermodynamically favorable reaction, given the negative values calculated for ΔG, -33 kJ.mol^{-1} for reaction 3a and -34 kJ.mol^{-1} for 3b. These data are in good qualitative agreement with experimental measurements that report Li^+/H^+ ion exchange and Li_2CO_3 formation in ambient air.[96] On the other hand, pathway 4a-b (involving protonation of LLZO and formation of an Li_2O intermediate) is somewhat less favored due to the positive reaction energy of 21 kJ.mol^{-1} predicated for its first step, reaction 4a. In addition, the total reaction energy for pathway 4, -127 kJ per Li_2CO_3 formula unit (f.u.), is slightly less exergonic than that of reaction 3: -134 kJ per Li_2CO_3 f.u. Finally, formation of LiOH and Li_2CO_3 by the direct reaction of LLZO with H_2O or CO_2 (Equation. 5a-b) is predicted to be thermodynamically unfavorable, as $\Delta G > 0$ for both reactions (ΔG = 83 kJ.mol^{-1} for reaction 5a and 15 kJ.mol^{-1} for 5b).

Table 4.1. Calculated Gibbs free energy for the hydration and carbonation of LLZO depicted in reactions 3-6 with $\boldsymbol{x = 1/8}$ at 298.15 K for. Reactions involve Li^+/H^+ ion exchange (i.e., protonation) and formation of a LiOH (reaction 3(a-b)) or a Li_2O (reaction 4(a-b)) intermediate phase. Reactions 5(a-b) assume direct hydration and carbonation of LLZO. Reaction 6 depicts the thermal decomposition of Li_2CO_3 in the presence of protonated LLZO**.**

Reaction no.	Reaction (assuming x = 1/8)	ΔG /kJ.mol^{-1}
3(a)	$Li_{56}La_{24}Zr_{16}O_{96} + H_2O(g) \rightarrow Li_{55}HLa_{24}Zr_{16}O_{96} + LiOH$	- 33.0
3(b)	$LiOH + 1/2\ CO_2(g) \rightarrow 1/2\ Li_2CO_3 + 1/2\ H_2O(g)$	- 33.6
4(a)	$Li_{56}La_{24}Zr_{16}O_{96} + H_2O(g) \rightarrow Li_{54}H_2La_{24}Zr_{16}O_{96} + Li_2O$	+ 21.5
4(b)	$Li_2O + CO_2(g) \rightarrow Li_2CO_3$	- 147.6
5(a)	$Li_{56}La_{24}Zr_{16}O_{96} + H_2O(g) \rightarrow Li_{54}La_{24}Zr_{16}O_{95} + 2LiOH$	+ 82.8
5(b)	$Li_{56}La_{24}Zr_{16}O_{96} + CO_2(g) \rightarrow Li_{54}La_{24}Zr_{16}O_{95} + Li_2CO_3$	+ 15.6
6	$Li_{55}HLa_{24}Zr_{16}O_{96} + \frac{1}{2}Li_2CO_3 \rightarrow Li_{56}La_{24}Zr_{16}O_{96} + \frac{1}{2}H_2O(g) + \frac{1}{2}CO_2(g)$	+ 66.6

Figure 4.1a plots ΔG at T = 298.15 K for reaction 3(a) as a function of the Li^+/H^+ exchange percentage. The data reveals that Li^+/H^+ ion exchange is thermodynamically favorable for all proton compositions up to full exchange of Li^+. The most negative ΔG value occurs at approximately 80% protonation; this value is in reasonable agreement with an earlier experimental study that observed approximately 60% of Li in LLZO powder could be exchanged with hydrogen in de-ionized water at room temperature.[98, 103] Although ΔG is negative for all proton concentrations, limited Li^+/H^+ ion mobility within partially ion-exchanged LLZO could kinetically preclude achieving very high (or full) proton exchange.[98]

Figure 4.1b plots ΔG for reaction 3(a) (assuming $x = 1/8$) as a function of temperature and the phase of the proton source, liquid or gaseous water. The data reveals that reaction 3(a) is favorable at low-to-moderate temperatures, $\Delta G < 0$ up to 466 K, regardless of whether water is a liquid or vapor. At higher temperatures, the positive values of ΔG for reaction 3(a) indicate the possibility for reversing the effects of water exposure by decomposing LiOH and de-protonating LLZO. In addition, we investigated the possibility for thermal decomposition of Li_2CO_3 based on a pathway that is the reverse of reactions 3a-b:

$$Li_{7-x}H_xLa_3Zr_2O_{12} + \frac{x}{2}Li_2CO_3 \rightarrow Li_7La_3Zr_2O_{12} + \frac{x}{2}H_2O + \frac{x}{2}CO_2 \quad (6)$$

As before, we assume $x = 1/8$ (the exchange of a single Li^+ for H^+ in the LLZO unit cell). The energetics associated with reaction 6 at T = 298.15 K are summarized in Table 4.1. Our calculations indicate that reaction 6 becomes thermodynamically favorable at 597 K, suggesting the possibility for decomposition of Li_2CO_3 and de-protonation of LLZO at high temperatures. Our predicted decomposition temperature is consistent with earlier TG-MS measurements showing H_2O evolution from LLZO at approximately 523 K, and de-protonation of LLZO with decomposition of Li_2CO_3 between 673 and 773 K .[109]

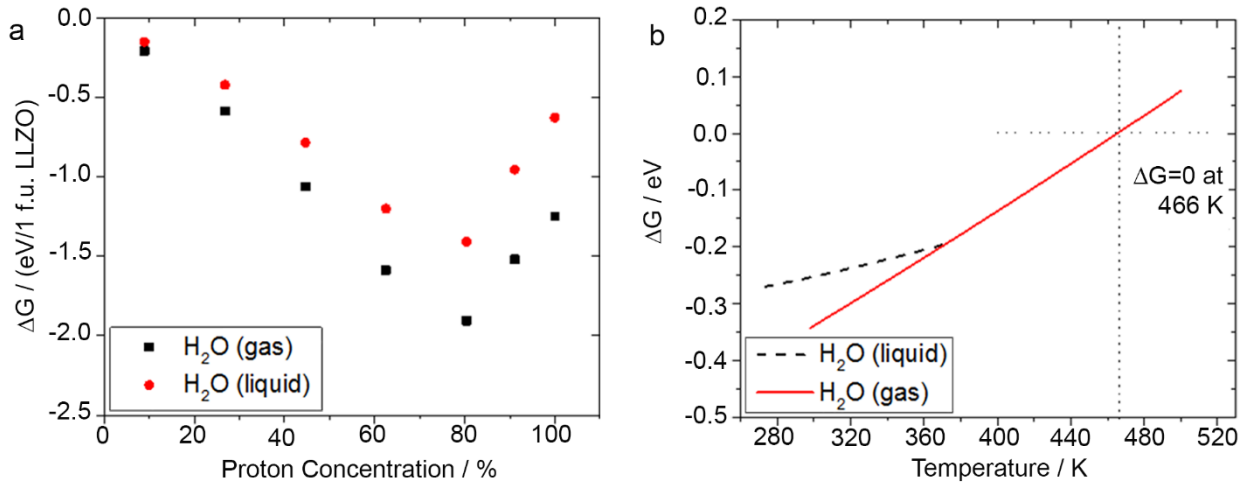

Figure 4.1. DFT calculations to evaluate the reactivity between ambient and LLZO. (a) the change in Gibbs free energy at 298.15 K for reaction 3(a) as a function of proton concentration, (b) the change in Gibbs free energy for LLZO protonation, reaction 3(a), as a function of temperature and the phase of the proton source (liquid or gaseous H_2O). The calculation assumes $x = 1/8$.

4.3.2 XPS depth profiling analysis

To elucidate the details of the reaction between LLZO and air, experiments were conducted to compliment the DFT calculations. First, XPS was conducted on the LLZO to determine the dominant surface species and evaluate if these species were consistent with the results of DFT calculations. Chemical stability and surface reactivity of LLZO after initial processing in ambient air (RH ~ 50%) was studied using XPS. The initial processing includes hot-pressing, cutting and dry polishing in ambient air prior to transferring into the glovebox. XPS depth profiling analysis was performed using an argon-ion sputtering source. Figure 4.2a and b show the typical carbon and Li 1s core level spectra at different sputter depths (time intervals) with 0 nm corresponding to zero sputtering time. Information regarding other core levels (O 1s, Zr 3d and $La3d_{5/2}$) can be found in the Figure 4.3. The depth profiling analysis of all the core levels as a function of thickness is presented in Figure 4.2c. At 0 nm, we find two primary carbon components with a larger intensity peak at a binding energy (BE) of 284.8 eV corresponding to adsorbed hydrocarbons and another at higher BE peak at 290 eV attributed to carbonate species.

Consistent with C 1s core level, the O 1s signal (Figure 4.3a) also shows two features. The adsorbed hydrocarbons were readily removed as evidenced by the diminishing C 1s peak down to 40 nm, but still substantial carbonate species were present. Upon sputtering 100's of nm below the surface, the carbonate layer is completely removed as shown by the black spectrum in Figure 4.2a at 450 nm. Consistent with this observation, the Li 1s core level corresponding to the pure carbonate component is at 55 eV at 0 nm and then progressively moves towards lower BE at higher sputtering times, finally overlapping with the relatively strong Zr 4s signal at 450 nm. Based on the relative intensity variation of Li, C, O, Zr, La XPS core levels as a function of sputtering depth, the LLZO atomic compositions at various depths can be determined as summarized in Figure 4.2c. The respective elemental core levels are marked by (I), (II) and (III) for carbonate, intermediate oxide/hydroxide, and LLZO, respectively.

The carbonate was present up to 5-10 nm beneath the surface then decreased gradually reaching the minimum concentration at about 40 nm. This gradual decrease in carbonate content was accompanied by an increase in the Li oxide/hydroxide, Li (II), suggesting a buried oxide/hydroxide layer. However, the difference in BE values for Li 1s between the oxide versus hydroxide is relatively small and difficult to de-convolute. Sputtering deeper than 40 nm (in the region between 40 to 100 nm) revealed a decrease in the Li (II) content with a gradual increase in the La and Zr concentration. It is worth noting that in the region between 40 to 120 nm, the three components (carbonate, Li oxide/hydroxide and LLZO) are simultaneously present. In this region, the pristine or bulk LLZO content gradually increases while both the carbonate and Li

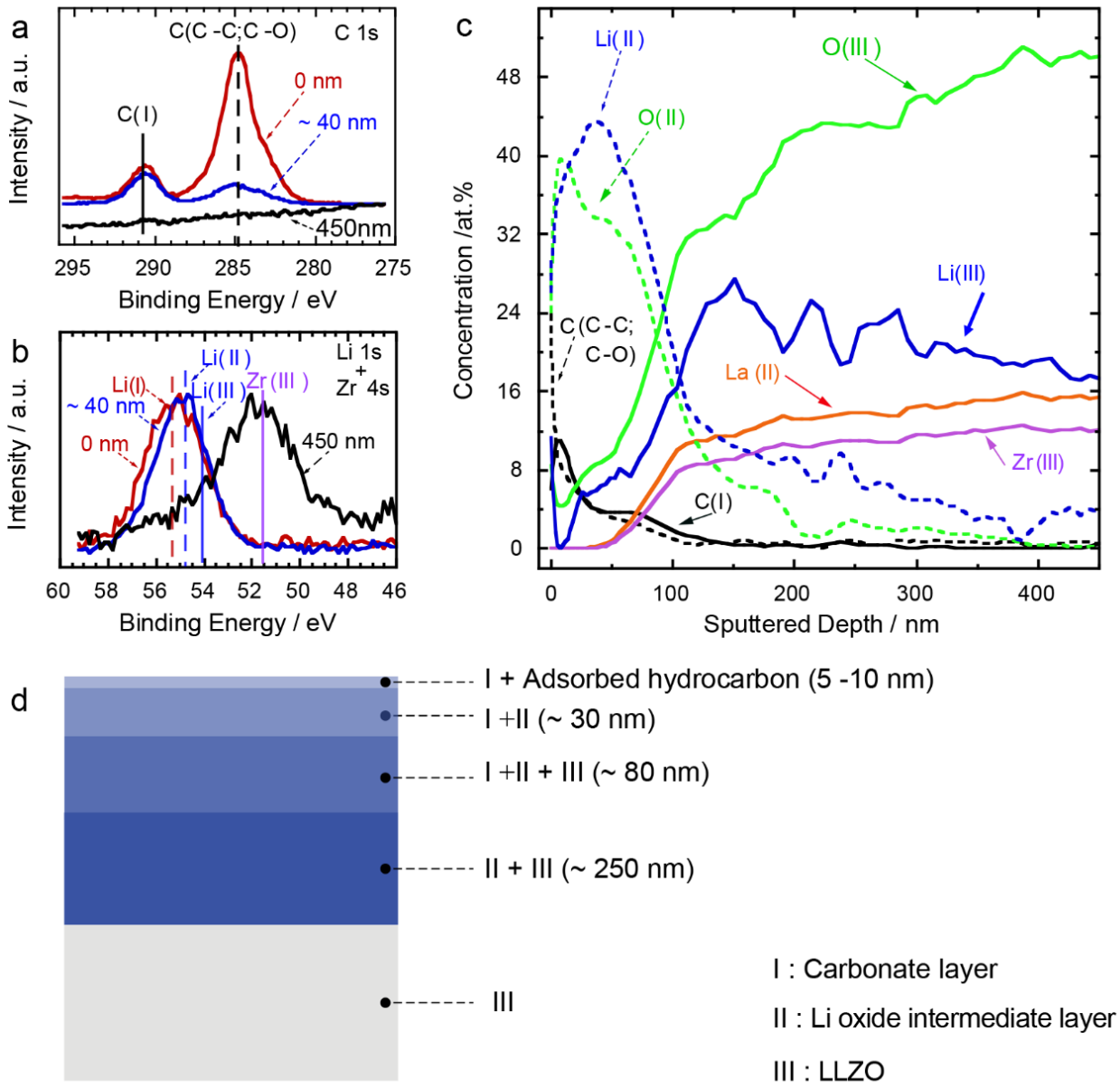

Figure 4.2. XPS analysis of LLZO after sample preparation in ambient air. (a) C 1s and (b) Li 1s + Zr 4s at different sputtering depths. (c) Depth profile for the concentration of Li, C, O, Zr, La from the XPS core levels analysis. (d) Schematic depicting the contamination layers that comprise the XPS analysis (the numbers between parenthesis represent the layer thickness estimated from the depth profile).

oxide/hydroxide concentrations diminished with increasing sputtering depth. It is important to note that given the weak XPS cross-section for Li, a relatively large uncertainty for determining the Li composition is expected compared to other easier to detect core levels. Further, in bulk LLZO regions the Li 1s substantially overlaps with Zr 4s complicating the analysis. The schematic in Figure 4.2d summarize the findings described above. These findings show the surface of LLZO is readily contaminated during processing and preparation in air**.** To further explore the implications of these results, more detailed experiments were carried out to probe the effect of RH and time on the surface chemistry and topography upon gradual exposure of LLZO to air. To this end, the LLZO samples were polished and stored in an argon-filled glovebox to remove the contamination layer formed on the surface during processing and exposed to ambient (RH ~ 50%) and dry air (RH ~ 0.5%) for various times.

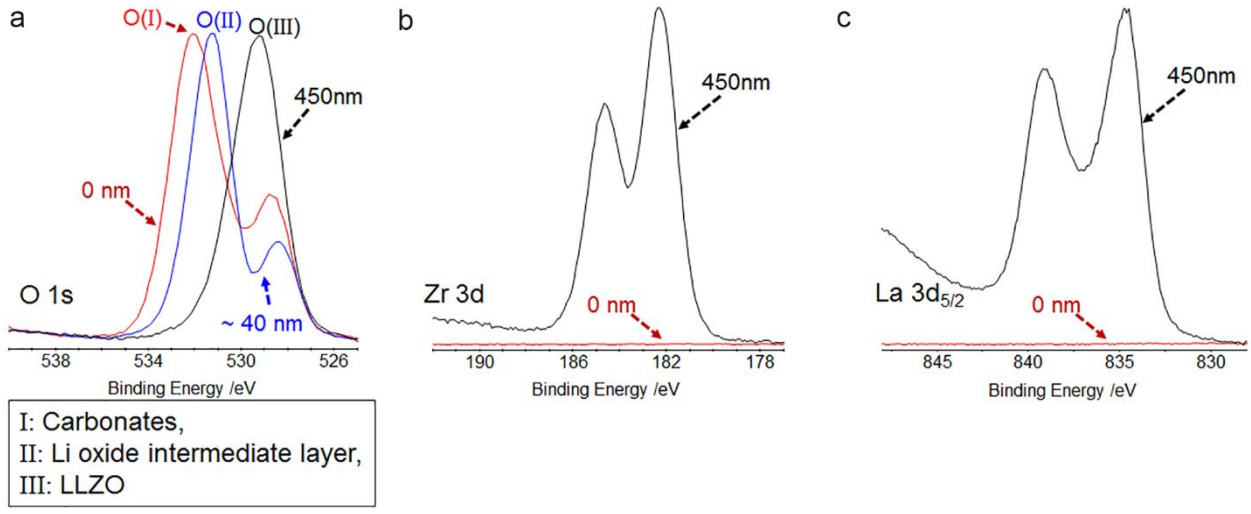

Figure 4.3. XPS analysis of LLZO after sample preparation in ambient air. (a) O 1s and (b) Zr 3d, (c) La $3d_{5/2}$ at different sputtering depths.

4.3.3 SEM/EDS mapping characterization

To characterize the LLZO surface chemistry and topography upon air exposure, SEM was conducted before and after 240 h of air exposure at RH ~ 50%, Figure 4.4. From Figure 4.4, several observations can be made. First, the SEM of the polished LLZO surface with no exposure confirms the uniform morphology where the only features present are the polishing lines (Figure 4.4a). Second, a noticeable change in surface topography is apparent as shown in Figure 4.4b, which is evidence of the secondary phase formation upon prolonged air exposure. The topography changes morphology in stages, first as continuous layers followed by the formation of nodular features. The nodular features, indicated by the arrows in Figure 4.4c, are evidence of non-uniform growth on the LLZO surface. To evaluate the chemical composition of these surface features, energy-dispersive X-ray spectroscopy (EDS) was conducted on a specific region marked by a square in Figure 4.4b. The related EDS maps for Zr, La, O, and C are shown in Figure 4.4e-g. The analysis of the surface composition showed a decrease in La and Zr on the micron size features, Figure 4c. On the other hand, the O and C contents were much higher in the same regions. The EDS spectra, as shown in Figure 4.4d also contains C, which is believed to be contained within the Li_2CO_3 layer. SEM/EDS mapping confirmed that the contamination layer was non-uniform in thickness and density. Further investigations are required to evaluate the cause of this non-uniformity.

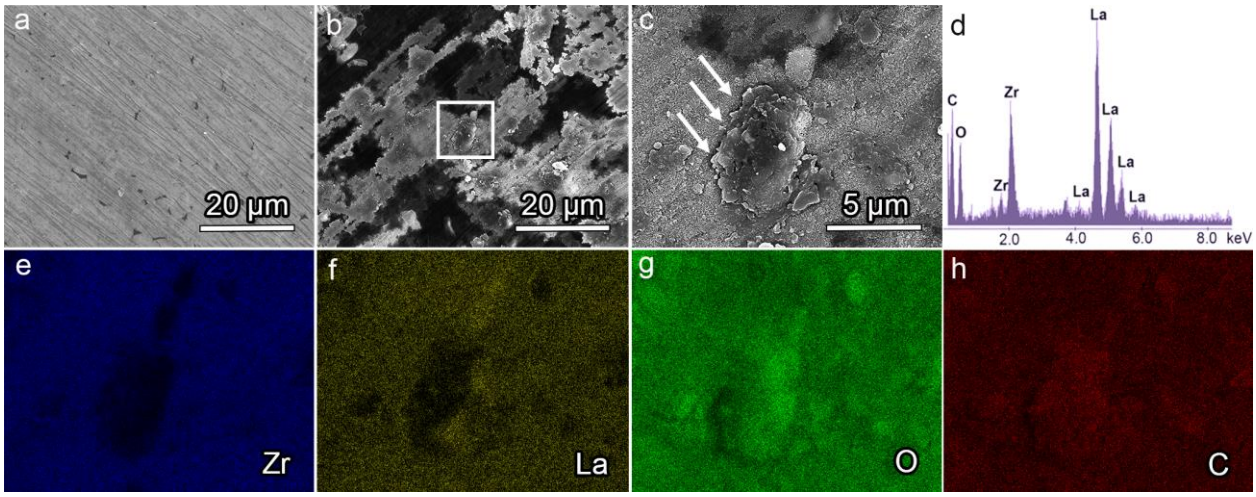

Figure 4.4. Secondary SEM micrographs of the LLZO surface. (a) before exposure to air, (b) after exposure to ambient air, (c) enlarged SEM micrograph of dotted box in (b), (d) the EDS spectrum of the LLZO surface layer and the corresponding EDS mapping of (e) Zr, (f) La, (g) O, (h) C.

4.3.4 Raman spectroscopy and mapping

While EDS analysis provides elemental distribution, correlating the features with stoichiometric compounds requires a complimentary analytical technique. To determine the compounds present, Raman spectroscopy was used. The Raman spectra shown in Figure 4.5a were collected from the surface of LLZO after exposure to ambient and dry air for various times ranging between 0 to 240 h. The Raman spectra obtained from pristine Li_2CO_3 and LiOH are also given in Figure 4.5a as a reference. The Raman spectrum of cubic LLZO with 0 h air exposure agrees well with the spectra reported in literature.[96, 110-112] The Raman spectrum for LLZO can be divided into three regions; a low-energy region (< 300 cm^{-1}), an intermediate-energy region (300-550 cm^{-1}), and a high-energy region (> 550 cm^{-1}) attributed to the vibration of the heavy La cations, Li vibrations and the vibrational stretching modes of ZrO_6 octahedral units, respectively. It is believed that the 1100 cm^{-1} peak can be assigned to Li_2CO_3. The presence of Li_2CO_3 is consistent with previous reports by Larraz *et al*. and Cheng *et al*.[91, 96] In addition, our DFT calculations confirm the reaction between ambient air and LLZO. In Figure 4.5a, the carbonate peak intensity at 1100 cm^{-1} increased with exposure time, indicating growth of a carbonate layer

on LLZO surface. In addition, the lower intensity Li_2CO_3 peak at 1100 cm^{-1} for LLZO exposed to dry air (RH ~ 0.5%) in comparison with ambient air (RH ~ 50%) for the same amount of exposure time suggests that the moisture content during exposure plays a significant role in the formation rate of Li_2CO_3 on the LLZO surface. LiOH is another expected phase to appear on LLZO surface upon air exposure.[91, 96] However, there is an overlapping feature in the Raman spectra for LiOH and the vibration of La cations in LLZO at lower frequency with Raman shift in a range of 210-250 cm^{-1} making deconvolution of these spectra difficult. Hence, Raman mapping and DCLS modeling were used to confirm the existence of LiOH on the LLZO surface. Distribution maps were created to determine and evaluate the complementary information on the coverage and an estimation of the LLZO surface chemistry after air exposure for 240 h by DCLS modeling. Reference spectra of the pure component including cubic LLZO, LiOH and Li_2CO_3 were accumulated. The Raman shift at 1100 cm^{-1} allows for reliable determination of the Li_2CO_3 content with DCLS modeling, since the other phase did not have an overlapping Raman shift in this spectral region. Figure 4.5 compares the spatial distribution of the LiOH and Li_2CO_3 on the LLZO surface. After prolonged exposure to ambient air, the LiOH is distributed almost equally on the LLZO surface and leading to a homogenous distribution as shown in Figure 4.5d-f. However, mapping of Li_2CO_3 indicated that the distribution of Li_2CO_3 was not uniform as shown in Figure 5e and g. The results of Raman spectroscopy are, therefore, consistent with the results of the SEM analysis in identifying the non-homogeneous formation of the contamination layer. These results indicate that exposure of LLZO to air results in the formation of a contamination layer consisting of LiOH and Li_2CO_3.

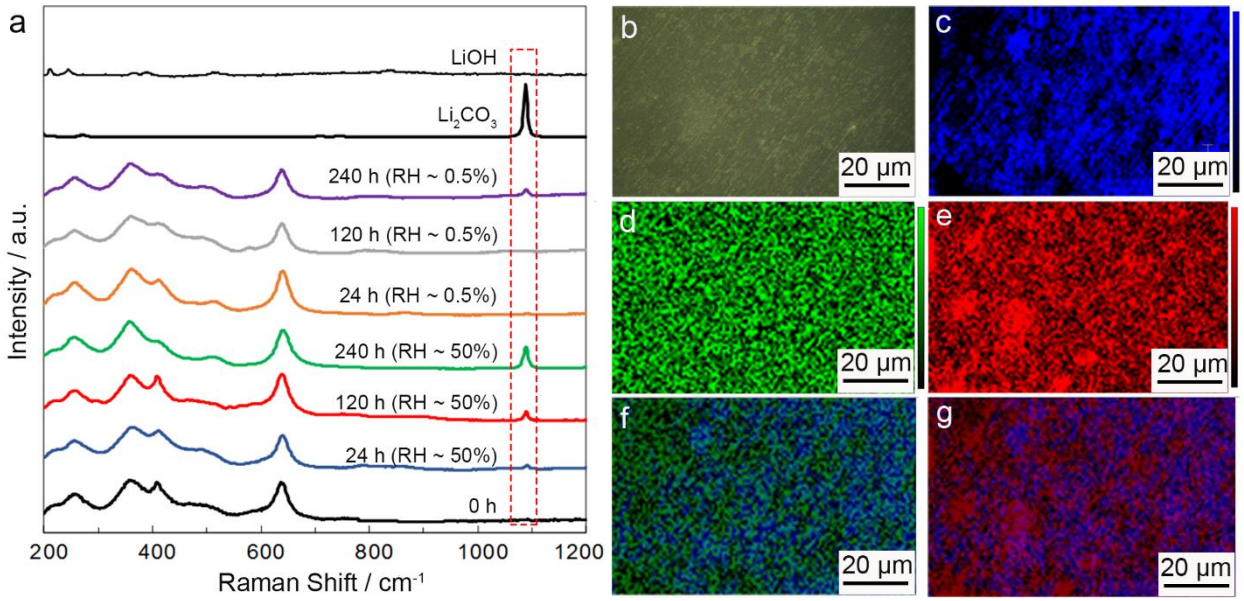

Figure 4.5. Raman analysis of LLZO before and after exposure to ambient and dry air (a). The dotted line highlights growth of the Li_2CO_3 layer on LLZO as a function of exposure time and RH. Topographic analysis of LLZO exposed to air (RH = 50%) for 240 h. (b) Optical image of LLZO, Raman mapping of: LLZO (c), LiOH (d), Li_2CO_3 (e), the overlay of LLZO (blue) and LiOH (green) (f), the overlay of LLZO (blue) and Li_2CO_3 (red), and (g) to show the distribution of different phases on the surface.

4.3.5 TEM characterization

To determine the effect of air exposure on and below the LLZO surface TEM of the LLZO cross section after exposure to ambient air was performed. Figure 4.6 shows a high-angle annular dark field (HAADF) scanning TEM (STEM) image and electron energy loss spectroscopy (EELS) maps of a LLZO cross section after 24 h exposure to ambient air (RH ~ 50%). Three distinct layers can be differentiated in LLZO according to the image contrast in Figure 4.6a, which will be referred to as the base, intermediate, and dark layers. Figure 4.6b, c, d show EELS spectra of O, Li, La, and C, respectively. The O-*K* edge with an onset about 525 eV for all three layers in Figure 6b confirmed the presence of O in all three layers. Figure 4.6c shows the Li-*K* edge peak position and amplitude varies considerably between different layers. The outermost layer, i.e. the dark layer, contains a significantly more Li than the other layers. In contrast, the intermediate layer has significant Li deficiency compared to base and the dark layer.

Additionally, the La-*N4,5* edge on LLZO cross section after air exposure reveals the presence of La in both base and intermediate layers, however the concentration of La in the dark layer is negligible. As the only elements detected from the dark layer are Li, C, and O, it is most likely the dark layer is Li_2CO_3 that formed during air exposure on the LLZO surface. In fact, the fine structure Li-*K* edge in Figure 5c for dark layer matches those from Li_2CO_3 reported previously, confirming the formation of Li_2CO_3.[113] On the other hand, the intermediate layer possesses both La and Li with significantly reduced Li content compared to the base Layer. This can be attributed to the formation of Li_2CO_3 that sequestered Li and possibly some O from LLZO, leading to a phase transition and the formation of the intermediate layer beneath the Li_2CO_3 layer. Moreover, the Li depleted interlayer could be partially protonated as reported previously by Larraz *et al.* and Cheng *et al.*; Li^+/H^+ exchange occurs in this layer to maintain charge neutrality upon reaction with H_2O and CO_2 from ambient air.[96-97] The TEM images of LLZO cross-section after 120 and 240 h air exposure are provided in Figure 4.7. These images show a considerable increase in the thickness of intermediate and dark layers. This implies the contamination layer formation continues to grow with longer exposure time.

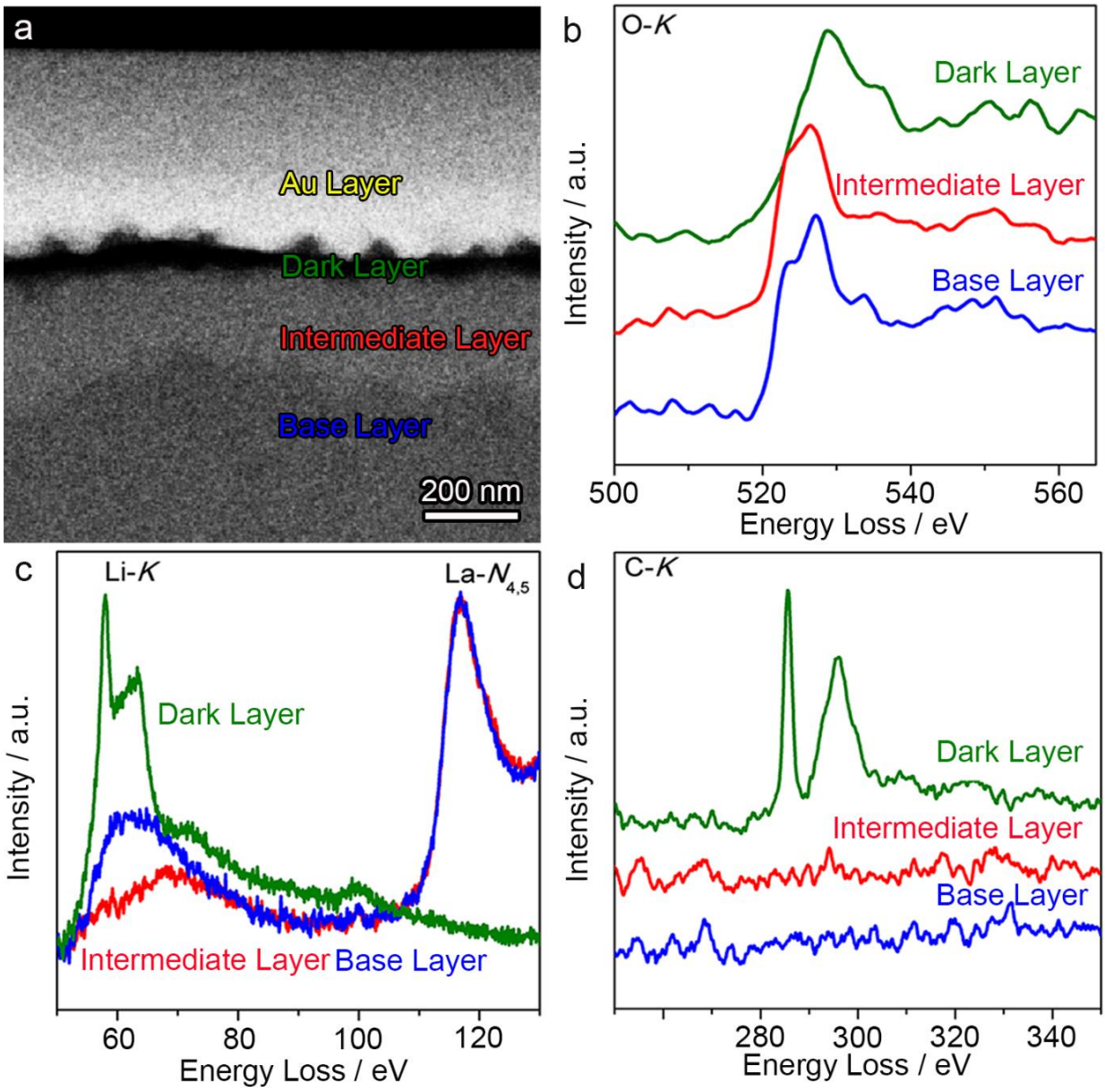

Figure 4.6. Cross sectional TEM image of LLZO pellet after 24 h air exposure to ambient air with 50 % RH (a), and corresponding EELS maps of oxygen (O-*K*) (b), lithium (Li-*K*) and lanthanum (La-*N4,5*) (c) and carbon (C-*K*) (d) on all the three layers (base layer, intermediate layer and dark layer) detected in LLZO after air exposure. The last layer above the dark layer is sputtered gold that was used to prevent electron beam damage.

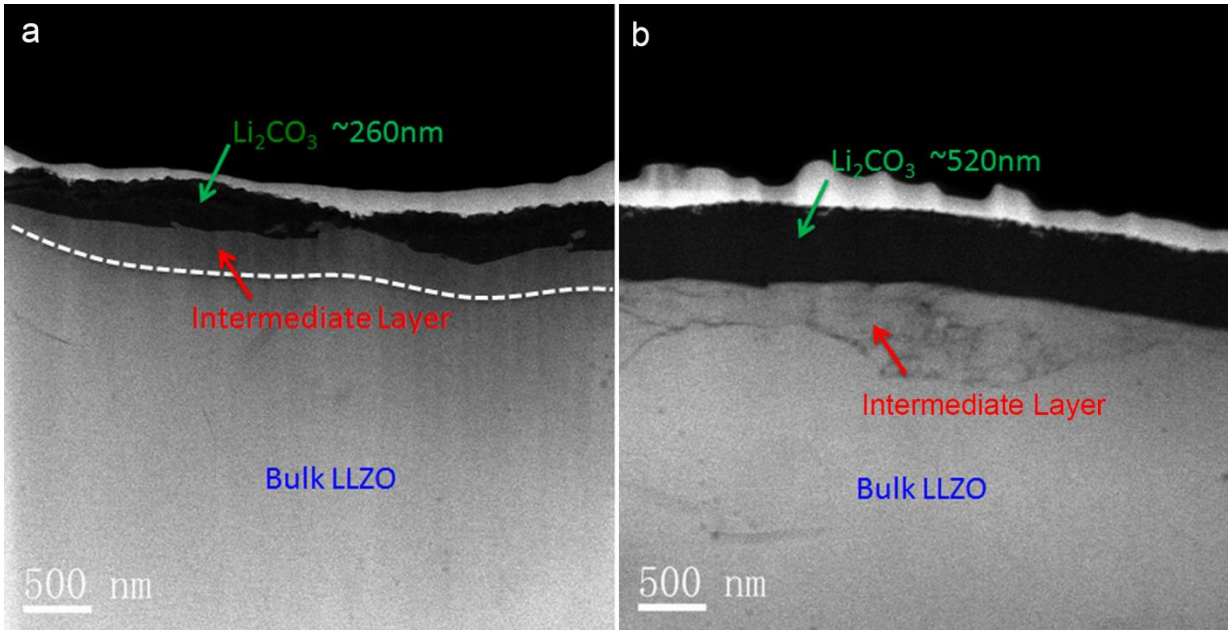

Figure 4.7. Cross sectional TEM image of LLZO pellet after (a) 120 h, and (b) 240 h air exposure to ambient air with 50 % RH (a), all the three layers (base layer, intermediate layer and dark layer) detected in LLZO after air exposure. The last layer above the dark layer is sputtered gold that was used on the exposed surface for protection.

4.3.6 XPS surface characterization

At the beginning of our analysis, the XPS depth profiling, ostensibly, offered an effective way to characterize the composition of the LLZO surface after processing and preparation in air. The results identified the contaminant compositions and pointed to the gradual removal of contamination during sputtering. To gain further insight into the kinetics of surface contamination upon air exposure and evaluate the change in surface chemistry, XPS analysis was conducted again as a function of air exposure. However, compared to the analysis using the initial XPS data in Figure 4.2, care was taken to clean the LLZO surface by polishing in an inert argon atmosphere. The sample was transferred immediately after polishing into the XPS chamber using a load locker to prevent any air exposure. Initial measurements on the polished LLZO with no air exposure were made, followed by the controlled and deliberate exposure to ambient air (RH ~ 50%) for predetermined periods. The cumulative air exposure time was 401 minutes. The results are reported in Figure 4.8. For the sake of clarity, the C 1s and O 1s

analysis are only shown in Figure 4.8a. At t = 0, the C 1s core level spectra show mainly a C 1s peak at 284.8 eV that can be assigned to adventitious carbon that existed in the glovebox or in the XPS vacuum chamber. The absence of a carbonate-type peak at a BE of ~289 eV suggests that the LLZO surface was effectively cleaned and transferred to the XPS instrument with no exposure to air. Additionally, the O 1s signal shows a strong peak at BE ~ 531 eV and a weaker peak at ~ 528.5 eV. The former peak was reported by Cheng *et al*. for LLZO that was polished in the glovebox, but the latter was not.[97] It is worth noting that the O 1s peak for LLZO after sputtering down to ~450 nm (for the sample discussed above) was found to be at ~ 528 eV, which is similar to the relatively weak peak observed here. Thus, it is reasonable to conclude that the peak at 528.5 eV represents O in bulk LLZO (III), while the peak at BE ~ 531 eV represents component (II), which could be the reaction layer due to trace amounts of oxygen in the glovebox or nominal contamination in the evacuated sample load locker. Since the XPS signal intensity decays exponentially, the surface oxide signal is masking the lattice O signal corresponding to pristine LLZO (III) at 528.5 eV. The atomic ratio of Zr to O (III) at t = 0 was found to be 1.0: 3.3 (for stoichiometric LLZO, it should be 1.0: 6.0), thus it reasonable to assume that the extra Zr is incorporated in component (II) and the latter is not just simply Li oxide/hydroxide. With subsequent air exposure, the carbonate buildup completely dominates the O 1s signal (I). Upon the initial 7 min of air exposure, clear evidence of Li_2CO_3 is detected and maintained throughout the duration of the 401 minutes cumulative time. The O 1s (I) feature corresponding to carbonate also grows concomitantly (Figure 4.8, right panel).

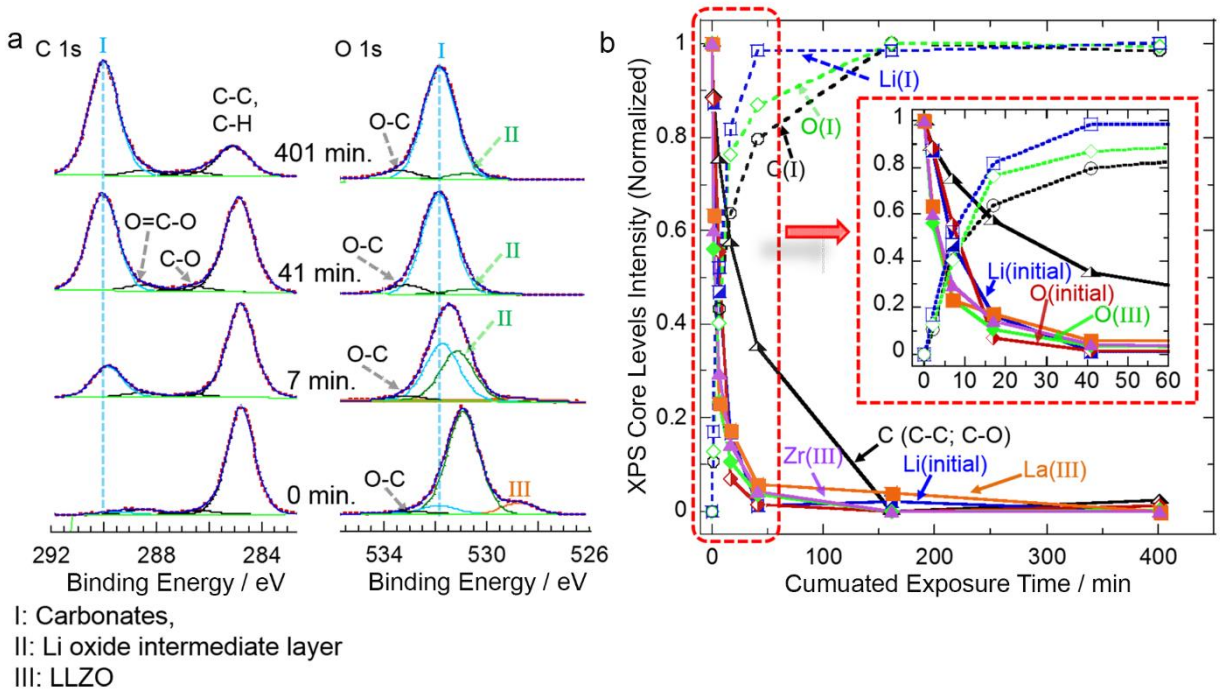

Figure 4.8. XPS analysis of LLZO after polishing and exposure to ambient air for various exposure time. (a) C 1s and O 1s, (b) Normalized XPS core levels intensity vs cumulated air exposure time. The inset is a zoom-in on the first 60 minutes of air exposure**.**

Figure 4.8b shows XPS core levels spectra for C, O, Li, Zr, and La features vs. cumulative exposure time. These features are based on peak fittings as discussed above. For the spectrum acquired at 161 minutes of air exposure, if the C, O, and Li values are normalized using the C value, it is clear the overall stoichiometry is close to Li_2CO_3. Hence, it can be deduced that the material growing on the surface due to exposure to air is Li_2CO_3. The same investigation was done for Zr 3d and La $3d_{5/2}$ core level for exposure time between 0 to 401 minutes (Figure 4.9). The Zr and La features quickly diminished with air exposure and again are not detectable after 161 minutes of air exposure. This indicates that this period was sufficient to form a contamination layer that is thicker than 10 nm (the detection limit for XPS) and this layer was mainly Li_2CO_3.

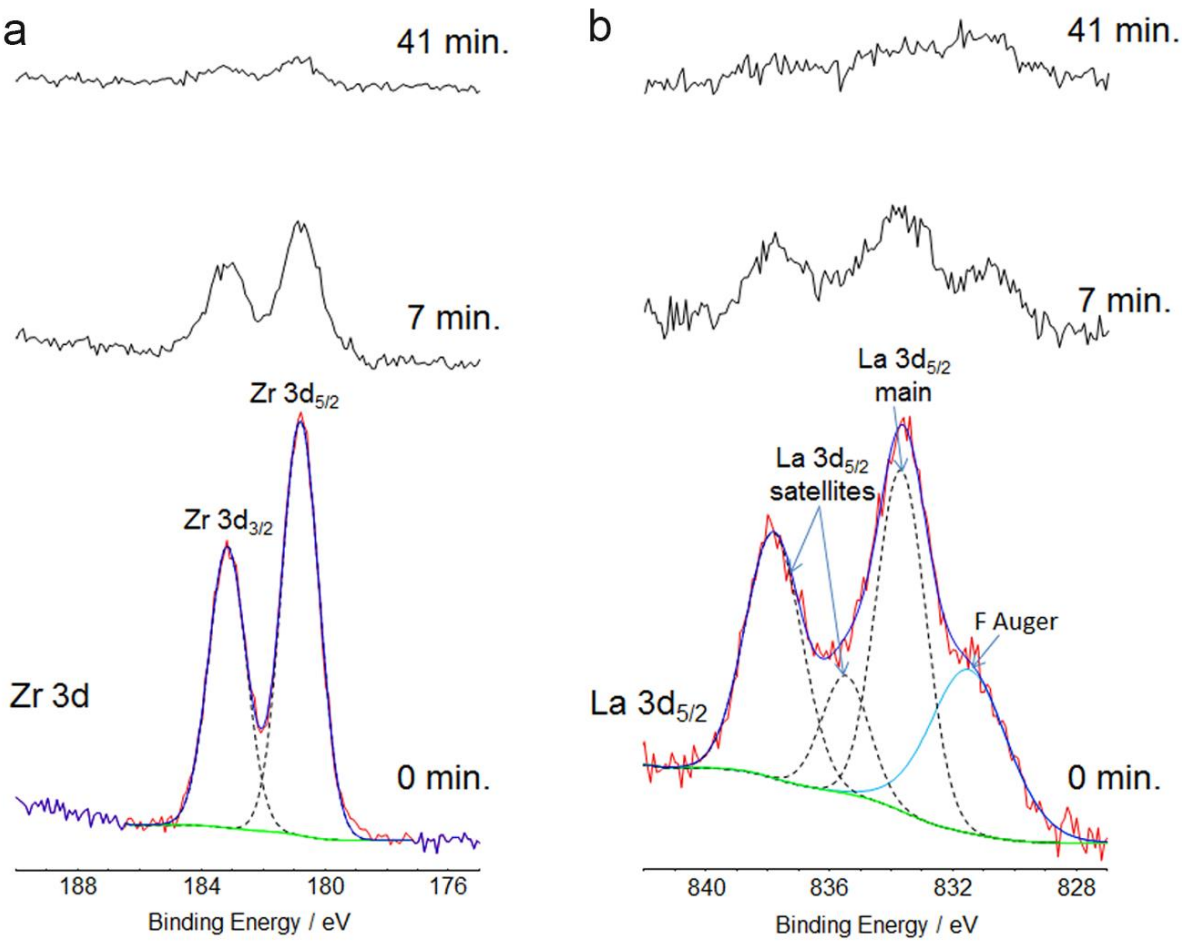

Figure 4.9. XPS analysis of LLZO after polishing and exposure to ambient air for various exposure time (0 min to 41 min), (a) Zr 3d 1s, and (b) La $3d_{5/2}$.

4.3.7 Electrochemical measurements

Electrochemical impedance spectroscopy of Li-LLZO-Li symmetrical cells was performed to evaluate the impact of the contamination layer on the Li-LLZO interfacial resistance. A comparison of the impedance spectra for Li-LLZO-Li cells consisting of LLZO exposed to ambient and dry air is shown in Figure 4.10. The impedance data were fitted with an equivalent circuit as shown in Figure 4.10a. The impedance data of a Li-LLZO-Li cell consists of three distinct constant phase elements (CPE) which were interpreted to represent: Li-LLZO interfacial resistance (R_{int}) between 120 kHz and 1 Hz, grain boundary resistance (R_{gb}), between 1 MHz and 120 kHz; and bulk LLZO resistance (R_{bulk}), between 7 MHz and 1 MHz. The capacitance values,

Q (F), resistance values, and α values were refined from the equivalent circuit modeling for the interfacial resistance, grain-boundary, and bulk transport processes for all samples are shown in Table 4.2. α is the ideality coefficient for each CPE; the closer to unity, the closer the fit between experimental and idealized behavior.[72] The capacitance values should be on the order of 10^{-6} F for the interfacial resistance, 10^{-8}-10^{-11} F for the grain boundaries, and 10^{-12} F for the bulk transport.[72-73]

The bulk conductivity of LLZO determined from the high frequency range is largely independent of RH and exposure time. The values are in good agreement with previous studies for bulk Al doped LLZO, which is in the 0.2 to 0.5 $mS.cm^{-1}$ range. [114-115] The α values for the bulk LLZO and grain boundaries were close to unity and in excellent agreement for all cells, thus confirming the consistency in EIS spectra among all samples. On the other hand, the α values for the interfacial resistance CPEs were less than 0.90 when the LLZO was exposed to air for longer times. This could be a result of the interposition of the contamination layer, which introduced more than one interface CPE, thus deviating from idealized interface resistance. The R_{int} determined for cells containing LLZO with no exposure (b), 24 h (c), 120 h (d), and 240 h (e) exposure to ambient air (RH ~ 50%) showed an increase with exposure time regardless of moisture content (Figure 4.10). As expected, the lowest R_{int} was observed for LLZO that was not exposed to air after surface grinding in the glovebox (of 54 $\Omega.cm^2$). This value is the lowest Li-LLZO interface resistance measured using EIS and equivalent circuit modeling.[115-116]

After 24 h of exposure, the R_{int} increased by approximately 3X to 145 $\Omega.cm^2$, likely due to the formation of the contamination layer described above. After 120 and 240 h of exposure, the R_{int} further increased to 12,085 $\Omega.cm^2$ and 36,782 $\Omega.cm^2$, respectively. Although the DFT could predict the energetics of contamination, the reaction kinetics were too complicated to determine a

reaction rate. Further complicating the reaction kinetics was the observation that the Li_2CO_3 cracked, thus likely resulting in non-uniform Li-LLZO interface contamination rates. Nevertheless, our measurements suggest that R_{int} increases rapidly in the beginning stages of exposure and then tapers off at longer exposure time, consistent with a reduction in kinetics as the reaction progresses. To further test the hypothesis that RH affects the kinetics of the contamination reaction, the same exposure time tests were conducted in dry air (RH ~ 0.5%). As shown in Figure 4.10, R_{int} for LLZO exposed to dry air was considerably lower compared to LLZO exposed to ambient air for the same exposure times (Figure 4.10c-e). For example, at 120 h of exposure, the R_{int} in ambient air increased by approximately 10X more that the R_{int} when exposed to dry air. Thus, higher RH in ambient will accelerate the contamination layer growth kinetics compared to dry air.

The reaction between LLZO and air as a function of RH and time was analyzed using DFT calculations and several materials characterization techniques. DFT calculations determined that LLZO reacts with air resulting in protonation of LLZO and the subsequent formation of LiOH intermediate and Li_2CO_3 contamination layers. XPS measurements were conducted on the LLZO surface after processing in air with no deliberate efforts to limit contamination. The XPS analysis revealed that, LiOH and Li_2CO_3 formed on the LLZO surface, consistent with the computed reaction thermodynamics. Similar analysis was repeated, but by taking precautions to prevent un-intentional exposure to air such that all reactions were deliberate and controlled. This was accomplished by mechanically cleaning (grinding) LLZO surfaces in an argon glovebox and exposing to air with RH ~ 0.5 or 50 % for specified times up to 240 h. Detailed characterization on LLZO surfaces was performed using SEM/EDS mapping and Raman spectroscopy to study the

chemistry of the LLZO surface after exposure to air. SEM micrographs showed the contamination layer formed on the surface was non-uniform. Raman spectroscopy confirmed that the formation of Li_2CO_3 was sensitive to the relative humidity, i.e. the higher the relative humidity, the faster the Li_2CO_3 grew. Furthermore, TEM characterization of subsurface LLZO demonstrated that exposure to air resulted in three distinct layers. It was observed that the formation of Li_2CO_3 sequestered Li and possibly O from LLZO, leading to a phase transition immediately below the Li_2CO_3. Immediately below the intermediate layer, pure LLZO was observed. Additional XPS analyses determined the contamination layer formed in 7 minutes after exposure to ambient air (RH ~ 50%). EIS analysis was conducted to correlate the surface chemistry with R_{int}. As expected, the longer the exposure time and the higher the relative humidity, the higher R_{int}.

The practical implications of this work are two-fold. First, R_{int} increases by only a factor of 2 to 3 upon exposure to dry or ambient air for periods of up to 24 h. In both cases the resulting interface resistance are some of the lowest values reported. This indicates that despite a relatively thin contamination layer that increases R_{int}, LLZO is stable in air. Second, the relatively stable behavior in air over moderate exposure times suggests that it may be feasible to process LLZO electrolyte membranes and/or solid-state LLZO-based batteries in air, which could reduce manufacturing costs.

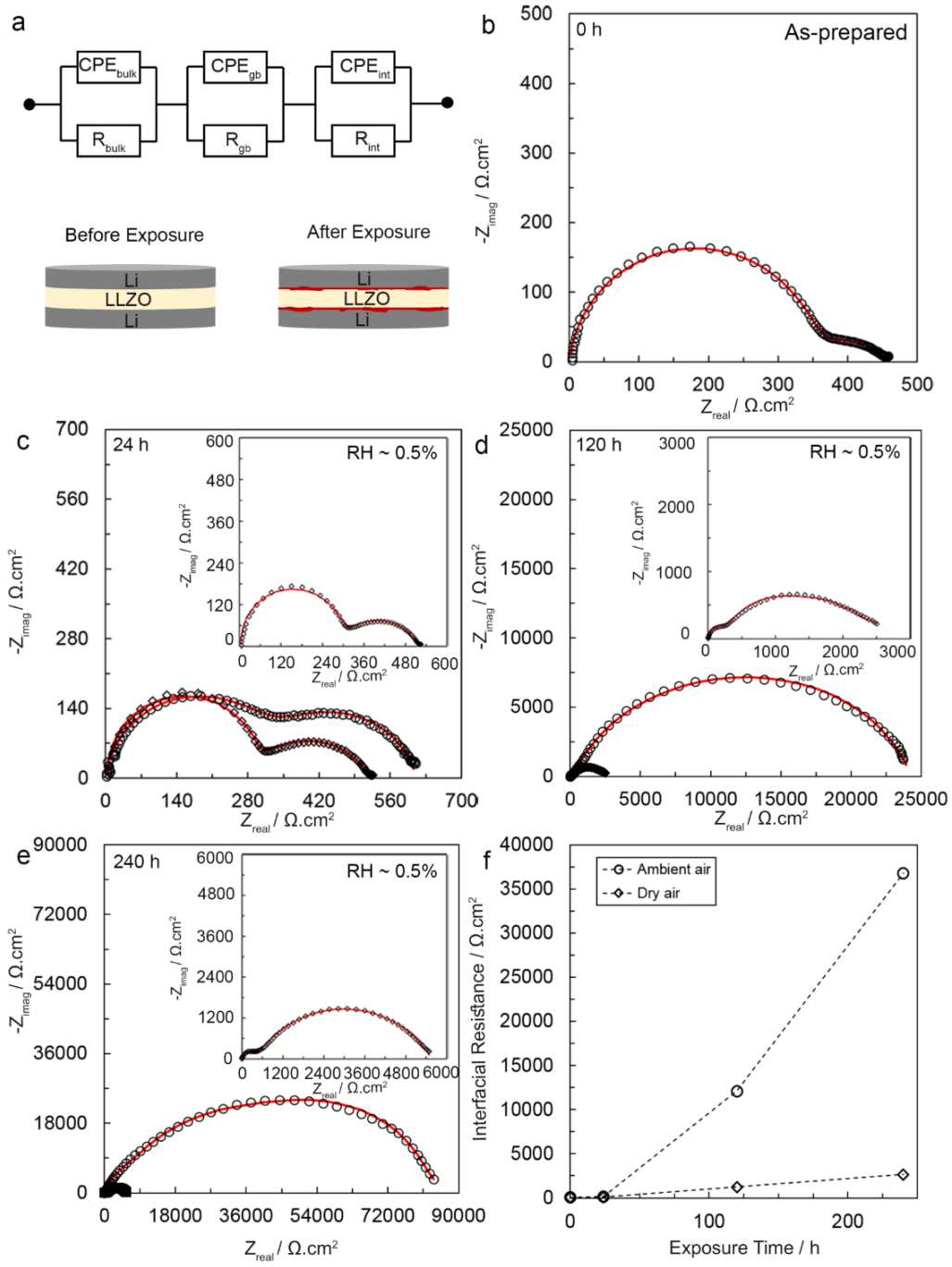

Figure 4.10. Impedance spectra measured at room temperature for Li-LLZO-Li cells after various exposure times to ambient (○) and dry air (◊). (a) Schematic depicting the asymmetric Li-LLZO-Li cell before and after air exposure and equivalent circuit modeled used for fitting EIS data, (b) 0 h, (c) 24 h, (d) 120 h, (e) 240 h. The insets show the impedance spectra for Li-LLZO-Li for samples exposed to dry air. Markers indicate experimental data and the solid lines are simulated lines extrapolated from the equivalent circuit modeling, and (e) interfacial resistance at Li-LLZO interface as function of time after exposure to ambient air (○) and dry air (◊), (f) The Li–LLZO interfacial resistance versus time after exposure to ambient and dry air.

Table 4.2. Summary of fitted data for electrochemical impedance spectroscopy of the Li-LLZO-Li symmetric cells.

Sample	Q_{bulk} (F)	α_{bulk}	R_{bulk} ($\Omega.cm^2$)	Q_{gb} (F)	α_{gb}	R_{gb} ($\Omega.cm^2$)	Q_{int} (F)	α_{int}	R_{int} ($\Omega.cm^2$)
0 h	8.3×10^{-12}	1	339	6.6×10^{-8}	0.94	5	1.1×10^{-6}	0.80	54
24 h-RH~50%	4.9×10^{-12}	0.99	310	9.7×10^{-8}	0.96	10	0.5×10^{-6}	0.85	145
120 h-RH~50%	5.8×10^{-12}	0.99	305	4.2×10^{-8}	0.98	30	1.1×10^{-6}	0.77	12085
240 h-RH~50%	9.8×10^{-12}	0.93	296	8.1×10^{-8}	0.90	120	1.2×10^{-6}	0.87	36782
24 h-RH~0.5%	8.1×10^{-12}	1	320	4.7×10^{-8}	0.98	6	1.3×10^{-6}	0.89	100
120 h-RH~0.5%	3.6×10^{-12}	1	289	4.3×10^{-8}	0.90	7	1.6×10^{-6}	0.88	1235
240 h-RH~0.5%	2.6×10^{-12}	0.94	380	9.1×10^{-8}	0.92	35	1.6×10^{-6}	0.88	2650

4.4 Conclusions

Understanding of LLZO the morphology, surface chemistry, and stability of LLZO is essential in the development of next-generation solid state batteries employing LLZO as solid electrolyte. Toward these goals, the present study has examined the effect of air exposure on LLZO surface chemistry and Li-LLZO interfacial resistance. First, DFT calculations were used to evaluate the LLZO air stability. The calculations reveal that LLZO readily reacts with humid air; the most favorable pathway involves protonation of LLZO and formation of an LiOH intermediate. Subsequent exposure to CO_2 (in air) converts the LiOH to Li_2CO_3 (Figure 4.11). Detailed XPS data showed that LiOH and Li_2CO_3 are present on the LLZO surface after exposure to air. These data agree closely with the results from DFT calculations. Furthermore, SEM analysis indicated the topography changes and non-uniform formation of contamination

layer on surface. The extent of Li_2CO_3 formation on LLZO surface was shown to depend strongly on RH level and exposure time using Raman spectroscopy. TEM analysis identified the formation of Li deficient LLZO beneath the Li_2CO_3 contamination layer, which is consistent with reaction pathway 3a-b where LLZO loses Li in exchange for protons. Moreover, the Li-LLZO interfacial resistance was correlated to LLZO surface chemistry. It was shown that the formation of contamination layers at the LLZO surface has a significant effect on the Li-LLZO interfacial resistance. The higher the extent of contamination the higher the Li-LLZO interfacial resistance.

This work suggests that the composition of the LLZO surface has a vital impact on the Li-LLZO interfacial resistance. It has been shown while LLZO can be synthesized, and densified in ambient air, measures must be taken to prevent subtle surface contamination to enable relatively low Li-LLZO interfacial resistance.

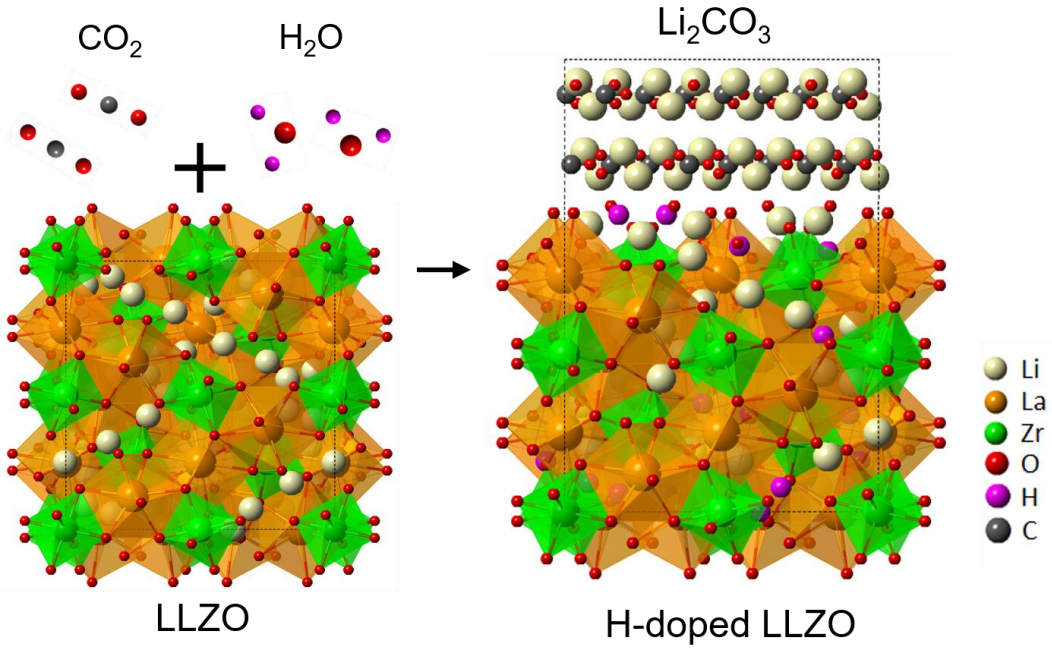

Figure 4.11. LLZO reacts with humid air, the most favorable reaction pathway involves protonation of LLZO and formation of Li_2CO_3. The air exposure-induced contamination layer impacts the Li-LLZO interfacial resistance.

CHAPTER V

Surface chemistry mechanism of ultra-low interfacial resistance in the solid-state electrolyte $Li_7La_3Zr_2O_{12}$

5.1 Introduction

A transition from a fossil fuel-based economy to one based on renewable resources has sparked interest in the development of energy storage devices with higher energy density, enhanced safety, and reduced cost.[23] Li-ion batteries (LIBs) represent a promising technology for near-term energy storage needs; however, for emerging applications such as electric vehicles, a step-change increase in battery performance is highly desirable.

Toward this goal, specific energies and energy densities exceeding 500 $Wh.kg^{-1}$ and 1000 $Wh.l^{-1}$, respectively, with costs less than \$100 kWh^{-1}, could be achieved through the development of solid-state electrolytes (SSE).[8] The garnet-type SSE, based on the nominal formula $Li_7La_3Zr_2O_{12}$ (LLZO), is unique in that it is a fast Li-ion conductor (1 $mS.cm^{-1}$ at 298K), exhibits sufficient mechanical properties,[54] and is also chemically and electrochemically stable against metallic Li.[46] Despite these promising attributes, additional challenges must be overcome before solid-state batteries (SSBs) based on LLZO are viable. Demonstrating low Li-LLZO interfacial resistance ($R_{Li\text{-}LLZO}$) is a

critical milestone along the path to commercialization. While several studies have characterized $R_{Li\text{-}LLZO}$, nearly all report values significantly higher than conventional LIBs employing liquid electrolytes (~10 $\Omega.cm^2$).[91, 115, 117] Thus, strategies to reduce $R_{Li\text{-}LLZO}$ to values comparable to, or lower than, LIBs are needed.

Recently, coating of the LLZO surface was investigated to reduce $R_{Li\text{-}LLZO}$. For example, Tsai *et al.* sputter coated Au on LLZO and demonstrated a $R_{Li\text{-}LLZO}$ of 58 $\Omega.cm^2$.[118] It was hypothesized that the Au coating provided uniform conductivity at the Li-LLZO interface, lowering $R_{Li\text{-}LLZO}$. In related work, Han *et al.* demonstrated that an Al_2O_3 coating could reduce $R_{Li\text{-}LLZO}$ to an extrapolated value of 1 $\Omega.cm^2$, which was attributed to enhanced Li wettability of the LLZO surface.[119] However, the mechanism of how surface modifications lead to improved performance has not been explicitly determined.

While the use of coatings can in some instances improve performance, the underlying physical and chemical mechanisms that control interfacial resistance are not well understood. Understanding the coupling between interfacial chemistry, Li wettability, and interfacial resistance would accelerate the rational design of engineered interfaces having low $R_{Li\text{-}LLZO}$. Such an understanding would also address the question of whether low interfacial resistance could be achieved without the need for coatings, as these add additional processing steps, create additional interfaces, and could compromise cycle life if the coating does not maintain integrity upon cycling.

In this study, we demonstrate that the Li-LLZO interfacial resistance can be nearly eliminated (2 $\Omega.cm^2$) through a simple coating free process for removing the surface contamination layer on LLZO. We provide a mechanistic understanding of the interplay

between interfacial chemistry and electrochemical performance at solid-solid interfaces in SSBs. This understanding provides design rules for engineering low-resistance interfaces.

The importance of Li wettability in achieving low-resistance Li-SSE interfaces in SSBs has been discussed in a few recent studies.[118, 120] However, a quantitative evaluation of Li wettability as a function of SSE surface chemistry is currently lacking. To address this, molten Li contact angle measurements using a sessile drop test were conducted on several relevant surfaces including LLZO with various surface chemistry. Trends in the measured contact angles are consistent with those calculated with density functional theory (DFT), and demonstrate the intimate connection between surface chemistry and Li wettability.

Our study quantitatively demonstrates the unified relationship between interfacial chemistry, lithium wettability, and facile charge transport. Equipped with this mechanistic understanding, we demonstrate that exerting rational control over interfacial chemistry enables a straightforward pathway towards commercially viable SSBs.

5.2 Experimental

5.2.1 LLZO specimen preparation

Cubic $Li_{6.25}Al_{0.25}La_3Zr_2O_{12}$ was prepared through a conventional solid-state technique. Li_2CO_3 (1 µm, Alfa Aesar, Ward Hill, MA), $La(OH)_3$ (1 µm, Alfa Aesar), Al_2O_3 (0.05 µm, Mager Scientific Inc.), and ZrO2 nanopowder (30-60 nm, Inframat, Advanced Materials) were weighed in stoichiometric ratios. 0.25 mole Al was added to stabilize the cubic phase at room temperature. Excess Li_2CO_3 was used to compensate for Li volatilization during calcination. The powder mixture was thoroughly mixed with a planetary ball mill (PM 100; Retsch) for 8 hours at 350 rpm. The precursors were milled

in 5 minute intervals, by milling for 5 minutes and resting for 5 minutes repeatedly. The powder mixture was cold-pressed into pellets using a 25.3 mm diameter stainless-steel die (MTI Corporation) at a constant 8000 N force for 2 min. The cold-pressed pellets were placed in a tubular furnace (Carbolite LTD) and calcined at 1000°C for 4 h under 2 $L.min^{-1}$ flowing dry air. The pellets were set on MgO boats (Ozark Technical Ceramics) during calcination. The calcined pellets were manually ground using an agate mortar and pestle. The ground powders were then passed through a 75 μm sieve. After grinding and sieving, the calcined powder was densified using a custom rapid induction hot-press (RIHP) at 1100°C and 62 MPa for 1 h in graphite dies under argon shielding gas to achieve > 97% relative density. Each sample was cut into 1 ± 0.2 mm discs using a slow speed diamond saw. The discs were dry polished using 400 grit SiC sandpaper in air to ensure the parallel faces.

5.2.2 Surface conditioning

Various surface conditioning processes including dry polishing (DP), wet polishing (WP), and heat treatment (HT) were used. For DP, LLZO samples were polished manually using 400, 600, and 1200 grit sandpaper (Norton Corporation) in air without polishing fluid. For WP, an automated polisher (EcoMetTM 300 Pro, Buehler) was used. First, LLZO samples were ground using 1200 sand paper (Norton Corporation). After grinding, the samples were polished on Technorton® polishing cloth (Leco Corporation) loaded with glycol-based diamond paste extender as the polishing fluid (Leco Corporation) and diamond polishing abrasives. The diamond polishing abrasive sequence ranged from 15, 6, 1 and down to 0.5 μm. After each diamond abrasive, samples were rinsed with ethanol to remove the residual polishing fluid from surface. Immediately

after polishing, samples were transferred to an argon-filed glovebox for HT. Heat treatment was conducted prior to surface chemistry characterization, contact angle measurements and electrochemical characterization by placing the samples in a MgO boat and heating to temperatures between 200 to 500°C in 100°C intervals in a muffle furnace (MTI Corporation) for 180 min using 4°C.min^{-1} as heating and cooling rate.

5.2.2 Surface chemistry characterization

A Kratos Axis Ultra was used for all XPS experiments. A custom o-ring sealed air-tight transfer device was used to transfer samples into the XPS tool without air exposure. Survey scans used a pass energy of 160 eV and were quantified using Shirley backgrounds and Kratos sensitivity factors for the La 3d, Zr 3p, C 1s, O 1s, and Li 1s peaks in Casa XPS. Core scans used a pass energy of 20 eV and were energy calibrated using the C-C bond energy at 284.8 eV. The O 1s peak was fitted with 3 species, LiOH at 531.1 eV,[121] Li_2CO_3 at 532 eV,[122] and oxide species at 528.6-529 eV.[122] The C 1s peak was fitted with 4 species, adventitious carbon at 284.8 eV, which was used to calibrate the spectra, C-O at ~286 eV,[123] O-C=O at 289 eV,[124] and Li_2CO_3 at 290 eV.[122]

5.2.3 Contact angle measurements

Cold-pressed Li_2CO_3 and LLZO with various surface treatments were placed on a hotplate at 300°C inside an argon-filled glovebox. The temperature was measured using a thermocouple placed on the surface of the sample to ensure the sample temperature was higher than melting temperature of Li (T>180°C). Subsequently, molten Li was injected on the surface with a stainless-steel syringe. The stainless-steel syringe was also heated to T>180°C to avoid solidification of molten Li. A droplet of molten Li was placed on LLZO surface after each cleaning step to measure the contact angle between Li and

LLZO. The contact angle measurement was performed by determining the tangent angle of the Li liquid drop with the sample surface. In this method, the shape of a droplet resting on a solid surface is dependent on the mechanical equilibrium of the drop under the three interfacial tensions including solid-vapor (γ_{SV}), solid-liquid (γ_{SL}), and liquid-vapor (γ_{LV}). This could be described by the Young-Dupree's Equation (1):

$$\gamma_{SV} = \gamma_{SL} + \gamma_{LV} cos\theta \quad (1)$$

where θ is the contact angle, the drop made on a solid surface. A high-resolution camera (Grasshopper GRAS-50S5M-C) with a Fujinon HF75SA-1 lens was used to capture the image and measure contact angles. The contact angle plugin tool in ImageJ software was used to measure the contact angle.

5.2.4 First principle calculations

First-principles calculations were performed using density functional theory (DFT) with a plane wave basis set and the projector augmented wave (PAW) method,[101] as implemented in the Vienna ab initio Simulation Package (VASP).[99] The semi-local generalized gradient approximation (GGA) of Perdew, Burke, and Ernzerhof (PBE)[102] was used for the exchange-correlation energy. For LiOH, van der Waals density functional (vdW-DF2)[125] was additionally used to describe the weak interaction between LiOH (001) layers. An energy cutoff of 450 eV was used for the plane wave basis. The Brillouin zone was sampled using the Monkhorst–Pack scheme,[105] with 3 × 3 × 1, 4 × 4 × 1 and 4 × 4 × 1 k-point meshes used for the Li-LLZO, Li-Li_2CO_3, and Li-LiOH interfaces, respectively. The convergence criterion for the electronic self-consistency loop was set to 10-5 eV, while atomic positions were relaxed until atomic forces were less than 0.05 eV.$Å^{-1}$.

The optimal lattice parameters for bulk cells were obtained by fitting total energy vs. volume data to the Murnaghan equation of state, as shown in Table 5.1.[106] The LLZO slab was constructed based on the cubic polymorph with partial occupancies of 0.542 and 0.448 on the 24d and 96h Li-sublattice sites, respectively. A (001) Li slab with 20 layers was used to calculate the surface energy of Li, resulting in 0.452 $J.m^{-2}$. The Li-LLZO, Li-Li_2CO_3, and Li-LiOH interfaces were assembled using geometries that minimize interfacial strain; periodic boundary conditions in directions parallel to the interfacial plane were accommodated by adjusting the lattice constants of Li to match the dimensions of LLZO, Li_2CO_3, or LiOH. The number of atoms in the interface supercell, the lattice parameters for the interface, and the in-plane strain of Li are listed in Table 5.2 for all three interface systems. A vacuum layer of 8 Å was included in the interface supercells; each supercell contained one interface. The interfacial distance was determined by rigidly displacing the two slabs along the interface normal, and fitting the resulting energy vs. displacement data to the Universal Binding Energy Relation (UBER).[126] This procedure resulted in minimum-energy interfacial distances of 1.96, 3.04, and 2.32 Å for Li-LLZO, Li-Li_2CO_3, and Li-LiOH, respectively. Ionic relaxations were then performed for the three interfaces starting from interfacial separations predicted by the UBER fit. For the Li-LLZO interface, which had the largest supercell size (570 atoms), atoms in the "back" half of each slab (i.e., the portion farthest from the interface) were fixed at their bulk-like positions. The Li-Li_2CO_3 and Li-LiOH interfaces were fully-relaxed without fixing any atom positions. Testing on these two systems revealed that the work of adhesion was not strongly influenced by the presence/absence of these constraints.

Table 5.1. Calculated lattice constants for bulk Li, LLZO, Li_2CO_3, and LiOH.

Sample/Lattice constant	a (Å)	b (Å)	c (Å)	α (°)	β (°)	γ (°)
Bulk Li	3.436	-	-	90	-	-
Bulk LLZO	13.026	-	-	90	-	-
Bulk Li_2CO_3	8.432	5.016	6.312	90	114.67	90
Bulk LiOH	3.535	-	4.408	90	-	-

The optimization of the translation state within the interfacial plane and the interfacial distance for the Li-LLZO and Li-Li_2CO_3 interfaces are shown in Figures 5.1 and 5.2, respectively. Contour plots of W_{ad} were obtained by translating the Li slab amongst many configurations at a constant interfacial distance. The lowest interface in the contour plot was then used to calculate interfacial distance by fitting to the UBER. For LiOH, the values of W_{ad} upon translating the Li slab were nearly identical. Optimization of the interfacial distance for the Li-LiOH interface using the UBER is shown in Figure 5.2b.

Table 5.2. Number of atoms in the supercell, lattice parameters in the interfacial plane, the in-plane strain of Li, the calculated W_{ad}, and the contact angle for the Li-LLZO, Li-Li_2CO_3, and Li-LiOH interfaces.

Interface	No. of atoms	a (Å)	b (Å)	$\varepsilon_{x,Li}$ (%)	$\varepsilon_{y,Li}$ (%)	W_{ad} (J.m^{-2})	Contact angle (°)
Li-LLZO	570	18.421	18.421	-0.43	-0.43	0.667	61.6
Li-Li_2CO_3	252	16.864	10.032	-1.83	-2.67	0.096	142.0
Li-LiOH	260	14.140	14.140	-0.18	-0.18	0.191	125.3

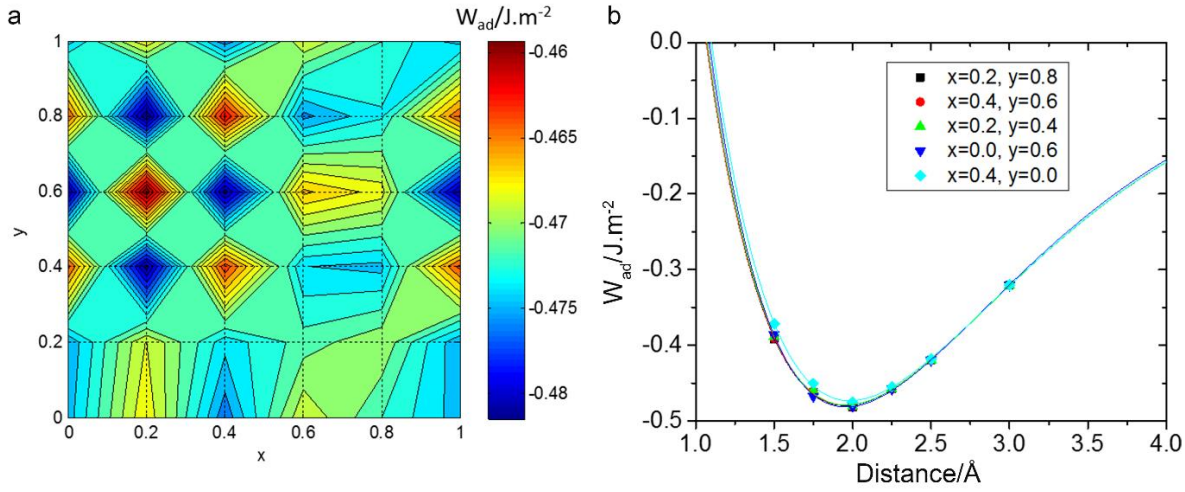

Figure 5.1. Optimization of the translation state within the interfacial plane and the interfacial distance for the Li-LLZO interface: a) contour plot of W_{ad} as a function of translation state for the Li slab relative to the LLZO slab using a 5×5 grid with a constant interfacial distance of 2 Å. b) W_{ad} as a function of interfacial distance between slabs fitted by the UBER for the five lowest W_{ad} interfaces identified in the contour plot of panel (a).

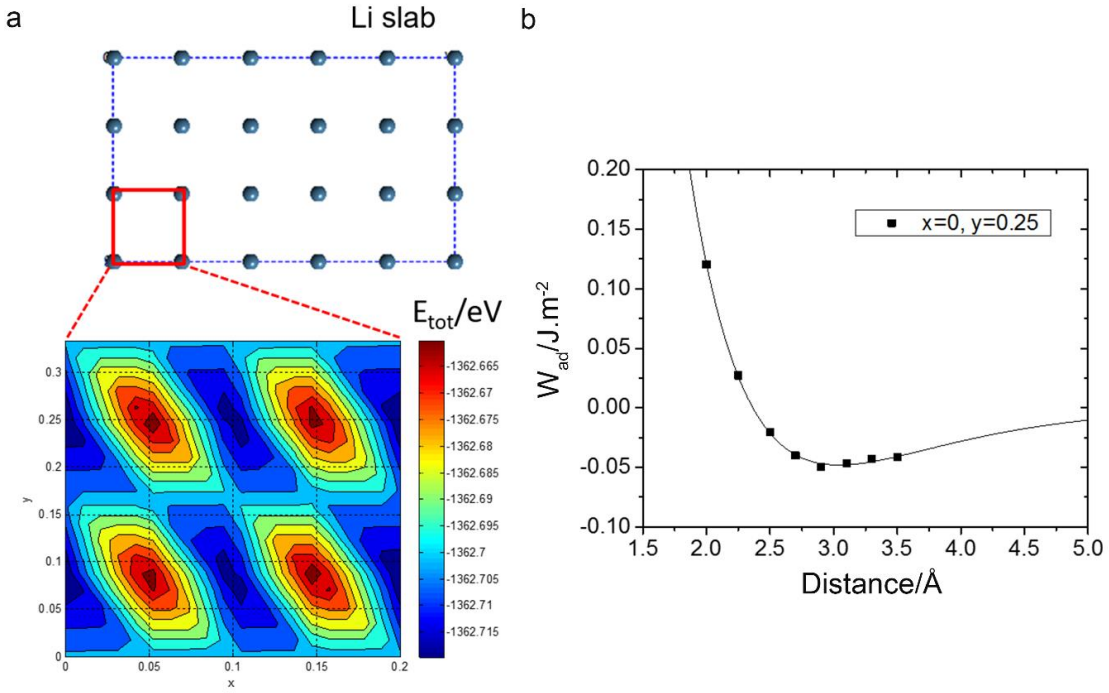

Figure 5.2. Optimization of the translation state within the interfacial plane and the interfacial distance for the Li-Li_2CO_3 interface. a) contour plot of the total energy as a function of translation state for the Li slab relative to Li_2CO_3 slab with a constant interfacial distance of 3 Å. Due to the symmetry of Li atoms in the Li slab, the translation state was restricted to the red box using a 4x4 grid. b) W_{ad} as a function of interfacial distance fit to the UBER for the lowest total energy interface (translation Li slab to x=0 and y=0.25) identified in panel (a).

5.2.5 Electrochemical measurements

Electrochemical measurements were performed to determine the effect of HT on RLi-LLZO and the maximum critical current density (CCD). Metallic Li electrodes were prepared by scraping with a stainless-steel spatula to expose a clean surface. Li-LLZO-Li cells were compressed under a constant 350 kPa uniaxial pressure during cycling. EIS measurements were conducted on symmetric cells after assembly using a 100 mV amplitude in the frequency range of 7 MHz to 1 Hz using a VMP-300 biologic and EC-Lab V11.02 software. To ensure good contact between metallic Li and LLZO, cells were heated to 175°C for 12 h as has been reported by Sharafi *et al.* (preconditioning step).[115] After cooling to room temperature, the change in cell impedance with a focus on RLi-LLZO was measured by EIS again. First, the entire spectrum was normalized for the contact area between Li and LLZO (area = 1.26 cm^2). Then, an equivalent circuit model was used to interpret the data. The EIS data was modeled using the equivalent circuit model shown in Figure 7b. An equivalent circuit model was used to interpret the data. In this model, a combination of a resistor and a capacitor in parallel are used to represent each transport phenomenon in the cell. Thus, three parallel combinations were used in the model representing the bulk (R_{bulk}), the grain boundary (R_{gb}), and the Li-LLZO interface ($R_{Li\text{-}LLZO}$). Ideal capacitors were replaced with constant phase elements (CPE) to account for any non-ideal behavior and dispersion in the time constant. The ideality of The CPE is represented by the coefficient α (α=1 shows the component is behaving as an ideal capacitor).[72] The Q values for the CPE should be on the order of 10^{-12}, 10^{-8}, 10^{-6} F for bulk, grain boundary, and Li-LLZO interface, respectively.[21, 72]

Cycling behavior of Li-LLZO-Li symmetric cells was measured at room temperature between 0.01 to 1 $mA.cm^{-2}$ to determine the CCD (the current density at which the cell

voltage dropped to 0 V). Cycling was continued until evidence of short-circuiting was observed and marked by a sudden drop in polarization voltage. To examine the cycling behavior of LLZO, Li-LLZO-Li cells were galvanostatically cycled at ± 0.2 $mA.cm^{-2}$. During cell cycling, the cell impedance was measured every 20 cycles, to evaluate the impact of electrochemical cycling on cell impedance and its stability. In this study, all tests have been repeated three times to ensure reproducibility.

5.3 Results and discussion

5.3.1 Surface chemical analysis

As has previously been shown, the surface chemistry of LLZO is sensitive to air exposure.[91, 96] A contamination layer readily forms and is predominantly composed of lithium carbonate (Li_2CO_3), lithium hydroxide (LiOH), and other adventitious carbon species;[91, 96, 127] which collectively result in high interfacial resistance between LLZO and metallic Li.[91, 127] It has been reported that dry polishing in an inert atmosphere can lower the interfacial resistance by partially cleaning the surface; however, the efficacy of this approach is limited to reducing the interface resistance from ~1000 $\Omega.cm^2$ to ~100 $\Omega.cm^2$.[91, 127] Here, several surface conditioning protocols, including dry polishing (DP), wet polishing (WP), and heat treatments (HT) were employed in an attempt to reduce the interfacial resistance, and their impact on LLZO surface chemistry was evaluated. Heat treatment between 200 and 500°C in an inert atmosphere was conducted after dry and wet polishing.

The surface chemistry of LLZO was analyzed using X-ray photoelectron spectroscopy (XPS) after each conditioning protocol (Figure 5.3). Measurements were performed on samples transferred without air exposure between an argon-filled glovebox

and the ultra-high vacuum XPS chamber. Figure 1a shows that in samples conditioned with DP or WP (no HT) a surface layer blocks nearly all the signal attributed to La and Zr. Thus, in these cases the surface layer is composed almost entirely of H, Li, C, and O (H content cannot be directly detected by XPS, but can be observed as hydroxyl bonds). The nature of the bonds in which these species participate can be examined through high-resolution core-scans. The O 1s peak reveals a significant difference between the surface layer after wet vs. dry polishing (Figure 5.3b). The WP surface consists of predominantly hydroxide species, while a greater concentration of carbonate species exists on the DP sample. This suggests that the use of polishing fluid protects the LLZO surface from reformation of carbonate species.

Samples that underwent HT were first polished (DP or WP in ambient air) and then immediately transferred into an argon-filled glovebox where the samples were heated to different temperatures. Subsequent XPS analysis demonstrated significant variations in the surface chemistry of these samples. In Figure 5.3a the plot of the ratio of the C content to the summed La and Zr contents is used as a metric to quantify the amount of surface contamination. The lower the ratio, the more closely the surface resembles bulk LLZO. Some adventitious carbon is always observed on the LLZO surface, even for samples kept continuously in an argon atmosphere after HT, Figure 5.3c. The amount of contamination is observed to dramatically decrease after heating to 400 and 500°C. This is consistent with the O 1s core scans shown for these samples, which demonstrate that the predominantly hydroxide and carbonate surfaces before heating are converted to primarily oxide species (as expected in bulk LLZO) after heating (Figure 5.3b). In contrast, heating a DP sample to 400°C did not change the surface as dramatically, with

carbonate species still dominating (Figure 4). A plot of the fractional surface composition of the oxygen-containing species is shown in Figure 3d for WP samples heated to different temperatures. As the HT temperature increases to 500°C, the oxide fraction steadily increases, the hydroxide fraction decreases, and the amount of carbonate remains roughly constant. In total, these observations suggest that: (1) compared to dry polishing, wet polishing is more effective at achieving a surface with low carbonate content, (2) heat treatment up to 500°C can remove LiOH, but is less effective at removing Li_2CO_3, and (3) of the strategies examined, the successive combination of WP and HT is the most effective at removing both carbonate and hydroxide surface contamination layers.

The removal of LiOH species at temperatures between 400 and 500°C is consistent with prior thermogravimetric analysis, mass spectroscopy, and first-principles calculations.[127-128] This suggests that the surface layer that reforms as a result of wet polishing is more easily removed by HT, thereby making the combination of wet polishing and HT in an inert atmosphere an attractive option to achieve a well-controlled LLZO surface prior to forming the Li-LLZO interface.

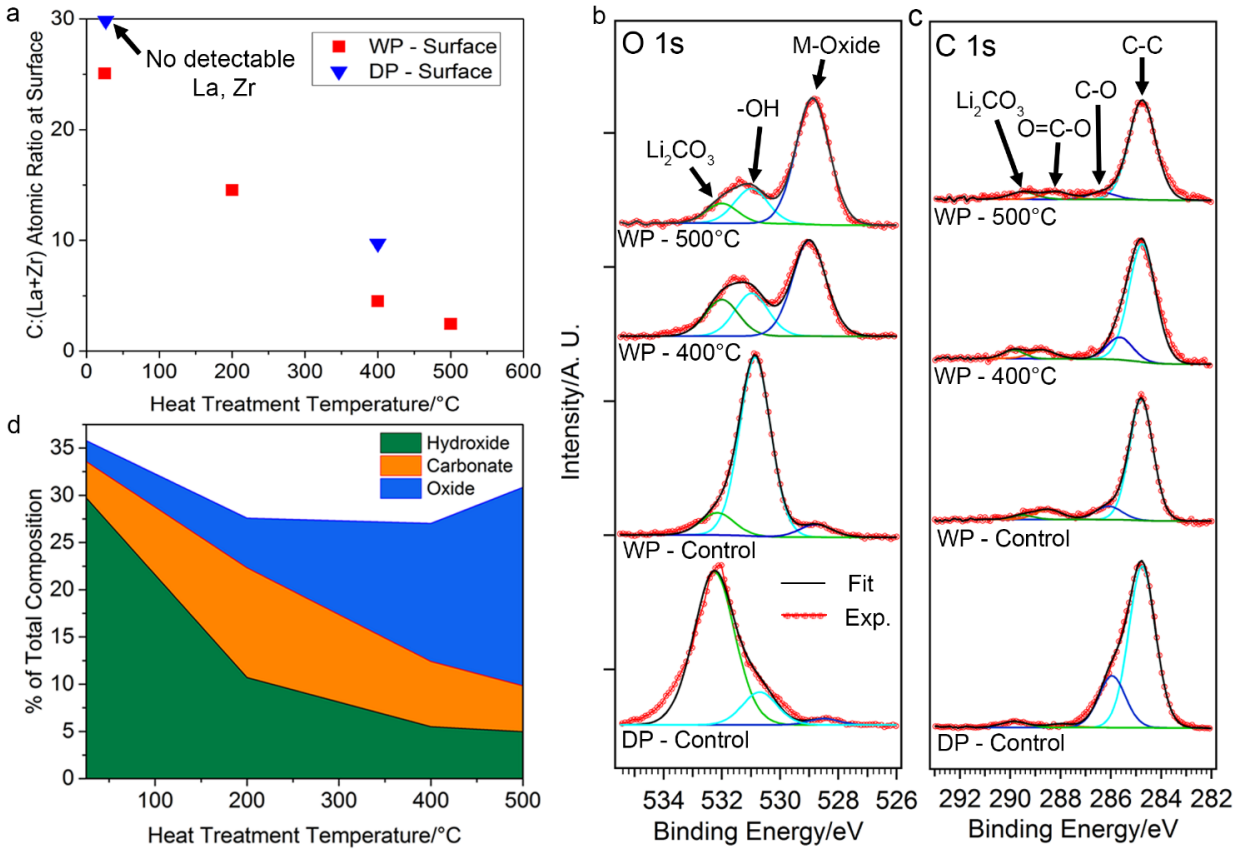

Figure 5.3. XPS analysis of LLZO before and after heat treatment at 400 and 500°C. a) C:(La+Zr) atomic ratio as a function of heat treatment temperature, b) O 1s and c) C 1s core levels, d) percentage of total composition of different oxygen species on LLZO surface as a function of heat treatment temperature after WP.

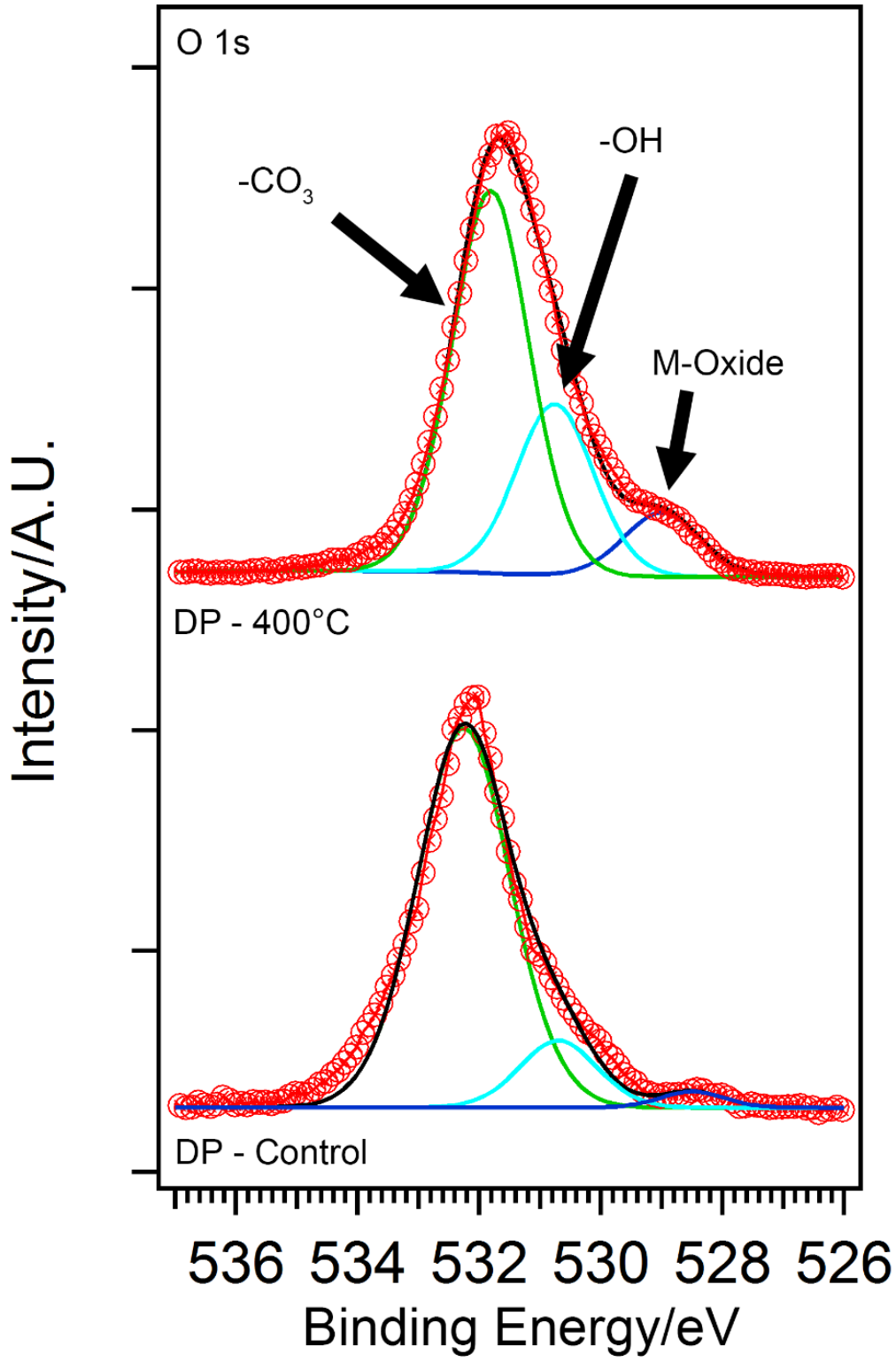

Figure 5.4. XPS analysis of LLZO showing the O 1s core level after dry polishing (DP-Control) and after dry polishing and heat treatment at 400℃ (DP-400℃).

5.3.2 Contact angle measurements and calculations

The wettability of a SSE by Li metal has been proposed to influence interfacial resistance in SSBs. However, quantitative analysis of the Li contact angle and direct correlation with surface chemistry has not been reported. To characterize wettability, sessile drop tests were performed to measure the contact angle of molten Li on Li_2CO_3 and on LLZO samples after various surface conditioning processes (Figure 5.5). Molten Li was deposited onto heated Li_2CO_3 or LLZO from a heated stainless-steel syringe. Both the surfaces and the syringe were kept above the Li melting temperature. Importantly, the native layers (composed of oxide, nitride, and carbonate species)[129] present on the surface of the Li foil did not melt, and thus were easily removed from the molten Li source. This allowed for deposition of purified molten Li onto the LLZO surface. The present approach differs from a scenario involving the melting of solid Li foil directly on LLZO, as wettability in the latter approach will be influenced by the presence of native layers on the Li surface and at the Li-LLZO interface. All experiments were performed inside an argon-filled glovebox, and high-resolution cross-sectional images were captured and digitally analyzed to determine contact angles.

As shown in Figure 5.5, the DP-LLZO sample exhibited the highest contact angle amongst all LLZO samples, $\theta = 146°$, which was nearly identical to the value measured for a pure Li_2CO_3 surface ($\theta = 142°$). Such a large contact angle is consistent with a non-wetting interaction typical of an interface exhibiting weak adhesion. The similar wetting behavior between the DP-LLZO sample and Li_2CO_3 is expected, given that the DP-LLZO surface is composed predominantly of Li_2CO_3. Similarly, the WP-LLZO contact angle was 141°, which is consistent with the presence of the hydroxide and

carbonate contamination layer which was observed with XPS. In contrast, the WP-LLZO heat treated at 500°C, exhibited a significantly lower contact angle ($\theta = 95°$). We hypothesize that this reduction in contact angle is caused by the removal of hydroxide and carbonate species, resulting in a surface more closely resembling bulk LLZO, which interacts more strongly with Li metal.

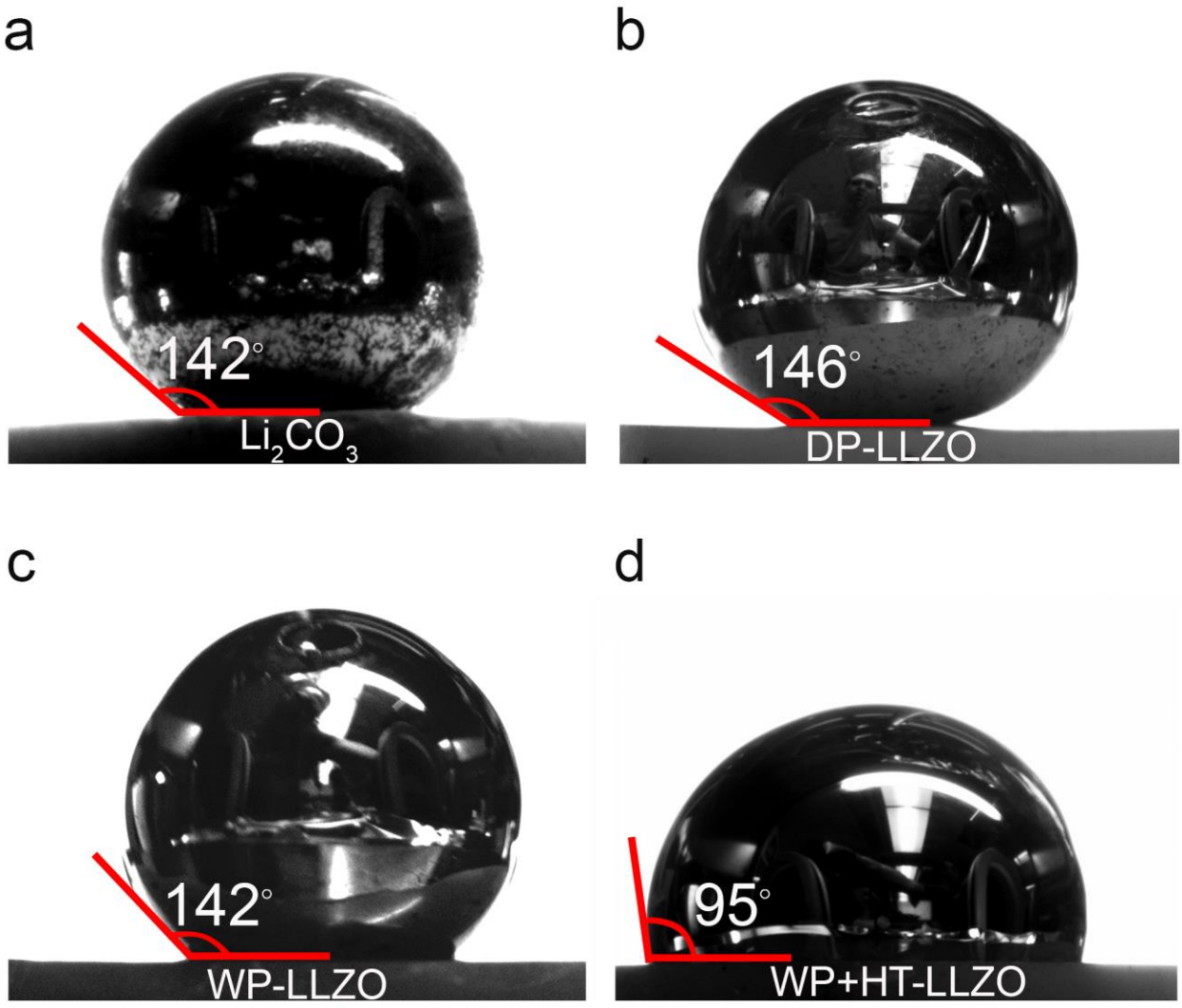

Figure 5.5. Contact angle measurements of molten metallic Li on a) Li_2CO_3, b) DP-LLZO, c) WP-LLZO, d) WP-LLZO after heat treatment at 500°C.

To validate the correlation between surface chemistry and wettability, the wetting angle of Li on LLZO, Li_2CO_3, and LiOH was evaluated using DFT calculations.[99] Li-LLZO, Li-Li_2CO_3 and Li-LiOH interfaces were constructed from the low-energy surfaces of each respective material, as reported previously.[51, 130] Large simulation cells were used, to accommodate geometries that minimize interfacial strain. The interfacial distance and translation state within the interfacial plane were optimized to identify the most energetically-favorable interface structures.

Figure 5.6 shows the atomic structure of the low-energy interfaces for Li-LLZO and Li-Li_2CO_3 (Data for Li-LiOH are shown in Table 5.2). The contact angle, θ, for these interfaces was calculated by combining the Young-Dupré equation, $W_{ad} = \sigma_{Li}\,(1+\cos\theta)$, with DFT calculations of the interfacial work of adhesion, W_{ad}, and the surface energy of Li, σ_{Li} = 0.45 J.m^{-2}. Using the Li-LLZO interface as an example, W_{ad} was evaluated as: $W_{ad} = E_{int} - E_{Li\text{-}slab} - E_{LLZO\text{-}slab}$. Here E_{int} is the energy of the interface cell and $E_{X\text{-}slab}$ refers to the energy of an isolated Li (X = Li) or LLZO slab (X = LLZO). The calculated values for W_{ad} and θ are shown in Figure 5.6 below their respective interfaces. The trend predicted by our calculations – that Li strongly wets LLZO, but not Li_2CO_3 – is consistent with the measurements shown in Figure 5.5. More specifically, the wetting angle predicted for the Li-Li_2CO_3 interface, θ=142°, is in excellent agreement with the measured value (142°, Figure 5.5a) indicating a weak interfacial interaction between Li and Li_2CO_3 (W_{ad} = 0.10 J.m^{-2}). In contrast, the calculated Wad for the Li-LLZO interface is nearly seven times larger, W_{ad} = 0.67 J.m^{-2}, resulting in a relatively small wetting angle, θ = 62°. This value is qualitatively consistent with the measured value of 95° reported in Figure 5.5d. The smaller value predicted by our calculations is expected, given that approximately 15% of carbonate and/or hydroxide remains on the LLZO surface after heating to 500°C (Figure 5.5d).

Calculations on the Li-LiOH interface predict a relatively large contact angle of 125°, similar to the non-wetting behavior observed for the Li-Li_2CO_3 system (see Table 5.2).

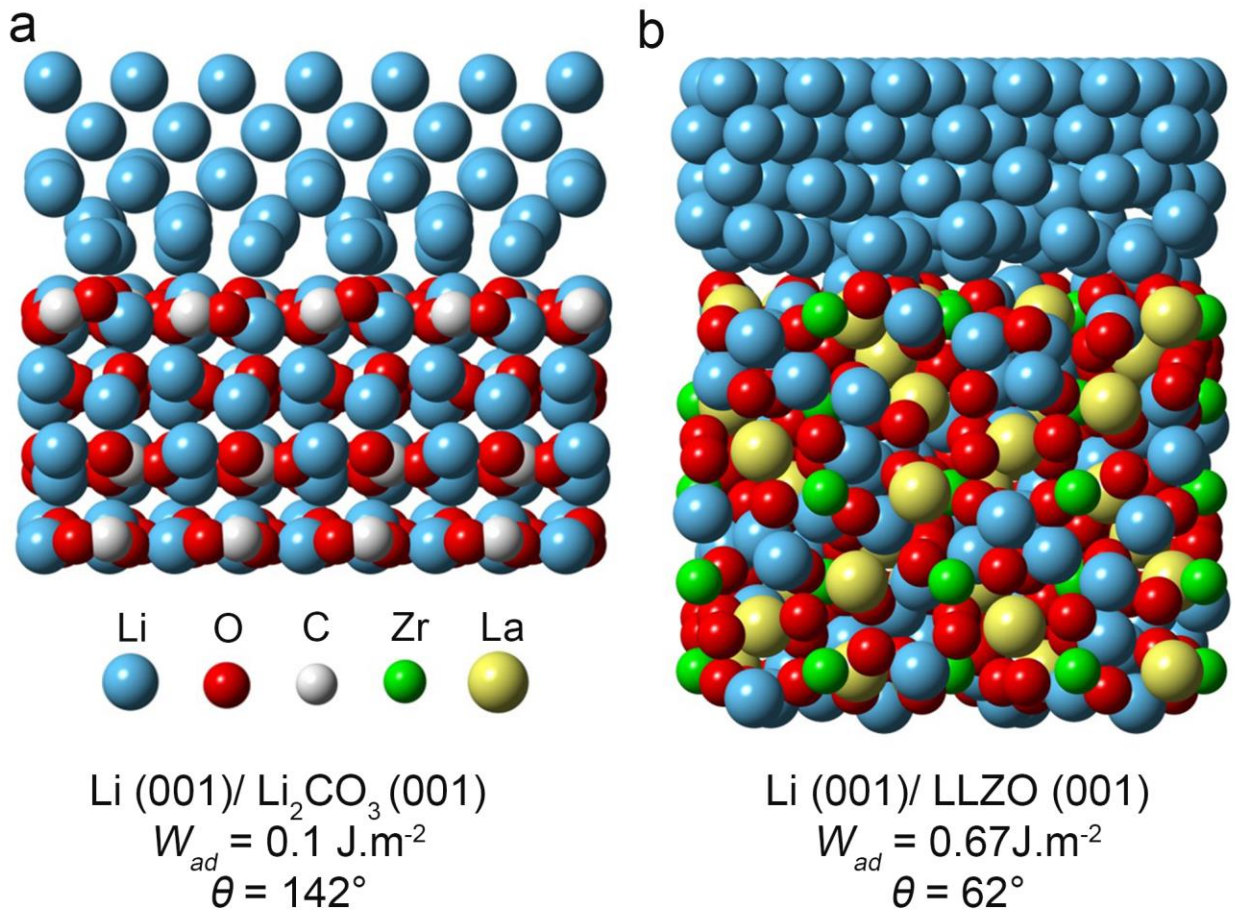

Figure 5.6. Calculated work of adhesion (W_{ad}), contact angle (θ), and atomic structure for the a) Li-Li_2CO_3 and b) Li-LLZO interfaces.

5.3.3 Electrochemical measurements

Electrochemical impedance spectroscopy (EIS) was performed on Li-LLZO-Li symmetric cells (Figure 5.7a) to measure the LLZO bulk (R_{bulk}), grain boundary (R_{gb}), and Li-LLZO interfacial ($R_{Li\text{-}LLZO}$) resistances for WP and HT samples between 200 and 500°C. In this study, EIS data were modeled using an equivalent circuit shown in Figure 5.7b. This approach allows for the direct measurement of the individual contributions to cell resistance and involves the correlation between characteristic frequencies and

transport phenomena.[73] Representative EIS spectra for a cell consisting of a WP and HT at 500°C LLZO sample before and after preconditioning at 175ºC are shown in Figure 5.7c (Preconditioning was used to ensure good contact between metallic Li and LLZO by heating the Li-LLZO-Li cell to 175°C for 12 h).[115] From Figure 5.7c, it is apparent the LLZO total resistance (R_{bulk} + R_{gb}) has remained constant (500 Ω.cm^2) while $R_{Li\text{-}LLZO}$ dramatically decreased upon preconditioning at 175°C and cooling. Initially, $R_{Li\text{-}LLZO}$ was approximately 400 Ω.cm^2 which is significantly lower than previous values reported for LLZO after dry polishing in literature.[115] After preconditioning at 175ºC, a further dramatic reduction in $R_{Li\text{-}LLZO}$ was observed. The combination of wet polishing, HT, and preconditioning results in an extremely small interfacial resistance of 2 Ω.cm^2.

Figure 5.7d shows $R_{Li\text{-}LLZO}$ after preconditioning for WP LLZO samples with no HT and HT at several temperatures between 200 and 500ºC. With increasing HT temperature, $R_{Li\text{-}LLZO}$ decreases from 400 to 2 Ω.cm^2. Importantly, the low interfacial resistance coincides with the removal of the surface contamination layer. Furthermore, the decrease in interfacial resistance closely follows the trend in surface chemistry with HT temperature observed in XPS measurements, and with the improved wettability of the LLZO surface after HT. Taken together, these observations provide quantitative evidence of the strong coupling between surface chemistry, wettability, and interfacial resistance.

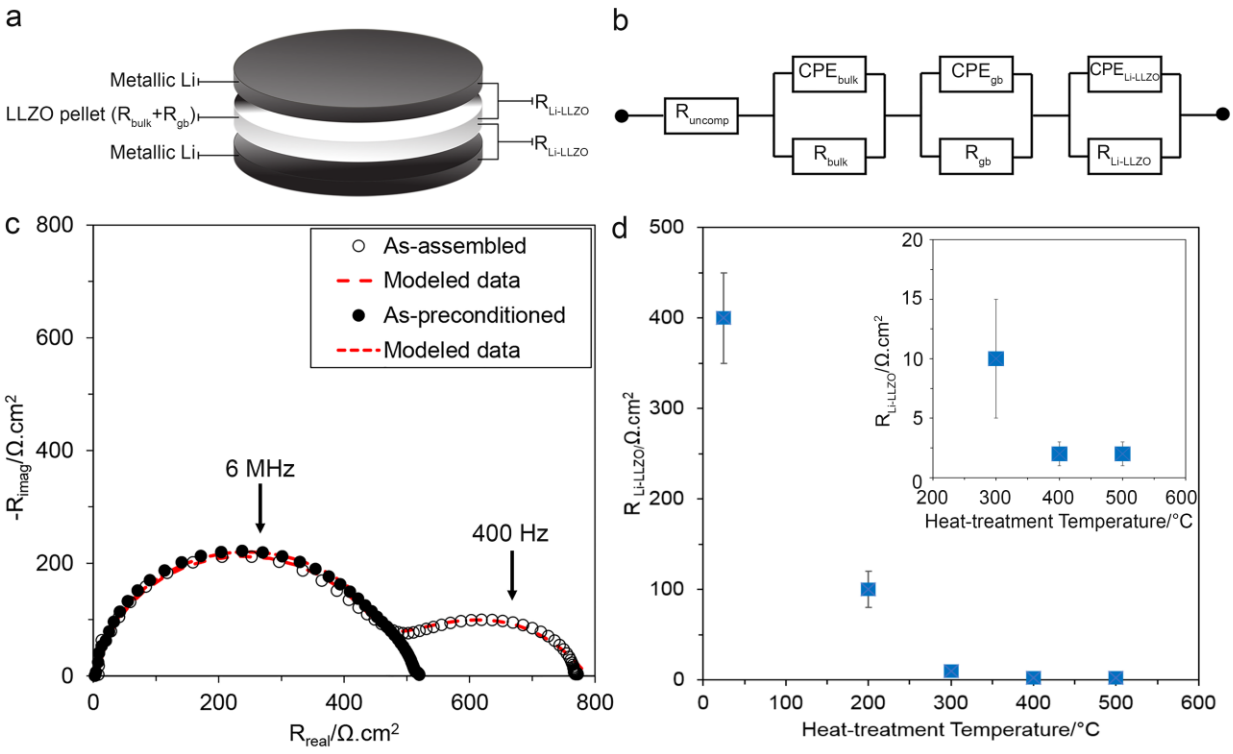

Figure 5.7. a) Schematic diagram of an solid-state Li-LLZO-Li cell, b) the equivalent circuit used for modelling the EIS data c) representative Nyquist plot of the Li-LLZO-Li cell (for LLZO heat-treated at 500°C), as-assembled (○) and after preconditioning at 175°C (●). Markers indicate experimental data and dotted lines are simulated lines extrapolated from equivalent circuit modelling using the circuit shown in b, d) the Li-LLZO interfacial resistance after preconditioning at 175°C versus the heat-treatment temperature. N=3 for each HT condition. Error bars represent standard deviations.

The cycling behavior and critical current density (CCD) of a WP LLZO sample HT to 500°C (WP+HT) were characterized using a combination of DC cycling and EIS analysis (Figure 5.8). The CCD is defined as the lowest current density at which cell shorting occurs due to Li metal penetration.[115, 127] After removal of the surface contamination, the CCD was determined to be 0.3 mA.cm^{-2} (Figure 5.8a). The CCD from the WP+HT sample prepared here is compared in Figure 5.8b to other Li-LLZO-Li symmetric cells reported in the literature.[57, 91, 115] The CCD measured in this study is one the highest values reported in literature for an LLZO SSE. Our data indicates that the CCD and R_{Li-}

$_{LLZO}$ are inversely correlated, suggesting that higher power density can be achieved by controlling interfacial chemistry, and thus $R_{Li\text{-}LLZO}$.

To evaluate the stability of the interface after WP+HT upon cycling, a Li-LLZO-Li cell was cycled for one hundred cycles at ± 0.2 mA.cm^{-2} at room temperature (Figure 5.8d). After every 20 cycles, EIS analysis was conducted to assess changes in R_{bulk}, R_{gb}, and $R_{Li\text{-}LLZO}$. Figure 5.8c shows that negligible changes in the EIS spectra were observed, implying excellent stability of the interface and the absence of short-circuiting. Furthermore, the total cell resistance (R_{bulk} + R_{gb}+ $R_{Li\text{-}LLZO}$) estimated using the DC cell polarization voltage (230 Ω.cm^2) (Figure 5.8a) agrees well with the total cell resistance measured using EIS (240 Ω.cm^2). This confirms that the DC and EIS analyses are in good agreement, and further validates the interpretation of the EIS data to quantitatively decouple resistance values and correlate them to their respective transport phenomena.

The DC and EIS characterization illustrate the importance of achieving low and stable interfacial resistance. First, a low $R_{Li\text{-}LLZO}$ enables a path toward low resistance solid-state cell designs employing metallic Li anodes. Second, reducing $R_{Li\text{-}LLZO}$ increases the CCD. Although 0.3 mA.cm^{-2} is one of the highest reported CCD values, it must be further increased to demonstrate relevance to vehicle electrification; the data in Figure 5.8b, suggest further tuning surface chemistry and reducing $R_{Li\text{-}LLZO}$ may be an approach to achieve higher CCD. Lastly, a clean and discrete Li- LLZO interface is preferred to minimize side reactions and mechanical degradation. In preliminary cycling tests, the interface kinetics appear to be stable when cycling at ± 0.2 mA.cm^{-2} at room temperature. Altogether, the electrochemical characterization suggests WP+HT could enable the use of metallic Li anodes and LLZO in SSBs.

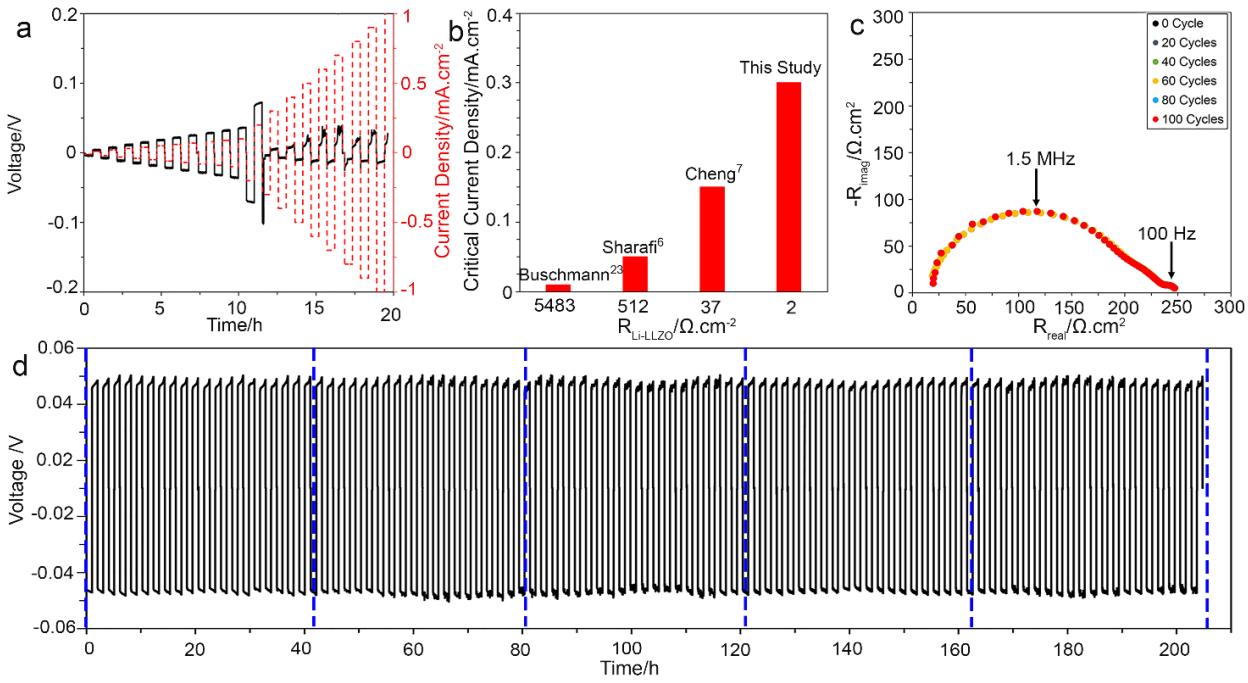

Figure 5.8. a) DC cycling of Li-LLZO-Li cells (LLZO HT to 500°C after WP) at room temperature, stepping the current density from 0.01 to 1 mA.cm^{-2}, b) the critical current density versus Li-LLZO interfacial resistance comparing the result of this study with other studies available in the literature, c) Nyquist plots of Li-LLZO-Li cell after each 20 cycles for cell cycled 100 times, d) Galvanostatic cycling of Li-LLZO-Li at 0.2 mA.cm^{-2} for 100 cycles at 0.4 mAh.cm^{-2}. Blue dotted lines indicate the time at which EIS was conducted and shown in c.

5.4 Conclusions

This study demonstrates that by rational control of surface chemistry, low Li-LLZO interfacial resistance (2 Ω.cm^{-2}) comparable to Li-ion technology can be achieved without the need for coatings. The removal of LLZO surface contamination (as confirmed by XPS) was demonstrated to be an effective method to enhance Li wetting of LLZO, which was quantitatively evaluated using molten Li contact angle measurements through sessile drop tests. The interfacial chemistry and wettability measurements agree with DFT calculations of interfacial energy. The effect of coupled surface chemistry and wettability were quantitatively correlated with the Li-LLZO interfacial resistance (Figure 5.9). Improved interfacial resistance also resulted in an increase in CCD to 0.3 mA.cm^{-2}. EIS analysis and DC cycling at ± 0.2 mA.cm^{-2} up to one hundred cycles in Li-LLZO-Li cells

demonstrated that the low interfacial resistance was preserved with no sign of short circuiting. This study improves the understanding of relationships between interfacial chemistry, lithium wettability, interfacial resistance, and stable cycling, which has implications for a wide range of SSBs and enables rational design of interfaces.

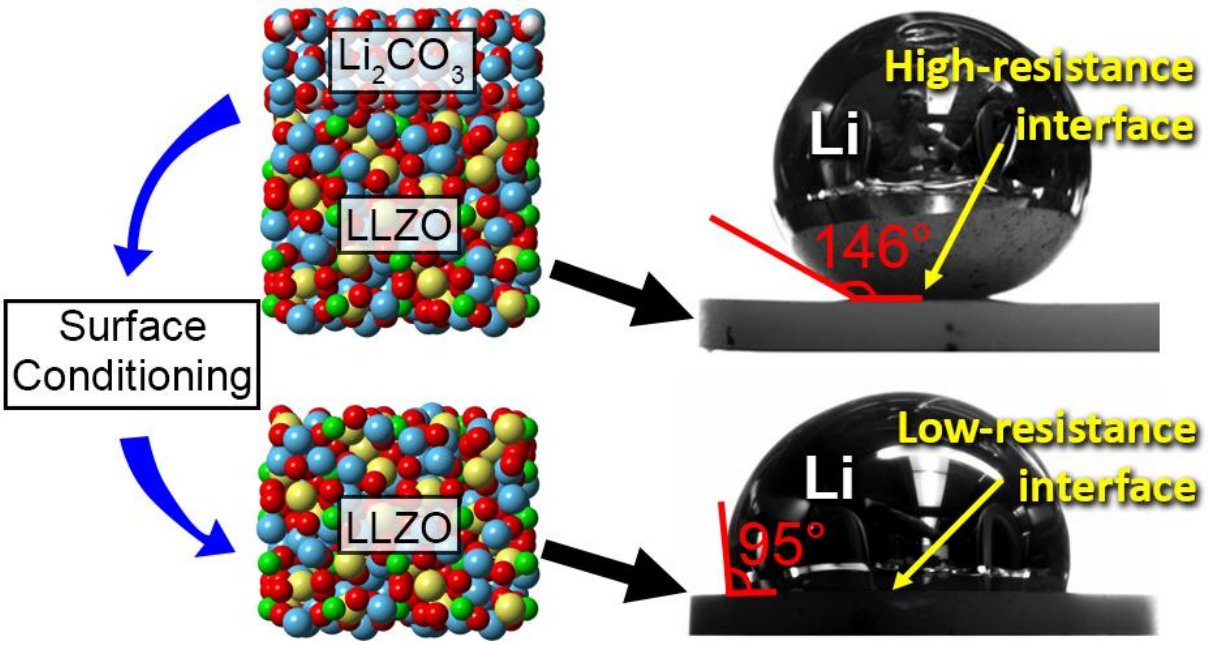

Figure 5.9. The strong linkages between surface chemistry, lithium wettability, and facile charge transfer are quantitatively demonstrated.

CHAPTER VI

Correlating the effect of grain size with the stability of the metallic Li - polycrystalline $Li_7La_3Zr_2O_{12}$ solid-state interface

6.1 Introduction

Li-ion battery (LIB) is a promising technology to meet near-term vehicle electrification needs, however achieving wide-scale adoption of electric vehicles will require a step increase in energy density (>1000 $Wh.l^{-1}$).[8, 11, 131] It is known that dramatically increasing energy density is possible by replacing conventional state-of-the-art anodes with metallic Li; but, stabilizing the Li-electrolyte interface has been a difficult challenge to overcome.[45-46, 132-133] Thus, there is a great-unmet need for strategies to stabilize the metallic Li interface during cycling, especially at high plating rates. One approach involves the integration of solid-state electrolytes (SSE) with metallic Li. The garnet-type SSE, with the nominal formula $Li_7La_3Zr_2O_{12}$ (LLZO) is promising, because it simultaneously satisfies several key performance criteria such as chemical and electrochemical stability against metallic Li and high ionic conductivity (1 $mS.cm^{-1}$ at room temperature).[51, 116, 134] Despite satisfying these and other performance characteristics, numerous barriers remain. We believe that the maximum Li plating rate is one of the primary challenges preventing the maturation of LLZO membrane technology. We and others have observed that Li metal propagates into LLZO at or above current densities ranging from 0.05 to 0.2 $mA.cm^{-2}$.[59-60,

[62, 74, 115, 127, 135] Although perhaps not directly related to crystalline materials, it has been suggested that the SSE shear modulus and the fracture toughness are important factors that affect the onset and propagation of alkali metals through SSE, respectively.[52, 81, 85] Furthermore, in a recent study by E. J. Cheng *et al*. it was determined that Li metal propagates along grain boundaries in polycrystalline LLZO when the critical current density (CCD) is exceeded, (CCD is defined as the current density at and above which Li metal propagates through a SSE).[127] Thus, it was hypothesized that one strategy to increase the CCD is to reduce the area fraction of grain boundaries or by increasing the grain size.[127] While there are several hypotheses that could help elucidate the phenomena that govern the CCD, to date, none have been validated for solid-state alkali metal-SSE interfaces or more specifically the Li-LLZO interface. It follows that the purpose of this study was multifold. One goal was to understand grain growth kinetics to allow for the fabrication of LLZO with a wide grain size range. Another goal was to correlate the effects of grain size with the mechanical, and electrochemical properties such as the CCD. Lastly, the overarching goal of this work was to better understand the underpinning mechanisms that govern the stability of the Li-LLZO interface.

A concerted suite of aspects was studied comprising ceramic processing, materials characterization, mechanical property measurements, and electrochemical analyses. Polycrystalline LLZO was densified using hot-pressing and annealing. Based on the processing conditions, the average LLZO grain size ranged between 5 to 600 μm. LLZO microstructures were characterized using standard materials characterization techniques as well as electron backscatter diffraction (EBSD) to obtain grain size, grain orientation, and grain boundary misorientation angle statistics. EBSD was used to analyze the grain growth mechanism and grain growth rate as a function of processing conditions. Vickers indentation was used to determine

hardness and fracture toughness as a function of grain size. Lastly, direct current (DC) and electrochemical impedance spectroscopy (EIS) were used to evaluate the CCD as a function of grain size. Taken together, these data were used to correlate the effects of LLZO grain size and mechanical properties on controlling the CCD.

6.2 Experimental

6.2.1 Powder synthesis and pellet processing of solid-state electrolyte

Cubic Al-doped LLZO with nominal composition of $Li_{6.25}Al_{0.25}La_3Zr_2O_{12}$ was prepared using solid-state synthetic technique. This composition was chosen due to its high ionic conductivity and stability against metallic Li.[50-51, 71, 114, 116] Li_2CO_3 (99.0%, Alfa Aesar), $La(OH)_3$ (99.95%, Alfa Aesar), ZrO_2 (99.9%, Inframat Advanced Materials), and Al_2O_3 (99.9%, Mager Scientific) precursors were combined in stoichiometric quantities and dry-milled for 4 h at 350 rpm in a planetary ball mill (Retsch GmbH). 5 wt. % excess Li_2CO_3 precursor was used to compensate for Li loss during calcination. The resulting mixed powder was pressed into pellets with diameter of 25.4 mm using a stainless-steel die (MTI Corporation) at 10 MPa. The cold-pressed pellets were placed on a MgO boat (Ozark Technical Ceramics) and calcined at 1000°C for 4 h in a tube furnace (STF 15/180, Carbolite LTD) under flowing dry air (Cryogenic gases, < 3 ppm moisture). The calcined pellets were ground into powder using a mortar and pestle and passed through a 75 μm sieve.

For hot-pressing, 6 g of powder was cold-pressed into a pellet with 12.7 mm diameter using a stainless-steel die at 62 MPa. The green density of the pellet was measured by dividing the mass by the measured volume (geometrical density). The relative density (RD%) was defined as the ratio of the geometric density and the theoretical density (5.17 $g.cm^{-3}$) with relative densities of green pellets ranging from 52 to 55%. The green pellet was placed in a graphite die then hot-

pressed using a custom rapid induction hot-pressing (RIHP) technique at a uniaxial 62 MPa pressure for 1 h under a flowing argon atmosphere. The microstructural evolution and grain growth was controlled by changing the hot-pressing temperature: 1100°C, 1200°C, 1250°C, and 1300°C. We will refer to these samples as HP-1100°C, HP-1200°C, HP-1250°C, HP-1300°C. Increasing hot-pressing temperature >1300°C resulted in significant Li loss, thus the maximum hot-pressing temperature was 1300°C. After hot-pressing, specimens were cut into pellets (1.1 ± 0.2 mm thickness) using a diamond saw (11-2180, Buehler). An alternative approach with a combination of hot-pressing and annealing was used to further grow grains. For this approach, HP-1100°C pellets were embedded in LLZO mother powder in a MgO boat and annealed in a tube furnace under flowing argon for 50 h at 1300°C (A-1300°C). The heating and cooling rate was 4°C.min^{-1}.

The pellets were ground by mechanical grinding using 400 grit sandpaper (Norton Corporation) and a polishing fixture (Model 150, South Bay Technology) to achieve parallel faces. Next, the pellets were ground using 600 grit and 1200 grit sandpaper followed by polishing (AutoMet 250, Buehler) using 15 μm, 6 μm, 1 μm, and 0.5 μm diamond polishing compound (LECO Corporation) with glycol based diamond extender (LECO Corporation). For all steps, 10 N force was applied to each pellet during polishing and the head and base rotated at 210 rpm and 60 rpm, respectively. For all mechanical property and electrochemical characterization, the final polishing step was 0.5 μm. For electron backscatter diffraction (EBSD) analysis, additional polishing was done using a colloidal silica suspension (Mager Scientific) with 0.03 μm particle size for 1 h, then washed with deionized water to remove the silica from the surface. The final polishing step was done immediately before EBSD analysis to minimize surface contamination and ensure that high quality electron backscatter patterns are obtained.

6.2.2 Materials characterization

6.2.2.1 X-ray diffraction

XRD (MiniFlex 600, Rigaku) was used to characterize the crystalline phases present in the LLZO powder, and LLZO pellets after hot-pressing and annealing. Samples were spun during XRD to ensure diffraction from multiple grains, especially for pellets with larger (>40 μm) grain size. Spectra were collected from 15 to 65° 2θ, at a rate of $4.5°.min^{-1}$ in 0.02° increments using CuK_{α} radiation operating at 40 kV and 15 mA. Rietveld refinement and Jade software 2010 (Version 5.0.0, Materials Data Inc.) was used to determine and quantify the weight fraction of phases present. The following reference crystallographic information files were used: cubic LLZO (PDF# 04-018-3158), $La_2Zr_2O_7$ (PDF# 01-070-5602), and $La_{0.28}Zr_{0.72}O_{1.86}$ (PDF# 04-002-7939).

2.2.2 Scanning electron microscopy (SEM) and Electron backscatter diffraction (EBSD)

SEM was performed on polished surfaces of LLZO pellets using a FEI Nova 200 lab dualbeam at 10 kV accelerating voltage and 5 mm working distance. EBSD measurements were conducted using an EDAX detector and TEAM software on a Tescan MIRA3 SEM. The microscope was operated at an accelerating voltage of 30 kV, and working distance of 20 mm. For EBSD analysis, the pellets were tilted at 70° toward the EBSD detector. A step size of 5 μm was used to construct EBSD maps. The backscatter diffraction patterns were fit to a custom material profile using information from PDF# 04-018-3158. The collected data were analyzed using EDAX OIM data collection software. The datasets were refined by dilating the grains in a single iteration. Grain dilation is an iterative OIM data-cleaning method, which assigns an orientation to a point that does not belong to any grains. Using this method, the orientations of neighboring points are

obtained and the orientation of a cleaning point is assigned to the orientation of most neighboring points.

6.2.2.3 Mechanical properties

The Vickers hardness (H) of hot-pressed and annealed pellets was measured using a Vickers hardness tester (HM122V/K Series 810 Micro, Mitutoyo Corporation). Before indentation, the indenter was calibrated using a steel hardness block (Hardness Test Block HMV 700 HV, Mitutoyo Corporation). The Vickers hardness tests were conducted at a load of 0.098 N for an indentation time of 10 s. The load was chosen specifically for each sample to reduce microcracking. The average hardness for each specimen was determined by using ten indentations. No indentations were placed closer than 1000 μm from the pellet edge, and a separation distance of at least 150 μm was maintained between adjacent indentations. The H values were determined by Equation (1):[136]

$$H = \frac{1.854P}{d^2} \quad (1)$$

where P is applied load, and d is the length of the diagonal of the Vickers indentation impression.

The fracture toughness (K_{IC}) of hot-pressed and annealed pellets was determined using the indentation technique on a Vickers indenter. The applied load was 0.196 N, chosen to produce measurable crack lengths with crack radius about 2-3 times larger than the half diagonal for all the measurements. In all cases, the dwell time was 10 s and ten indents were made per pellet. Crack lengths were determined using an optical microscope and confirmed by SEM (Nova 200 NanoLab, FEI) images right after indentations were made. The K_{IC} was calculated using Equation (2):[137]

$$K_{IC} = \xi\left(\frac{E}{H}\right)^{0.5}\frac{P}{c_0^{1.5}} \quad (2)$$

where ξ is a material-independent constant (0.016), E is the Young's modulus (150 GPa),[54] H is the hardness, c_0 is the crack length, and P is the applied load. The loads for H and K_{IC} measurements were kept constant for all pellets to eliminate the effect of load as a variable.

6.2.2.4 Electrochemical characterization

Electrochemical impedance spectroscopy (EIS) was performed on the hot-pressed and annealed LLZO pellets to determine the room temperature ionic conductivity. Gold electrodes were sputter coated on both sides of each pellet using a sputter coater (Desk V, Denton Vacuum) with gold target (99.99%, Angstrom Engineering). EIS was performed at 25°C from 1 Hz to 7 MHz with a 100 mV perturbation amplitude using a potentiostat/galvanostat (VMP300, Bio-Logic) and EC-Lab V10.44 software. The thickness and diameter of each pellet was used to normalize the collected data for conductivity calculations.

DC electrochemical measurements were performed to determine the maximum tolerable current density (critical current density, CCD). Prior to Li-LLZO-Li cells assembly, polished LLZO pellets were heat-treated in a muffle furnace (KSL-1100X, MTI Corporation) inside an argon-filled glovebox (0.1 ppm O_2 and 1 ppm H_2O) to reduce surface contamination that forms during air exposure. Pellets were placed on a MgO boat inside the furnace and heated to 400°C for 3 h using 4°C.min^{-1} as heating and cooling rate. Li foil (Alfa Aesar) was scraped with a stainless-steel spatula to remove the surface contamination layer before being used. Solid-state symmetric cells were assembled by placing the heat-treated LLZO pellet between two scraped Li foils. A load frame was used to apply a constant uniaxial pressure (3.5 MPa). EIS measurements were conducted on the assembled cell in the load frame. The cell was removed from the load frame and preconditioned by heating to 175°C for 12 h to improve contact between metallic Li and LLZO as demonstrated by Sharafi *et al.*[115] After cooling to room temperature, another EIS

spectrum was collected and normalized to the contact area between Li and LLZO (area = 1.26 cm^2). An equivalent circuit model was used to interpret the data and to determine the contribution of each resistive component in the total cell impedance. In this model, a combination of a resistor and a capacitor in parallel are used to represent each component in the cell. Thus, three parallel combinations were used in the model representing the bulk (R_{bulk}), the grain boundary (R_{gb}), and the Li-LLZO interfacial ($R_{Li\text{-}LLZO}$) resistance as shown schematically in Fig. 8a. Ideal capacitors were replaced with constant phase elements (CPE) to account for non-idealized behavior and dispersion in to the time constant. The ideality of the CPE is represented by the coefficient α (α = 1 shows the component is behaving as an ideal capacitors). The Q values for the CPE should be on the order of 10^{-12} F, 10^{-8} F, 10^{-6} F for bulk, grain boundary and Li-LLZO interface, respectively.[72-73] The data fitting and circuit modeling was done with a software package EC-Lab V10.44. To determine the effect of grain size on CCD, Li-LLZO-Li symmetric cells were cycled between 0.01 to 1 $mA.cm^{-2}$ at room temperature under a constant uniaxial pressure (3.5 MPa). Cycling was continued until a sudden drop in polarization voltage occurred, indicating short-circuiting of the cell. EIS was performed after DC cycling to confirm short-circuiting.

6.3. Results

6.3.1 Crystallographic and microstructural analysis of cubic $Li_7La_3Zr_2O_{12}$

6.3.1.1 Crystallographic analysis

XRD was used to characterize the LLZO powder and LLZO pellets hot-pressed between 1100 and 1300°C (Figure 6.1). The calcined powder, HP-1100°C and HP-1300°C pellets were single-phase cubic LLZO (space group $Ia\bar{3}d$). However, a low concentration of pyrochlore (<4 wt.%) was present in the HP-1200°C and HP-1250°C pellets. Previous reports indicated these

phases form due to Li loss during calcination and/or densification at high temperatures.[50, 123] The HP-1300°C did not contain secondary phases possibly due to the higher densification rate used compared to the HP-1200°C and HP-1250°C pellets. For example, it has been shown that as the densification rate increases, pore collapse accelerates, thus the propensity for Li loss through sublimation diminishes.[71, 138] Since, the amount of second phases (3 volume %), in the hot-pressed pellets is small their effects on the mechanical and electrochemical properties will be neglected and the results attributed only to single-phase cubic LLZO.

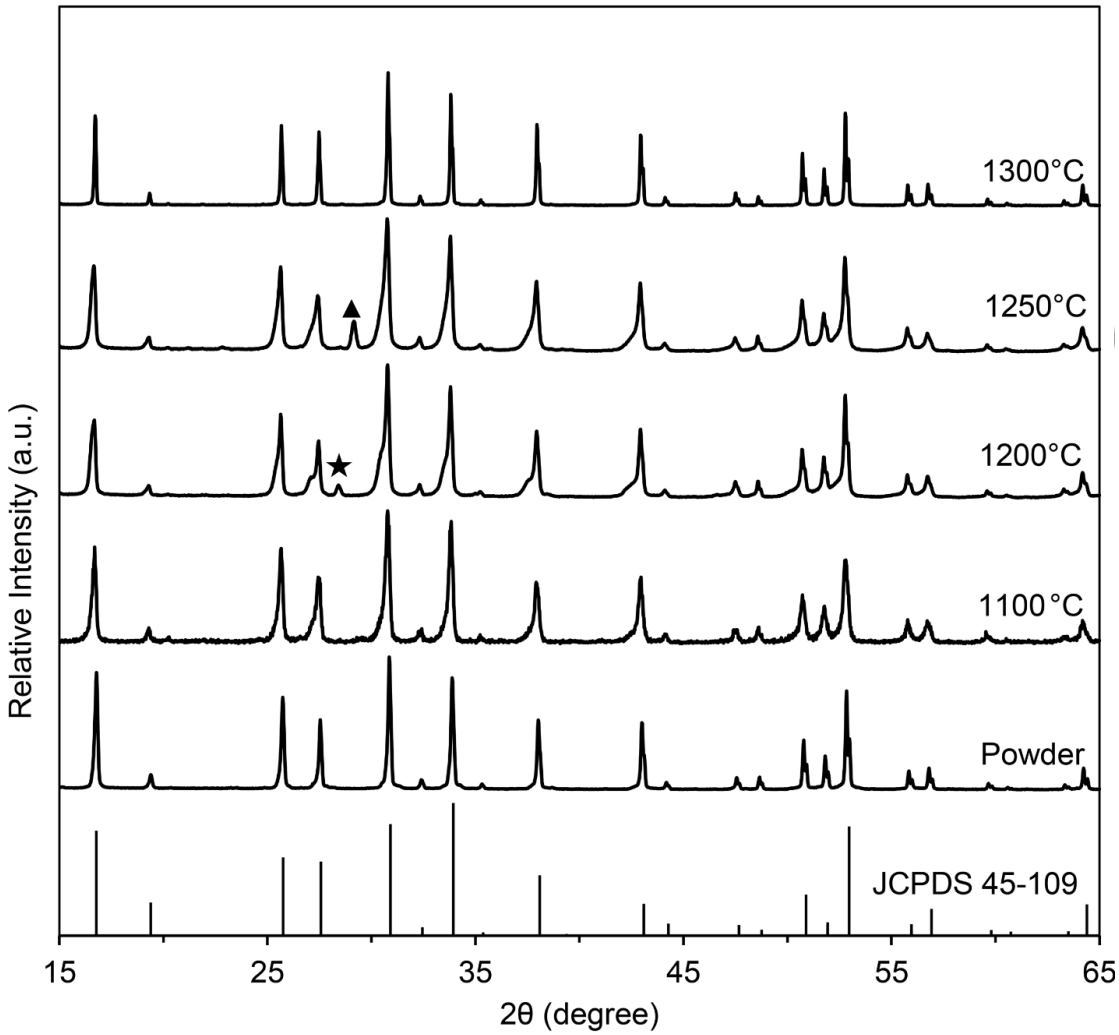

Figure 6.1. XRD patterns for LLZO calcined powder and pellets hot pressed between 1100 and 1300°C. Secondary phases: ▲ ($La_2Zr_2O_7$) and ★ ($La_{0.28}Zr_{0.72}O_{1.86}$). JCPDS file # 45-109 was used for cubic garnet.

Table 6.1. Summary of the LLZO crystallographic, physical, mechanical, and electrochemical properties.

	Phase Purity and Relative Density		Grain Growth		Mechanical Properties		Electrochemical Properties	
Pellet	Phase Purity	RD%	G_{ave} (μm)	Misorientation Angle (°)	H (GPa)	K_{Ic} (Mpa.m$^{-1/2}$)	σ_{total} (mS.cm^{-1})	CCD (mA.cm^{-2})
HP-1100°C	Cubic LLZO	96.0 ± 0.5	5 ± 2	20	9.88 ± 0.49	0.82 ± 0.07	0.46	0.3
HP-1200°C	4% Pyrochlore	97.7 ± 0.5	40 ± 13	35	8.05 ± 0.52	0.61 ± 0.05	0.52	0.4
HP-1250°C	2% Pyrochlore	98.1 ± 0.5	60 ± 20	40	7.74 ± 0.46	0.60 ± 0.06	0.54	0.4
HP-1300°C	Cubic LLZO	99.4 ± 0.5	80 ± 20	40	7.42 ± 0.48	0.61 ± 0.04	0.56	0.5
A-1300°C	Cubic LLZO	99.4 ± 0.5	600 ± 200	41	6.80 ± 0.49	0.60 ± 0.05	0.57	0.6

6.3.1.2 Microstructure

The relative density increased with increasing hot-pressing temperature, ranging between 96.0 ± 0.5 % and 99.4 + ± 0.5 % for the pellets hot-pressed between 1100 and 1300ºC, respectively (Table 6.1).

To further analyze the microstructural evolution as a function of hot-pressing temperature, scanning electron microscopy (SEM) analysis was conducted on polished surfaces (Figure 6.2). Additionally, optical images of the hot-pressed pellets are shown in Figure 6.2. From Figure 2, a trend between the volume fraction of porosity and optical transparency was apparent. As the hot-pressing temperature increased, porosity decreased, thus resulting in higher relative density and higher transparency. As the hot-pressing temperature increased, both porosity and grain boundary area decreased resulting in higher relative density and transparency. Typically, transparency in dense polycrystalline ceramics is achieved by eliminating defects such as porosity and/or secondary phases with different indices of refraction,[34] by increasing the densification temperature and/or time.[139-140] Thus, the observations made in this study are consistent with what is commonly observed when processing transparent polycrystalline ceramics. It is worth noting that the high relative densities achieved for all pellets likely

eliminated the porosity as a variable in the mechanical properties and electrochemical characterization analyses.

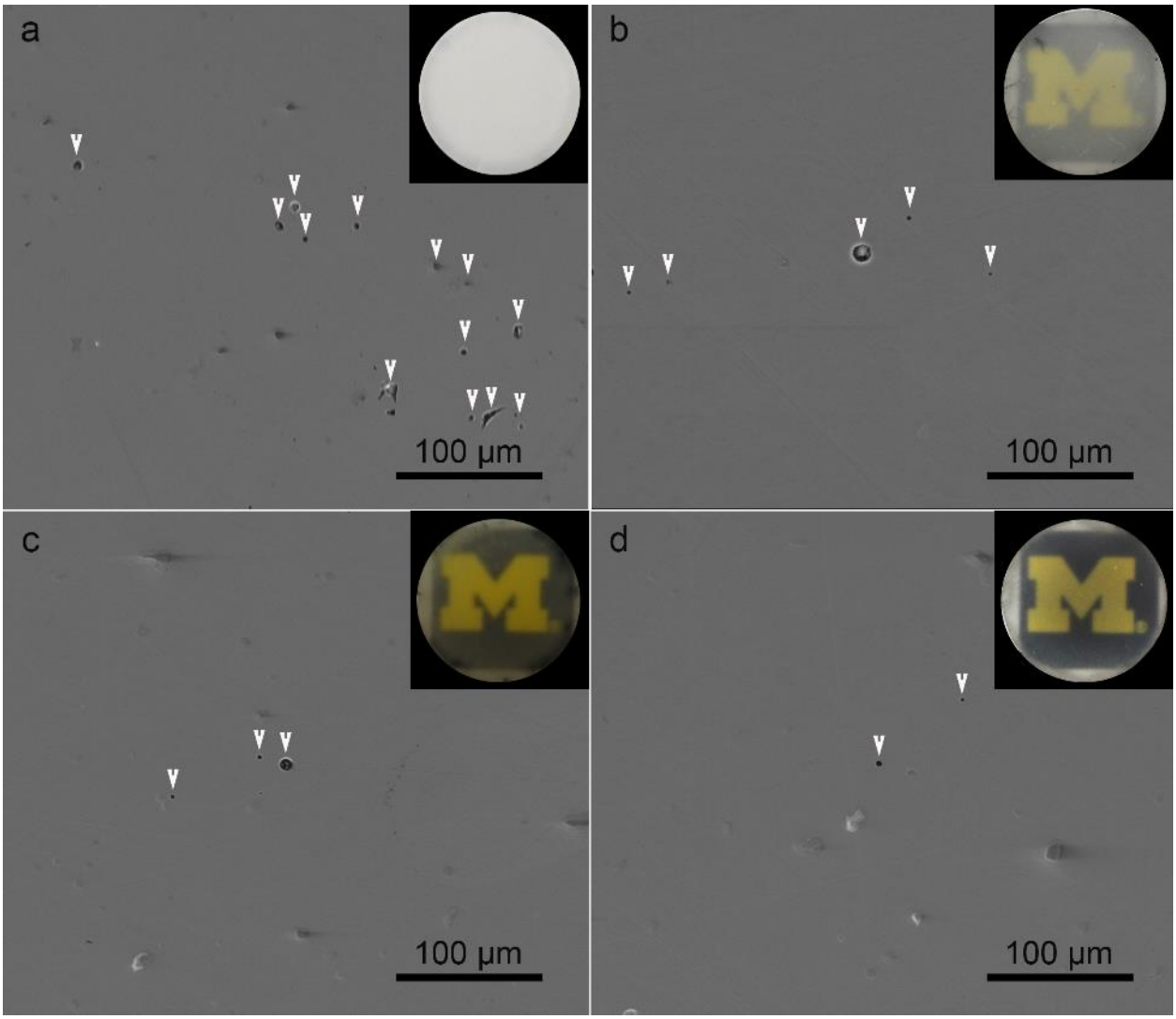

Figure 6.2. Secondary electron SEM images of polished LLZO pellets: a) HP-1100°C, b) HP-1200°C, c) HP-1250°C, and d) HP-1300°C. Arrows indicate pores. Insets are optical images of hot-pressed LLZO pellets (12.7 mm diameter).

6.3.2 Grain growth

Two methods were used to grow grains; 1) increasing the hot-pressing temperature and 2) hot-pressing at 1100^{o}C followed by annealing without pressure at 1300^{o}C for 50h. To characterize the effect of each method on the grain growth behavior, EBSD analysis was conducted after hot-pressing between 1100 and 1300°C, and annealing for 50 h (Figure 6.3, and

Figure 6.4). The average grain size was determined using histograms and grain size probability distribution curves obtained from EBSD grain orientation maps (Figure 6.5, and Figure 6.6). From the EBSD orientation maps in Figure 6.3, it was apparent that the average grain size increased with increasing hot-pressing temperature. Table 6.1 summarizes the average grain size as a function of hot-pressing temperature. As mentioned in experimental section, increasing the hot-pressing temperature to >1300°C resulted in significant Li loss, hence the maximum hot-pressing temperature was limited to 1300°C. Thus, to further amplify the effects of grain size on the mechanical and electrochemical properties, an alternative grain growth approach was used, which involved annealing the HP-1100°C LLZO at 1300°C for 50 h (A-1300°C). This approach resulted in significant grain growth with an average grain size of 600 ± 200 μm (Figure 6.4, and 6.6). To better understand the grain growth phenomenon, detailed EBSD analysis was conducted to correlate the effects of temperature, grain boundary curvature, and grain boundary misorientation.

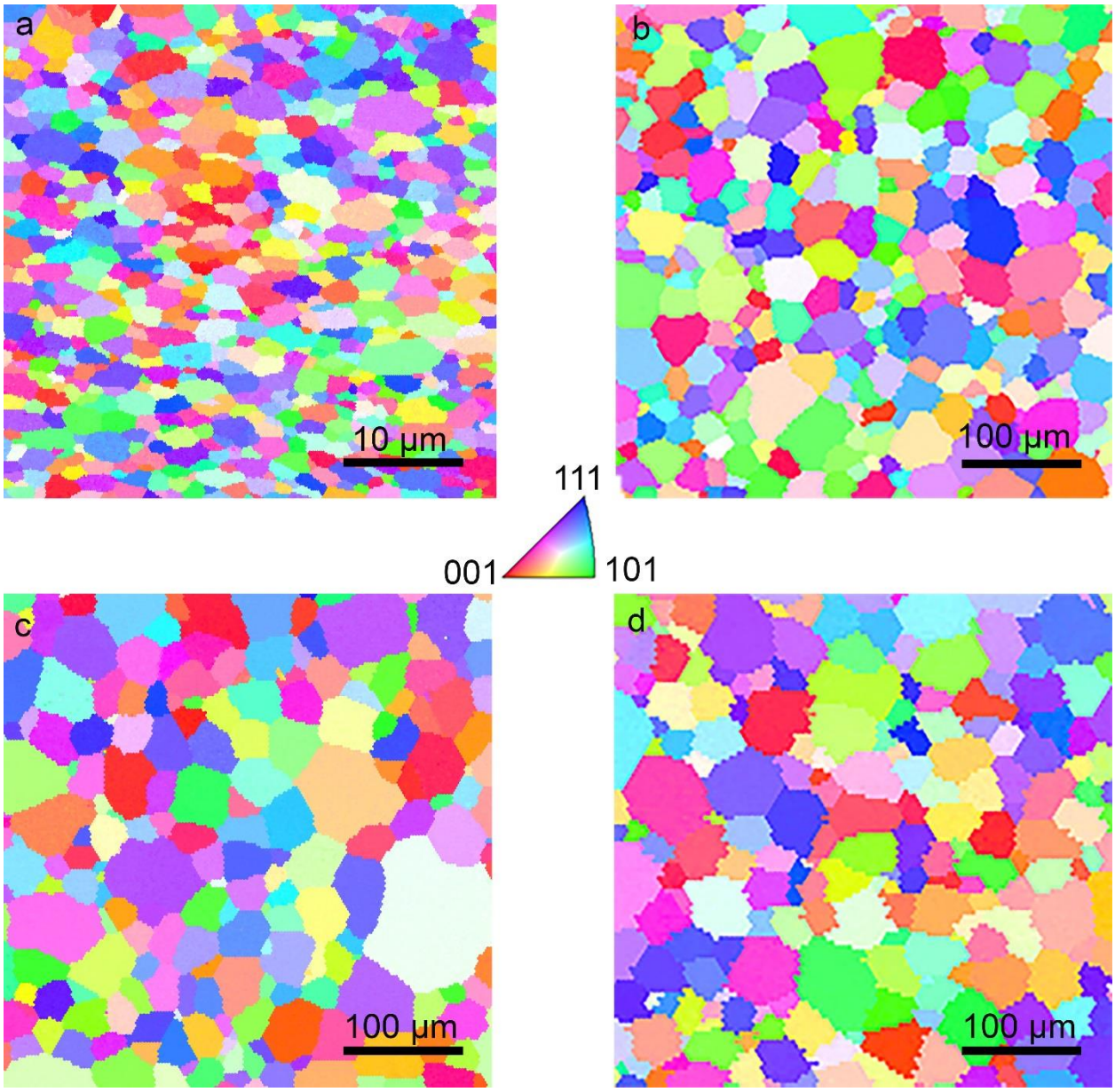

Figure 6.3. Electron backscatter diffraction grain orientation maps of LLZO pellets: a) HP-1100ºC, b) HP-1200ºC, c) HP-1250ºC and d) HP-1300ºC. The triangle in the center correlates color with crystallographic orientation**.**

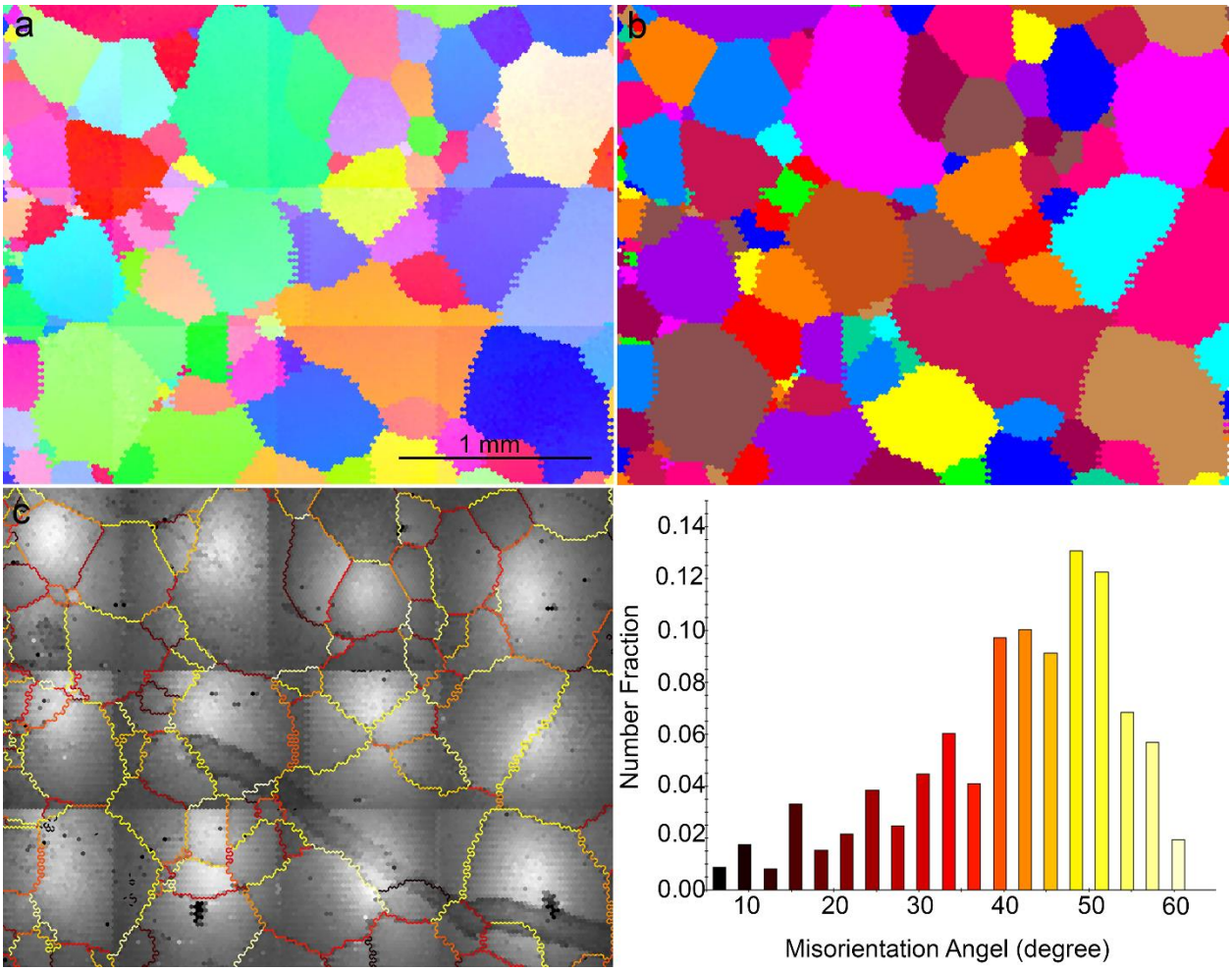

Figure 6.4. a) EBSD orientation map showing the evolution of LLZO microstructure, b) grain size map for annealed LLZO, c) Grain boundary misorientation angle map and histogram for A-1300ºC pellet.

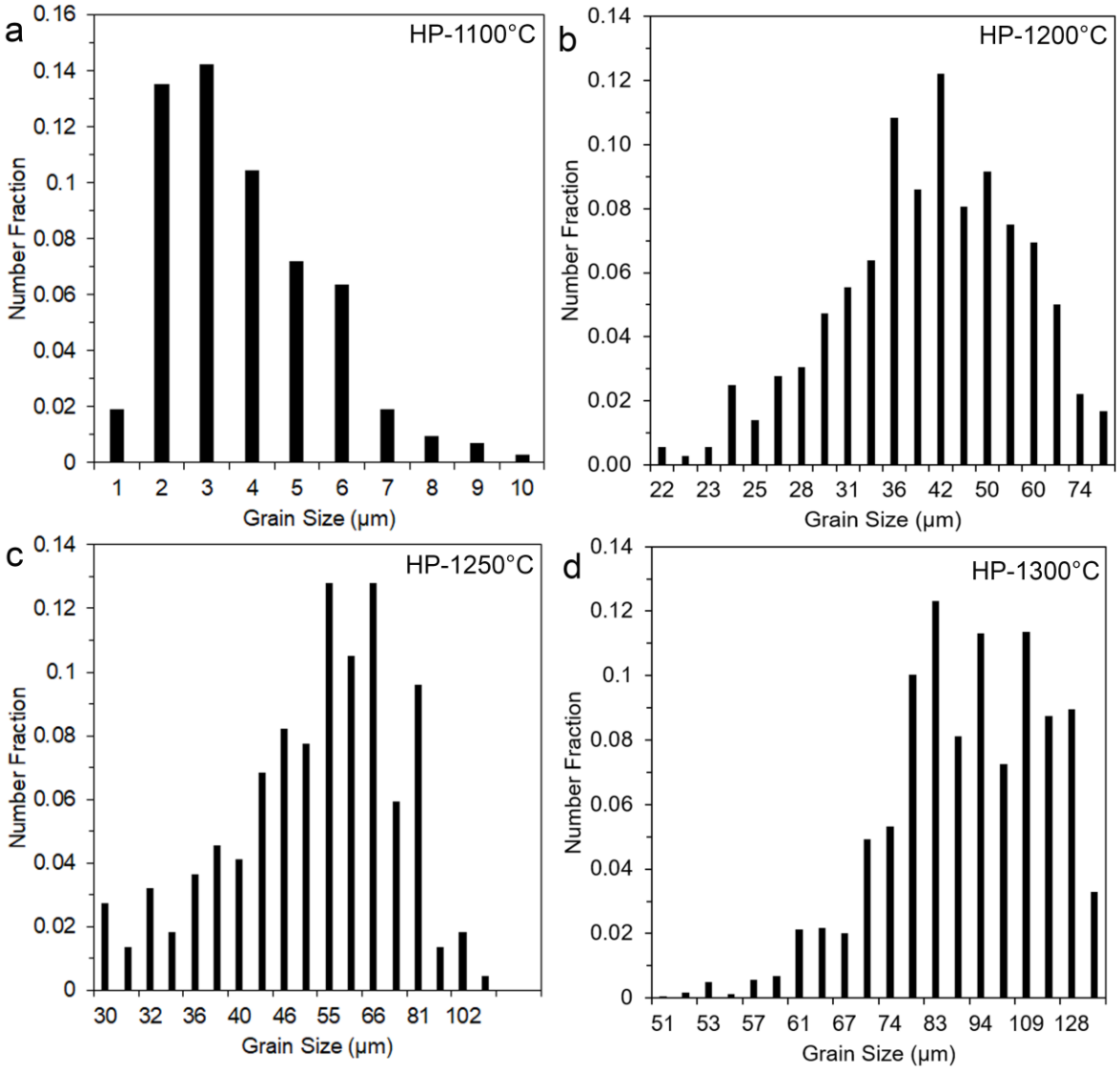

Figure 6.5. Corresponding histograms and probability distribution curves of grain sizes obtained from EBSD analysis on LLZO pellets: a) HT-1100ºC, b) HP-1200ºC, c) HP-1250ºC and d) HP-1300ºC.

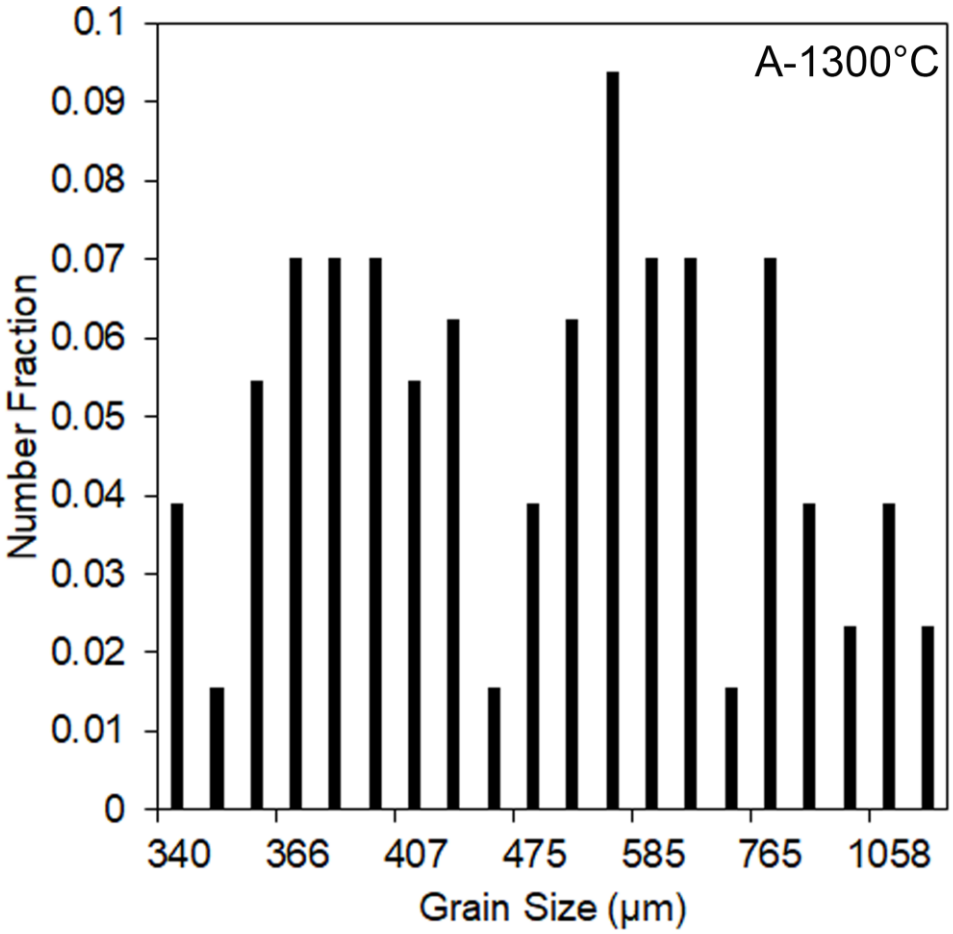

Figure 6.6. Corresponding histograms and probability distribution curves of grain sizes obtained from EBSD analysis on A-1300ºC LLZO pellet**.**

6.3.2.1 Effect of temperature

It was shown that the grain size increases with increasing hot-pressing temperature (Figure 6.7a). Based on previous studies, it has been observed that grain growth is strongly temperature dependent and typically increases with increasing temperature. [141-143] The relationship between grain size and temperature can be expressed by Equation (3):

$$d^n - d_0^n = k_0 \, t \exp(-\frac{Q}{RT}) \quad (3)$$

where d is the average grain size at a certain time (t), d_0 is the initial grain size, n is the grain growth exponent, Q is the activation energy for grain growth, R is the gas constant, T is the absolute temperature, and k_0 is an empirically derived proportionality constant. To determine the

dominant mechanism responsible for grain growth and rate-controlling species $\ln(d^n - d_0^n)$ for LLZO was plotted versus *1/T* using *n*=2 and *n*=3. It was observed that *n*=2 gave the best fit with R^2=0.96 (Figure 6.7b). An *n* value equal to 2 is usually associated with normal grain growth with no inhibiting second phases/impurities.[144-146] In contrast, *n*=3 is associated with grain growth controlled by impurity, pore or second phase drag.[147-148] The *n* value equal to 2 is in agreement with previous transmission electron microscopy results for hot-pressed LLZO, which revealed the absence of second phases or impurities along grain boundaries or triple junctions.[50, 149] In addition, since the LLZO tested in this study is of high relative density, pore drag is not expected to control grain growth. Furthermore, the activation energy for grain growth was determined from the slope of the line in the $\ln(d^2 - d_0^2)$ versus *1/T* plot shown in Figure 6.7b. The slope of the line yields an activation energy of 560 kJ.mol^{-1}. It is well known that the rate-controlling species for a grain growth of a ceramic is the slowest moving ion through the lattice or along grain boundaries.[150-151] For LLZO, it is expected that La ions, which occupy the dodecahedral sites because of their large size, should be the rate-controlling species. Thus, the activation energy value of 560 kJ mol^{-1} should be correlated with La diffusion in LLZO. At present, no activation energy values for diffusion of any of the species in LLZO except Li exist. However, for the case of another material with the same garnet structure as LLZO, yttrium aluminum garnet (YAG), lattice diffusion data exists for the diffusion of rare-earth elements (La, Nd, Dy and Yb) which occupy the dodecahedra sites and Ga, which occupies the tetrahedral and octahedral sites in YAG.[152] The activation energies for diffusion range are between 540 to 603 kJ.mol^{-1} for La, Nd, Dy and Yb, while the activation energy for Ga diffusion is lower, 404 kJ.mol^{-1}. In another study, both the activation energy for lattice and grain boundary diffusion of Yb in YAG was determined.[153] In this study, it was observed that the activation energy for grain

boundary diffusion of Yb in YAG was 530 kJ.mol^{-1}, while that for lattice diffusion of Yb in YAG was 560 kJ. mol^{-1}. For the case of yttrium iron garnet (YIG) activation energies for diffusion of Y and Fe in YIG are 502 and 362 kJ.mol^{-1}, respectively.[152] A comparison of the activation energy for grain growth of LLZO with cation diffusion data for YAG and YIG would suggest that the grain growth of LLZO is controlled by La diffusion. However, in another study, it was observed that the activation energy for grain boundary diffusion of Yb in YAG was 530 kJ.mol^{-1}, while that for lattice diffusion of Yb in YAG was 560 kJ.mol^{-1}.[14] In this study the activation energy for diffusion of the dodecahedral ion in the lattice and along grain boundary are similar. Hence, to conclusively confirm that the grain growth of LLZO is controlled by La diffusion, cation (La, Zr) diffusion in LLZO through the lattice and along grain boundaries is needed.

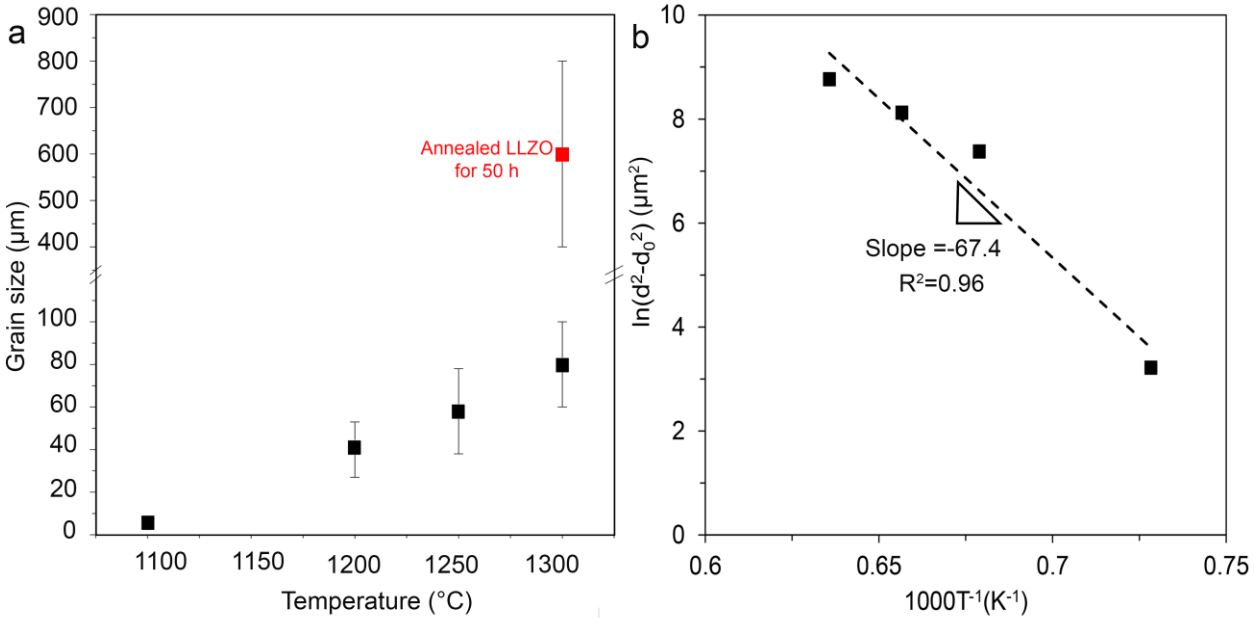

Figure 6.7. LLZO grain growth data: a) grain size as a function of hot-pressing temperature and b) plot of average grain size for LLZO pellets at hot-pressing temperature ranging from 1100 to 1300°C. The experimental values are compared to the predictions made by Equation. (3) for the grain growth mechanism.

6.3.2.2 Effect of grain boundary curvature

To better understand the effect of grain boundary curvature on grain growth kinetics, EBSD orientation maps were analyzed (Figure 6.3). From Figure 6.3 several observations can be made. First, the grains can be categorized into three types: type I) grains with six sides which have straight boundaries, type II) grains with less than six sides which have concave grain boundaries (when observed from the center of the grain), and type III) grains with more than six sides which have a mixture of concave and convex grain boundaries. Second, the hot-pressing temperature affects the microstructure. For example, the lower hot-pressing temperature (HP-1100°C) resulted in grains with less than six sides and concave grain boundaries, while higher hot-pressing temperatures ($\geq$1200°C) resulted in a higher fraction of grains with more than six sides and convex grain boundaries. Third, hot-pressing at T$\geq$1200°C, the type III grains were typically surrounded by type II grains. De Jonghe and Rahaman have shown that grain boundary trajectory and the mass transport during grain growth is controlled by chemical potential gradients related to the curvature of grain boundaries;[154] i.e. the atoms under a convex surface have a higher chemical potential than the atoms under a concave surface.[141, 154-155] The Gibbs-Thompson Equation (4) correlates the chemical potential gradient $\Delta\mu_{gb}$ with grain boundary curvature:[141, 154]

$$\Delta\mu_{gb} = \gamma_{gb}\Omega_{MX}k \quad (4)$$

where γ_{gb} is the grain boundary energy, Ω_{MX} is the volume of a formula unit, and k is the radius of curvature. The difference in the chemical potential energy across the grain boundary is what moves the grain boundary away from its center and is the driving force for grain growth. Based on Equation. (4), the type I grains with six sides and flat grain boundaries are stable and immobile, while grains with more than six sides with a positive curvature tend to grow at the

expense of the smaller grains that have fewer than six sides and negative curvature. Thus, the larger grain size in LLZO pellets hot-pressed at T≥1200°C can be attributed to the presence of more type II grains. Furthermore, the presence of curved grain boundaries in the microstructure of LLZO pellets show the potential for more grain growth upon holding time at high temperature. This phenomenon was confirmed by annealing LLZO after hot-pressing which shows more grain growth and significant increase in grain size (600 μm). For better clarification, Figure 6.8 shows the direction of grain boundary migration during grain growth.

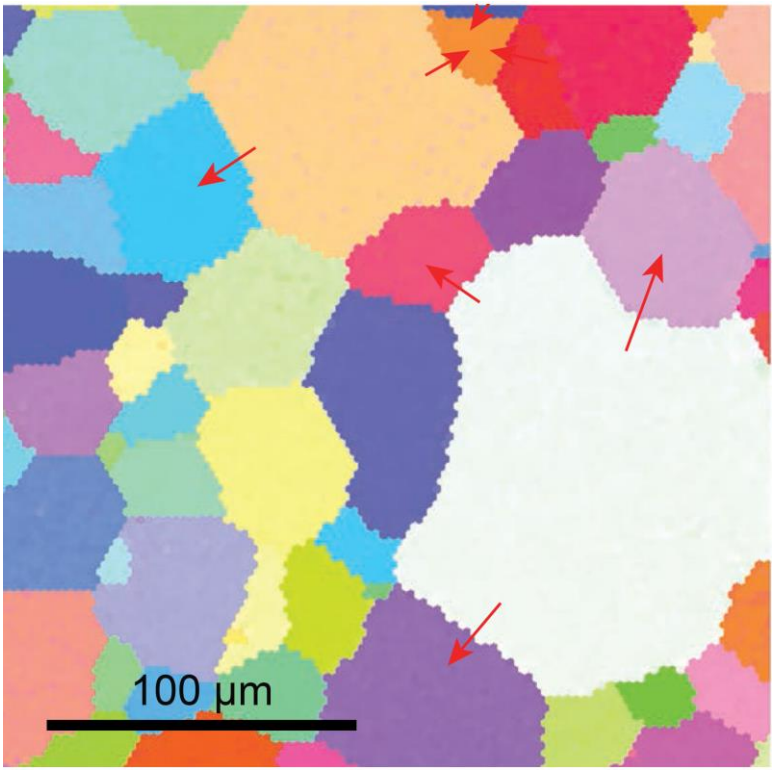

Figure 6.8. Representative EBSD orientation map of LLZO hot-pressed at 1250ºC highlighting projected grain boundary trajectories during grain growth.

6.3.2.3 Effect of grain boundary misorientation angle

To further examine effect of grain boundary on the grain growth, the influence of grain boundary misorientation angle was investigated. The misorientation angle maps and histograms for LLZO pellets hot-pressed at different temperatures are shown in Figure 6.9. The same

analysis was conducted on the A-1300ºC (Figure 6.4). From Figure 6.9 and Figure 6.4c, several observations can be made. First, a wide range of misorientation angles between 0 and 65º were observed in all LLZO pellets. Second, there is a clear difference in the fraction of low to high misorientation angles comparing the HP-1100°C, HP-1200°C, HP-1250°C, HP-1300°C and A-1300°C LLZO pellets. The average misorientation angles calculated from the histogram plots in Figure 6.9 are listed in Table 6.1. It is apparent that the average misorientation angles were affected by the hot-pressing temperature. For example, the HP-1100ºC LLZO pellet had a higher fraction of low misorientation angles (<20º), while the LLZO pellets hot-pressed at ≥1200ºC and A-1300ºC had a higher fraction of boundaries with >35º misorientation. It has been shown by Barrett *et al.* working on aluminum with cubic structure that the degree of grain boundary misorientation is one of the primary factors influencing grain boundary mobility; i.e. the higher the misorientation angle, the higher the grain boundary mobility, hence the higher the grain growth rate.[156] It was shown that grain boundary mobility was negligible for grain boundaries with misorientation angles <15-20º whereas grain boundary mobility increased with higher misorientation angles.[157-158] In a related study, it was shown that the highest grain growth rate occurred when the misorientation angle was ≥ 40º.[159-163] Turning back to this study, the EBSD analysis corroborates the general trend between grain boundary misorientation angle and the grain size (Figure 6.9). The LLZO pellets with the larger average grain size, exhibited higher misorientation angles, especially when hot-pressing at ≥1200ºC and in the A-1300°C pellet. For example, all pellets but the HP-1100ºC, had grain boundary misorientation angles between 35º and 40º, while the HP-1100ºC LLZO pellet had an average misorientation angle of ~20º.

The effect of LLZO processing conditions on the grain size was studied to understand the phenomena that govern grain growth kinetics. It was determined that the processing temperature,

grain boundary curvature, and grain boundary misorientation angle are important factors in controlling grain growth in LLZO. Moreover, the activation energy for grain growth and grain growth exponent revealed that hot-pressed LLZO exhibited normal grain growth rate-limited by La diffusion. We believe that an understanding of grain growth will facilitate future efforts to integrate LLZO into solid-state batteries, specifically with regard to mechanical integrity and electrochemical performance as is discussed in subsequent sections.

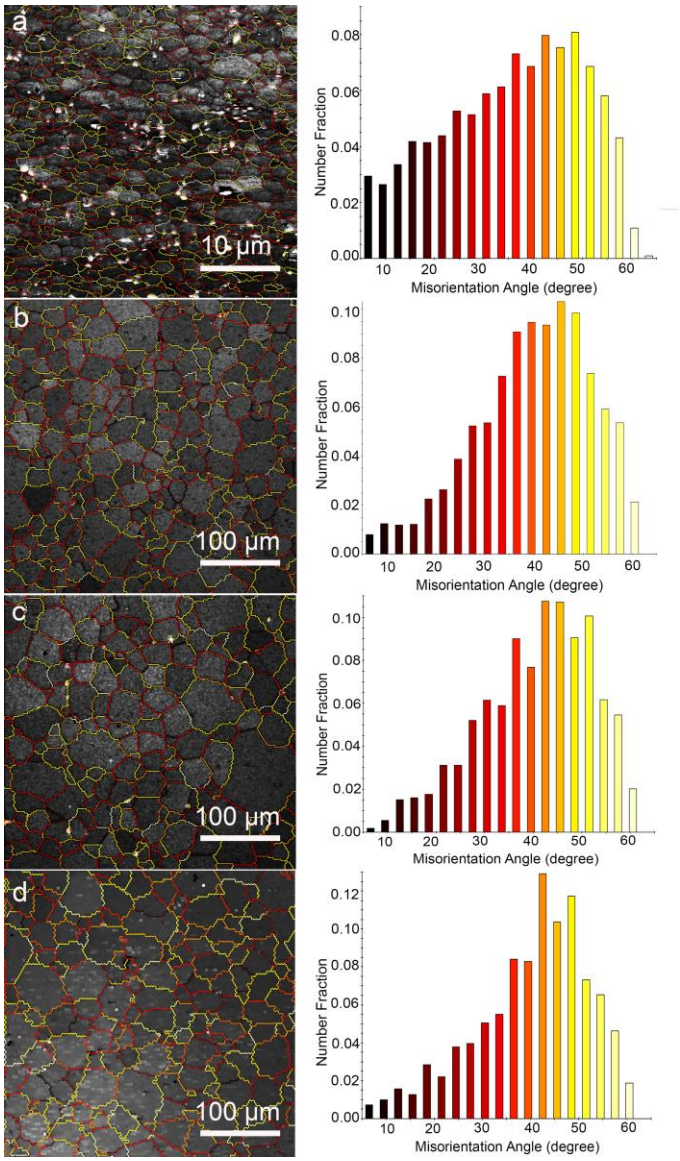

Figure 6.9. Grain boundary misorientation angle maps and histograms for LLZO pellets: a) HP-1100ºC, b) HP-1200ºC, c) HP-1250ºC, and d) HP-1300ºC**.**

6.3.3 Mechanical properties characterization

6.3.3.1 Hardness

Vickers indentation was used to correlate LLZO grain size with hardness (H) (Figure 6.10a, b). From Figure 6.10a it can be observed that hardness decreased from 9.88 ± 0.49 GPa to 6.86 ± 0.49 GPa as the average grain size increases from 5 µm to 600 µm, respectively. The HP-1100^{o}C H value for the 5 µm grain size pellet agrees with the H value measured by Kim *et al.* (9.1 ± 0.1 GPa) on hot-pressed LLZO with the same composition and similar grain size.[164] The H was correlated with the grain size (Figure 6.10b) using the Hall-Petch relationship shown below, Equation. (5):[165]

$$H = H_0 + K_H d^{-1/2} \quad (5)$$

where d is the grain diameter, H_0 is the ordinate axis intercept corresponding to the hardness of a single crystal, and K_H is the slope of the straight line drawn through the data and corresponds to a material strengthening constant. Plotting the data from this study using Eq. (5) gives the relationship: $H = 6.80 + 6.93\ d^{-1/2}$ with a R^2 value equal to 0.98. The high R^2 value indicates that the correlation between grain size and H follows the Hall-Petch relationship. Furthermore, the LLZO single crystal H value can be estimated with confidence to be 6.80 GPa. The H values were used to estimate the fracture toughness as a function of grain size using Equation.2.

6.3.3.2 Fracture toughness

The fracture toughness (K_{IC}) was measured as function of grain size using Vickers indentation (Figure 6.10c). First, it was observed that the HP-1100^{o}C LLZO pellet with the smallest average grain size (5 µm) has the highest fracture toughness (0.82 ± 0.07 MPa.m$^{-1/2}$). This value is in good agreement with the K_{IC} value of 0.97± 0.10 MPa.m$^{-1/2}$ for a sample of the same relative density and similar composition, but slightly smaller grain size of ~3 µm.[164]

Second, it was observed that as the average grain size increased from 5 μm to 40 μm, the fracture toughness decreased from 0.82 ± 0.07 MPa.m$^{-1/2}$ to 0.60 ± 0.05 MPa.m$^{-1/2}$, respectively. As the grain size further increased ($\geq$ 40 μm), the fracture toughness remained relatively constant at ~0.60 MPa.m$^{-1/2}$. The fracture toughness insensitivity to grain size at $\geq$40 μm could be explained by comparing the size of the indentation crack length with the LLZO grain size. In this study, the indentation total crack lengths (twice the distance from the center of the Vickers indentation to the crack tip) were typically ~25 μm. Thus, when the total indentation crack length was greater than the LLZO grain size, crack propagation was likely impeded by grain boundaries resulting in an increase in fracture toughness. [137, 164] However, when the grain size was greater than the total indentation crack length, on average, the likelihood of grain boundaries impeding crack propagation significantly diminished, resulting in a reduction in fracture toughness compared to the LLZO with 5 μm grains. Thus, at grain sizes $\geq$ 40μm the fracture toughness should correspond to the LLZO single crystal. [137]

Using the single crystal fracture toughness value (0.60 MPa.m$^{-1/2}$) and E ~150 GPa as reported by Yu *et al.*,[54], also allows for estimation of the fracture surface energy (γ). γ was calculated using Eq. (6):

$$\gamma = \frac{K_{IC}^2}{2E} \quad (6)$$

The fracture surface energy is estimated to be 1.24 J.m^{-2}, which is in good agreement with γ values for typical single crystal ceramics (0.5-3 J.m^{-2})[166] including LLZO.[164]

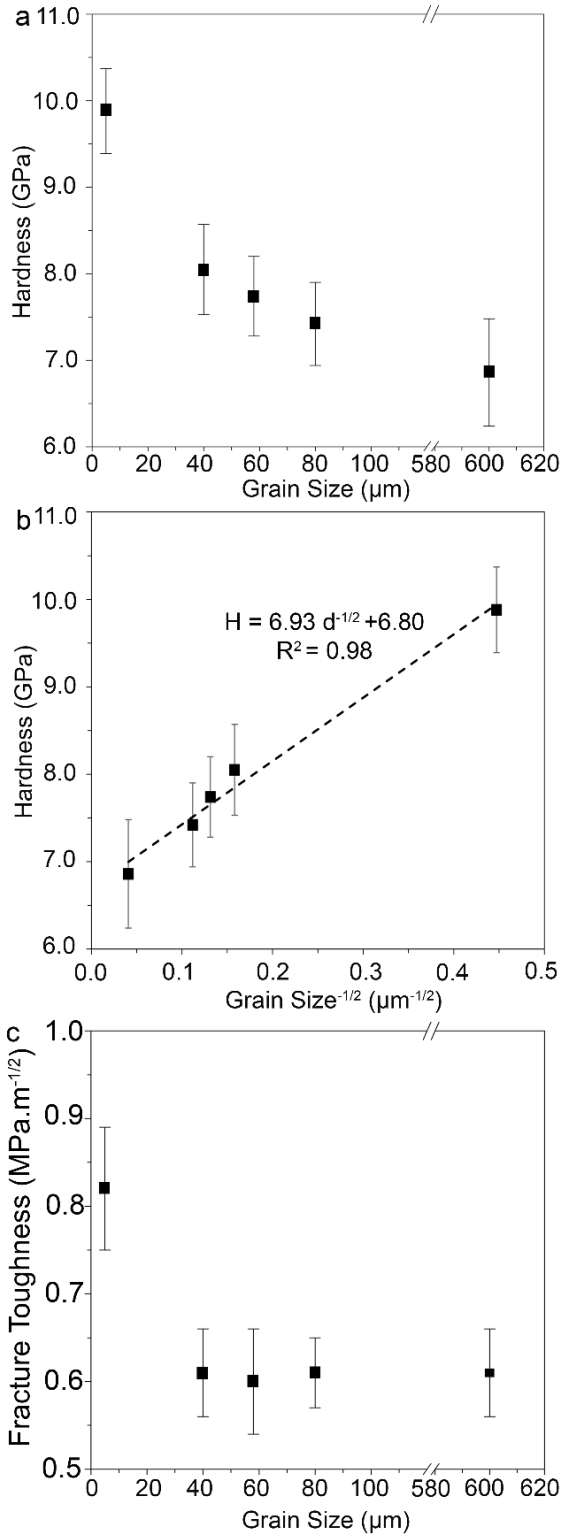

Figure 6.10. Mechanical property analysis of LLZO as a function of grain size. Vickers hardness: a) as a function of grain size, b) as a function of the inverse square root of grain size (data follows the Hall-Petch relationship), and c) LLZO fracture toughness as a function of grain size. Error bars represent the hardness standard deviation from the mean (N= 10).

6.3.4 Electrochemical characterization

To evaluate the effect of LLZO grain size on the electrochemical stability (or critical current density, CCD), a combination of DC cycling and EIS analysis was performed on Li-LLZO-Li symmetrical cells (Figure 6.11). After cell assembly and preconditioning, EIS was conducted and the data were fitted with an equivalent circuit (Figure 6.11a) to determine the individual impedance contributions to the total cell impedance. The total cell impedance comprised the LLZO bulk (Z_{bulk}), grain boundary (Z_{gb}), and Li-LLZO interfacial ($Z_{Li\text{-}LLZO}$) impedances. A representative EIS spectrum for a cell consisting of an A-1300ºC LLZO pellet is shown in Figure 6.11b. Analysis of the EIS spectrum determined that a remarkably low $Z_{Li\text{-}LLZO}$ of 2 $\Omega.cm^{-2}$ was achieved using the previously reported LLZO heat-treatment prior to cell assembly.[167] It was also apparent that the LLZO total impedance (Z_{bulk}+Z_{gb}) was the primary contribution to the total cell impedance. The LLZO total impedance was ~300 $\Omega.cm^2$, which is consistent with the values reported previously for LLZO with the same composition and high relative density.[115-116, 127] All the cells had consistently low $Z_{Li\text{-}LLZO}$ (in the range of 2 to 5 $\Omega.cm^2$), eliminating the effect of Li-LLZO interfacial impedance on the CCD. Therefore, the only variable between cells was the LLZO grain size.

A representative DC cycling voltage profile of a Li-LLZO-LI cell consisting of an A-1300ºC LLZO pellet (600 ± 200 µm average grain size) is shown in Figure 6.11c. The cell followed Ohmic behavior (V=IR) at lower current densities, but exhibited a sudden drop in polarization voltage at 0.6 $mA.cm^{-2}$. Thus, the CCD was determined to be 0.6 $mA.cm^{-2}$; this value is one of the highest values reported in literature for an all solid state Li-LLZO cell.[57, 59-60, 63, 74, 115, 119, 127] The EIS conducted on the cell after the CCD was exceeded (Figure 6.11b, close circle), indicated a different behavior compared to previous reports on similar short-circuited symmetric cells.[115,

[127] First, as mentioned above the total cell impedance was ~300 $\Omega.cm^2$ before the CCD was exceeded; however, after the CCD was exceeded the total cell impedance (diameter of the semicircle) decreased to ~ 70 $\Omega.cm^2$. Second, the high frequency intercept no longer extended to the origin, but instead terminated on the Z_{real} axis at approximately 30 $\Omega.cm^2$. We believe the $Z_{uncompensated}$ increased based on the equivalent circuit model fitting. The reason for the increase is not known at this time, but we believe it could be related to the short-circuiting phenomenon.[115, 127] The same short-circuiting behavior was observed in the other LLZO pellets in this study with an average grain size $\geq$40 μm. More work is necessary to better interpret the EIS spectra after short-circuiting in solid-state cells.

The CCD for Li-LLZO-Li cells using LLZO pellets with average grain sizes ranging between 5 to 600 μm is shown in Figure 6.11d. With increasing average grain size, the CCD increases from 0.3 $mA.cm^{-2}$ to 0.6 $mA.cm^{-2}$. These observations confirm that LLZO with larger average grains size can exhibit a higher CCD. Currently, we believe the correlation between increasing CCD and increasing grain size can be attributed to the reduction in the grain boundary area and/or the number of failure points per unit area at the Li-LLZO interface. It should be noted to achieve much higher current density and avoid failure due to short-circuiting and Li propagation along the grain boundaries, all the failure points should be eliminated from the microstructure. In other words, the LLZO ideally should be used in its single crystalline form. From Table 1 it should be noted that the smallest grain size of 5 μm exhibited a different value for the misorientation angle, total conductivity and fracture toughness compared to the four larger grain size samples. Thus, it is possible that not only grain size but misorientation angle could affect the CCD. However, if this grain size is ignored the trend shown in Fig. 8d is still valid, that increasing grain size leads to a high CCD, since from Table 1 it is observed that the

four larger grain size samples all exhibit similar values for the misorientation angle, total conductivity and fracture toughness, the only variable between them is grain size.

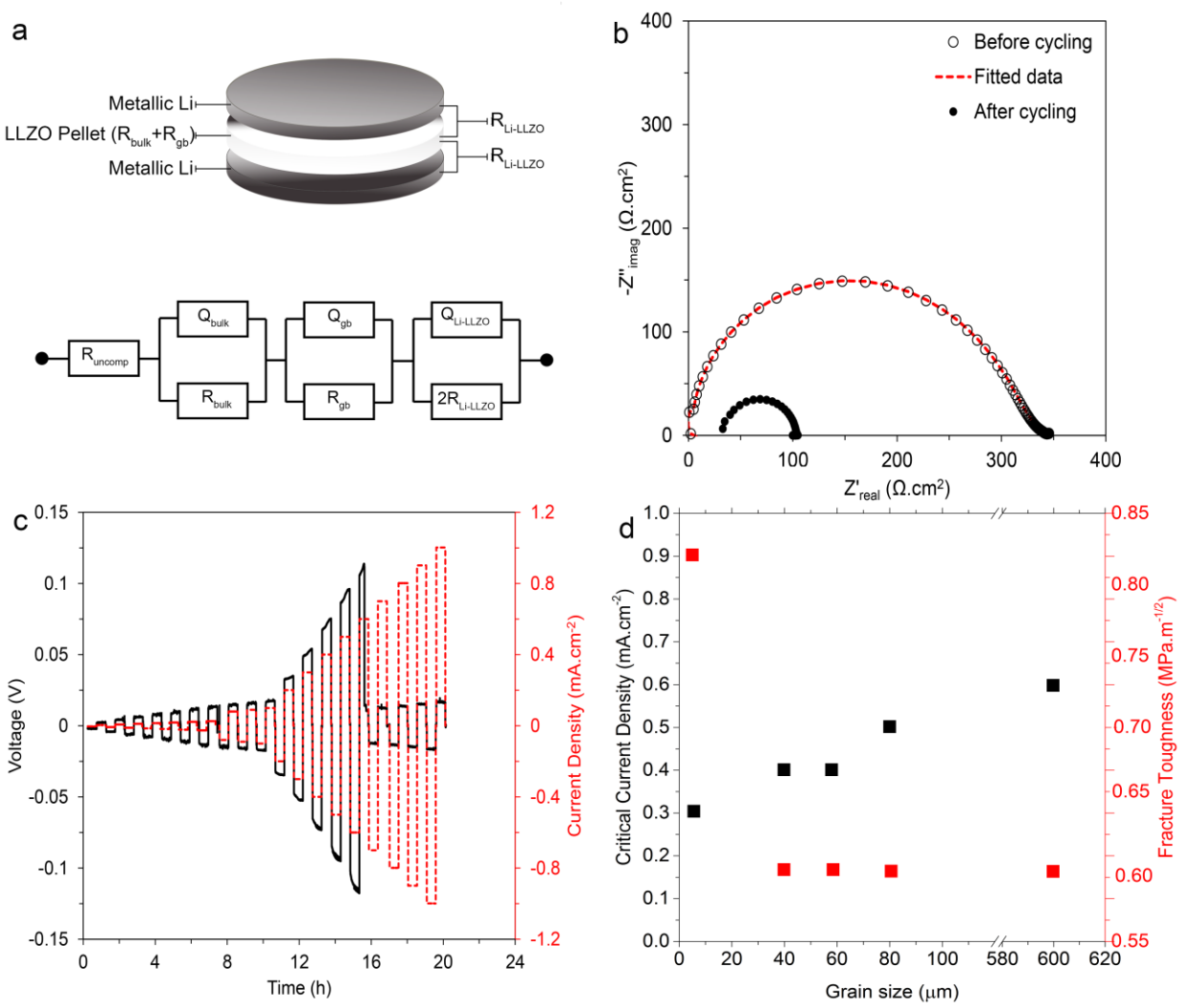

Figure 6.11. AC and DC electrochemical measurements. a) Schematic diagram of the all solid-state Li-LLZO-Li cell configuration and the equivalent circuit used to model the EIS data, b) a representative Nyquist plot of the Li-LLZO-Li cell before (○) and after (●) cycling (LLZO; A-1300oC). Markers indicate experimental data and dotted lines are simulated lines extrapolated using the equivalent circuit model shown in a, c) DC cycling of Li-LLZO-Li cell (LLZO; A-1300oC) at room temperature, stepping the current density from 0.01 to 1 mA.cm-2, 30min in each polarization orientation, and d) the CCD and fracture toughness (taken from Fig 7c) as a function of grain size.

6.4. Discussion

Previous studies in which DC cycling was performed to evaluate the electrochemical stability of polycrystalline LLZO against metallic Li, observed short-circuiting when the CCD was exceeded.[59-62, 115, 127] It is generally believed that exceeding the CCD is accompanied by Li metal filament propagation when short-circuiting occurs. However, little is known about the parameters that govern the CCD and short-circuiting in a polycrystalline LLZO. There have been several hypotheses proposed to determine what factors control the CCD. Some are based on theory suggesting that mechanical properties such as the shear modulus have an effect on governing the CCD.[52, 85] For example, Monroe *et al*. proposed that if the shear modulus of a SSE is greater than a factor of two higher than the shear modulus of Li (4.8 GPa), dendrite initiation should not occur.[52] In hypotheses based on experimental data, it has been suggested that microstructural features such as the grain size and/or grain boundaries have an effect on governing the CCD.[97, 127] In studies investigating the initiation and propagation of Na metal through the polycrystalline sodium beta alumina (SBA), it was determined that the CCD was affected by the fracture toughness (K_{IC}) of the SSE.[85, 168] It was shown that the higher the SBA fracture toughness, the higher the CCD, Equation. (7):

$$CCD = \frac{AK_{IC}^4}{\eta}\frac{c^2}{l^3} \quad (7)$$

where A is a constant, η is viscosity of the metal, and $\frac{c^2}{l^3}$ captures the flaw size in microstructure. According the Eq. 7, the CCD was very sensitive to any change in the fracture toughness, e.g. $(K_{IC})^4$. In a more relevant study on LLZO, *L.* Cheng *et al.* showed that the CCD is strongly correlated to the grain size. It was shown that small grain LLZO exhibited a higher CCD compared to large grains. The improved cycling behavior was attributed to the to larger relative area fraction of grain boundaries at the Li-LLZO interface, which is counter to the observations

in this study.[74] In contrast, *E. J.* Cheng *et al.*, using SEM and high spatial resolution Auger spectroscopy, showed that metallic Li preferentially propagates along the grain boundaries when the CCD is exceeded in hot-pressed LLZO. Likewise, it was suggested that elimination of grain boundaries as failure points from polycrystalline LLZO could increase the CCD. The purpose of this study was to correlate the effect of grain size, and the resulting changes in mechanical and electrochemical properties, on controlling the CCD. Table 6.1 summarizes the results obtained for phase purity, relative density, average grain size, mechanical properties and electrochemical properties in all LLZO pellets.

6.4.1 Impact of mechanical properties on CCD

Because the elastic modulus is a material intensive property, in general grain size does not affect the elastic properties such as shear modulus.[136, 165, 169] Though in some cases porosity can affect the effective modulus, all samples analyzed in this work had high relative densities, thus it was assumed that the elastic modulus values for the hot-pressed pellets used in this study agree with previously reported values on dense LLZO pellets.[164, 170-171] For example, Ni *et al.* and others determined the shear modulus of LLZO to be 58-60 GPa, which is more than 10 times higher than shear modulus of metallic Li.[53-54] Hence, despite meeting and exceeding the shear modulus criterion proposed by Monroe *et al*., the DC cycling of Li-LLZO-Li symmetric cells have shown a sudden drop in polarization voltage at current densities <0.5 $mA.cm^{-2}$, which is consistent with short-circuiting or Li metal propagation.[52] This confirms that the Monroe model is not applicable to polycrystalline LLZO. Hence, the shear modulus is not or cannot be the only parameter controlling the Li-LLZO interface stability.

Microstructural features such as the grain size, secondary phases, and porosity can affect hardness and fracture toughness.[136, 141, 170, 172-173] In this study, it was assumed that the fraction of

secondary phases and porosity were negligible and that the only microstructural feature to affect the non-elastic mechanical properties was the grain size. To evaluate effect of fracture toughness on CCD, the influence of grain size on fracture toughness was studied. The fracture toughness of LLZO decreased with increasing grain size from 5 to 40 μm and remained constant for LLZO with grain sizes $\geq$ 40 μm. This suggests that if fracture toughness was the only factor controlling the CCD, that LLZO with grain sizes $\geq$ 40 μm should have exhibited a lower CCD compared to LLZO with an average grain size of 5 μm. However, the DC cycling measurements between 0.01 and 1.0 $mA.cm^{-2}$ determined that the CCD increased with increasing grain size while the fracture toughness remained constant (~0.60 $MPa.m^{-1/2}$) (Figure 8d). In fact, the CCD doubles with increasing grain size from 5 to 600 μm while the fracture toughness decreases from 0.82 ± 0.07 to 0.60 ± 0.05 $MPa.m^{-1/2}$, respectively. Based on these observations, it is unlikely that there was a correlation between the fracture toughness and the CCD in this study. Moreover, we believe that mechanical properties (elastic or non-elastic) may not affect the LLZO CCD as previously believed.

6.4.2 Impact of microstructural features on CCD

The effect of grain size on the cycling behavior and stability of LLZO against metallic Li was studied. For this purpose, the average grain size was varied over a wide range by hot-pressing between 1100 and 1300°C and by annealing hot-pressed LLZO at 1300°C for 50 h. The average grain size increased from 5 ± 2 to 600 ± 200 μm. As described in sections 2.1.1 and 2.1.2, the LLZO pellets examined here contained no secondary phases, were close to the theoretical density, and had consistent and low Li-LLZO interfacial impedance between 2 and 5 $\Omega.cm^2$. By controlling these material aspects, the grain size was successfully isolated as the only variable to change among the cycled LLZO pellets. Our results show that by increasing the grain size, and

effectively lowering the grain boundary area per unit area of Li-LLZO interface, an increase in CCD was achieved. The findings of this study contradict the outcomes of the study conducted by L. Cheng *et al.* who observed the opposite trend, i.e. the CCD increased as the grain size decreased. The improved cycling stability was attributed to the larger relative area fraction of grain boundaries at the Li-LLZO interface, which was also believed to reduce the Li-LLZO interfacial impedance.[97] For example, in the L. Cheng *et al.* study, the LLZO pellets consisting of smaller grains exhibited one-third the interfacial impedance, compared to the LLZO pellets with larger grains at the Li-LLZO interface. It is also possible that the difference in the effect of grain size on the critical current density for this study and that of L. Cheng *et al*. could be a result of the nature of the grain boundaries formed during hot-pressing versus sintering. The grain boundaries formed during hot-pressing typically exhibit increased strength compared to those formed during sintering. This may explain why the fracture mode of the hot-pressed material in this study was nearly all transgranular while the fracture mode of pressure-less sintered LLZO primarily consisted of intergranular fracture. Typically, transgranular fracture is associated with high grain boundary strength while intergranular fracture is associated with relatively low grain boundary strength. Lastly, it is possible that the grain boundary chemistries were not comparable based on the different densification techniques and conditions. Altogether, due to the numerous differences in processing conditions and the impact each may have on the microstructural aspects, we believe it would be difficult to correlate the CCD behavior of the LLZO in this study and the LLZO prepared by Cheng *et al*. In related work, it has been shown that the CCD was inversely correlated with the Li-LLZO interfacial impedance; the lower the interfacial impedance, the higher the CCD.[115] Owing to its possible influence on the CCD, the interfacial impedance was not a variable in this work, suggesting that the effect of grain size was isolated.

The correlation between grain size and CCD in this study are consistent with the findings reported by E.J. Cheng *et al*. who observed Li metal propagation along grain boundaries when the CCD was exceeded in Li-LLZO-Li cells.[127] It follows that if grain boundaries are initiation points for Li metal propagation into LLZO, the lower the relative area/volume fraction of grain boundaries, the less likely Li metal propagation will occur. It could be argued that increasing the grain size would increase the current density through the grain boundaries, thereby decreasing the effective CCD; however, the results of this study suggest the opposite is true; i.e. the CCD increases with increasing grain size. The results of this study suggest that increasing the CCD of LLZO can be achieved by increasing the grain size or minimizing or altogether eliminating grain boundaries (single crystal).

We believe that the outcomes of this work could have both broad scientific and practical implications. First, ostensibly, it has been believed that the CCD of LLZO should be governed by the same or similar mechanical property phenomena that control the stability of related SSE models or systems.[18-20] However, perhaps due to differences in material property assumptions, some existing hypotheses used to predict the CCD may not be consistent with the observations made in this work, i.e. the Monroe model is predicated on uniform ionic conductor, while LLZO conducts ions through the bulk and grain boundaries.[18] Moreover, the findings from this and other recent work indicate that the mechanical properties of LLZO may not affect the CCD as previously suggested. Instead, these findings may point to other phenomena that have more profound effects in governing the CCD that have yet to be discovered. Clearly, more in depth studies are needed to better understand what triggers Li metal propagation in LLZO. Second, the highest room temperature CCD (0.6 $mA.cm^{-2}$) was demonstrated with 600 μm average grain size LLZO. Taken together, our study correlates the effect of LLZO grain size and the Li-LLZO

stability as a function of Li plating rate. By controlling the microstructure, a straightforward pathway towards viable solid-state batteries can be achieved.

6.5 Conclusions

Achieving current densities $\geq$ 1 mA.cm^{-2} is a necessary condition for a viable solid-state electrolyte to enable the use of a metallic Li anode. Toward this goal, the present study has examined the parameters such as fracture toughness and grain size that could affect the maximum tolerable current density. It was observed that maximum current density was roughly independent of fracture toughness and strongly dependent on grain size. When the grain size increased from 5 µm to 600 µm the critical current density increased from 0.3 to 0.6 mA.cm^{-2}. It is believed that this increase in grain size reduced the grain boundary area and hence, the number of possible failure points leading to an increased CCD (Figure 6.12). These results indicate that further efforts should be focused on the elimination of grain boundaries from the microstructure to suppress Li filament propagations in polycrystalline SSE and allow for improvements of solid-state battery technology.

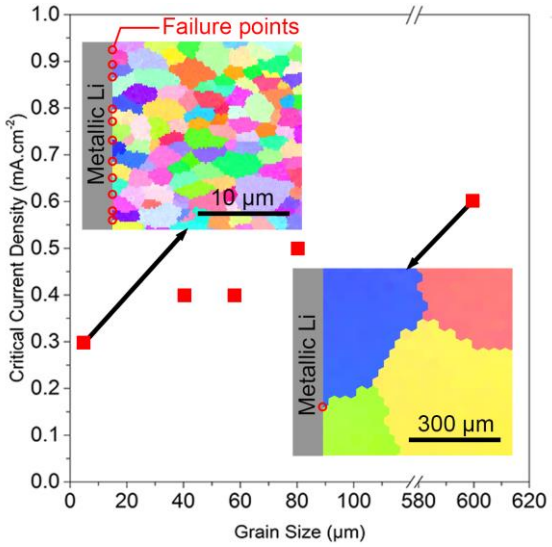

Figure 6.12. The correlation between LLZO grain size and the Li-LLZO stability as a function of Li plating rate is demonstrated. The increase in grain size reduces the grain boundary area and hence the number of possible failure points leading to an increased maximum tolerable current density.

CHAPTER VII

Summary and future work

7.1 Summary

The overall objective of this work was to develop a solid-state electrolyte (SSE) technology based on garnet-type $Li_7La_3Zr_2O_{12}$ (LLZO) to enable the integration of metallic Li anodes into rechargeable batteries. If successful, this work could enable a step increase in energy density and facilitate the transition to electric power trains. The critical steps toward the successful completion of this objective include:

- Determine if LLZO SSE can protect metallic Li anodes
- Develop a fundamental understanding of what governs the critical current density in polycrystalline LLZO
- Establish approaches to maximize the critical current density in polycrystalline LLZO
- Determine if polycrystalline LLZO is relevant to vehicle electrification.

Per our hypothesis, defects will govern the maximum current density in polycrystalline LLZO. To this end, the primary focus of this thesis was to understand the role that defects play in governing the stability and transport through the Li-LLZO interface and quantify the contributions of each defect. This knowledge can be used to develop engineering approaches to tailor the LLZO microstructure and interface for maximum resistance to Li metal propagation.

7.1.1 Stability and transport through the Li-LLZO interface

Comprehensive knowledge of solid-solid interfaces is needed to understand what governs their feasibility in enabling solid-state batteries. The stability and kinetics of the Li-LLZO interface were characterized as a function of temperature and current density (Chapter 3). To this end, polycrystalline LLZO was densified using a rapid hot-pressing technique achieving 97 ± 1% relative density, and <10% grain boundary resistance; effectively consisting of an ensemble of single LLZO crystals. It was demonstrated that temperature and current density significantly affect the Li-LLZO interface kinetics and stability between 30 and 175°C. It was also determined that by heating to 175°C, the room temperature Li-LLZO interface resistance decreases dramatically from 5822 (as-assembled) to 514 $\Omega.cm^2$; a > 10-fold decrease. In characterizing the maximum sustainable current density (or critical current density, CCD) of the Li-LLZO interface, it was shown CCD significantly increases with increasing temperature. For the cells cycled at 30, 70, 100, 130 and 160°C, the CCD was determined to be 0.05, 0.2, 0.8, 3.5, and 20.0 $mA.cm^{-2}$, respectively. The relationship and phenomena observed in this study is useful to better understand the Li-LLZO interface stability to enable the use of batteries employing metallic Li anodes. However, for a SSB to be viable, the stability and charge transfer kinetics at the Li-LLZO interface should foster facile plating and stripping of Li. To compete with conventional Li-ion batteries, the Li-LLZO interfacial resistance should be lower than 10 $\Omega.cm^2$. Contrary to these goals, the initial interfacial resistance in Li-LLZO was much higher (>500 $\Omega.cm^2$) than expected. Previous studies reported high Li-LLZO interfacial resistance is attributed to a contamination layer that forms upon exposure of LLZO to air. Hence, Chapter 4 clarifies the mechanisms and consequences associated with air exposure of LLZO; additionally, strategies to minimize these effects were described. In this chapter, first-principles calculations revealed that

LLZO readily reacts with humid air; the most favorable reaction pathway involves protonation of LLZO and formation of Li_2CO_3. The reaction pathway describing the formation of a contamination layer on LLZO surface proposed by calculations was supported by materials and surface chemistry analysis. X-ray photoelectron spectroscopy (XPS), scanning electron microscopy (SEM), Raman spectroscopy, and transmission electron microscopy (TEM) were used to characterize the surface and subsurface chemistry of LLZO as a function of relative humidity and exposure time. Additionally, electrochemical impedance spectroscopy (EIS) was used to measure the Li-LLZO interfacial resistance as a function of surface contamination. These data indicated that air exposure-induced contamination significantly impacts the interfacial resistance: exposure for 240 h resulted in a resistance increase from 54 $\Omega.cm^2$ (no exposure) to ~37,000 $\Omega.cm^2$. Further calculations indicated the possibility for decomposition of Li_2CO_3 and de-protonation of LLZO at high temperatures. The predicted decomposition temperature for H_2O evolution from LLZO was at approximately 250°C, and de-protonation of LLZO with decomposition of Li_2CO_3 was defined between 400°C and 500°C. Thus, Chapter 5 focused on evaluating a simple procedure for removing these surface layers by heat-treatment between 400°C and 500°C in inert gas. It was shown the interfacial resistance of the LLZO SSE against metallic Li can be reduced to 2 $\Omega.cm^2$ – lower than that of liquid electrolytes – by controlling the surface chemistry of LLZO and without the need for interlayer coatings. A combination of Li contact angle measurements, surface characterization, first-principles calculations, and EIS was used to show that the presence of common LLZO surface contaminants, Li_2CO_3 and LiOH, resulted in poor wettability by Li and high interfacial resistance. Furthermore, the direct current (DC) cycling illustrated the importance of achieving low resistance in solid-state cell designs employing metallic Li anodes. It was shown that decreasing the Li-LLZO interfacial resistance

from hundreds of $\Omega.cm^2$ to less than ten $\Omega.cm^2$ can increases the CCD from 0.05 $mA.cm^{-2}$ to 0.3 $mA.cm^{-2}$, respectively. This demonstrates that controlling surface chemistry and reducing Li-LLZO interfacial resistance is an approach to achieve higher CCD. It was also shown that the low resistance interfacial properties were maintained over one hundred cycles, which suggested a pathway to achieving stable, high energy and power density SSBs.

7.1.2 Stability and transport through LLZO

In the context of SSB technology maturation, the CCD must approach values higher than 1 $mA.cm^{-2}$. Monroe *et al*. proposed that if a SSE has a shear modulus more than a factor of two higher than metallic Li (4.8 GPa), Li filament initiation and propagation should not occur. Thus, LLZO with high shear modulus (60 GPa) was believed to be stable against metallic Li and to suppress initiation and propagation of Li filaments during DC cycling. However, our studies (Chapter 3, 5) and previous studies by other researchers showed that the CCD of LLZO is <1 $mA.cm^{-2}$ in symmetric metallic Li anode cells. To understand this phenomenon, more efforts were focused on understanding the mode of Li filament propagation and engineering the microstructure to suppress Li filament propagation in polycrystalline LLZO. Characterization of short-circuited LLZO in Chapter 3, showed direct evidence of intergranular Li propagation through LLZO grain boundaries. This shows grain boundaries are the defects that primarily control the CCD in polycrystalline LLZO. This finding begged the question "how can the LLZO microstructure be carefully engineered to stabilize the Li-LLZO interface?". In this regard, more efforts were focused on improving the LLZO stability through microstructural engineering of LLZO (Chapter 6). In this chapter, the amount of grain boundary area per unit area of Li-LLZO interface (reduce the number of failure points per unit area) was controlled by growing grains through ceramic processing. It was shown that the average grain size of polycrystalline LLZO

can be increased by increasing the hot-pressing temperature and annealing time. It was also shown that increasing the average grain size from 5 μm to 600 μm, improved the CCD from 0.3 to 0.6 $mA.cm^{-2}$, respectively. However, the presence of grain boundaries, albeit reduced, still acts as initiation points to propagate metallic Li during cycling. To improve the stability of the Li–solid electrolyte interface, future efforts should focus on engineering grain boundaries to suppress Li filament propagation in polycrystalline solid electrolytes.

7.2 Future work

The comprehensive list of material attributes in this thesis has shown LLZO has the potential to enable high energy density Li metal batteries. Based on the results of this thesis, several promising strategies to engineer interface and microstructure of LLZO SSE for SSB applications are proposed.

7.2.1 Interface engineering

Beside removal of contamination from the LLZO surface, the Li-LLZO interface should be free of inhomogeneity. The presence of inhomogeneity at the interface can cause non-uniform Li transport between the metallic Li anode and LLZO, which likely decreases the critical current density. Figure 7.1 shows how the presence of inhomogeneity might cause non-uniform distribution of current density and create hot-spots. Thus, it is important to eliminate the sources of inhomogeneity by interface engineering between Li and LLZO. One strategy can be the use of an interlayer to not only lower the Li-LLZO interfacial resistance but also improve the non-uniform distribution of current density at the interface. Previous studies have shown the use of the interlayer between metallic Li and LLZO can improve interfacial resistance and the uniform distribution of current on the LLZO surface. The interlayer preferably should exhibit the following properties:

- Mixed conduction, e.g. ionically and electronically conducting
- Electrochemically stability at the Li^+/Li^0 redox potential
- Should maintain integrity upon cycling

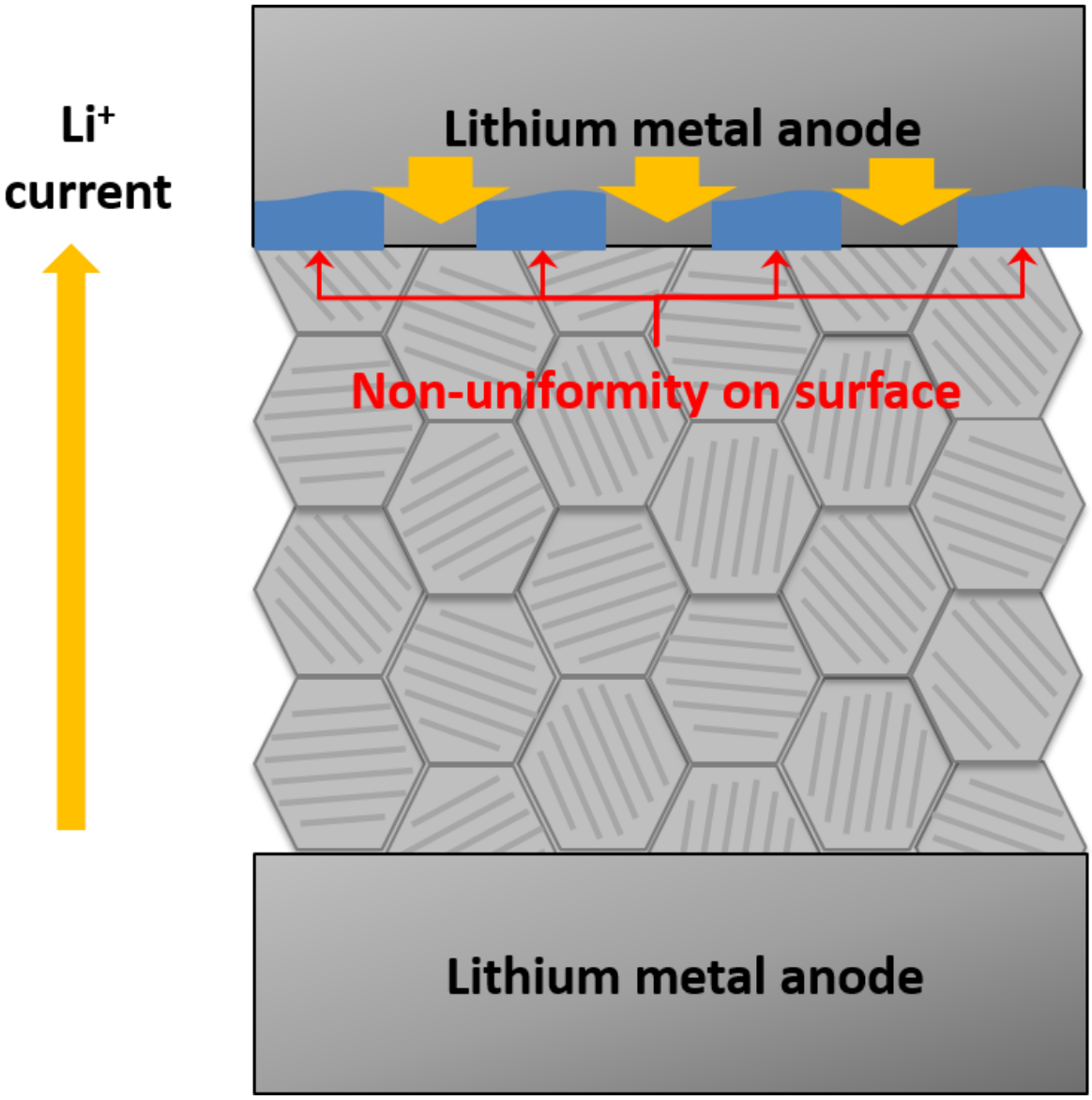

Figure 7.1. Surface non-uniformity may create hot spots and control the current density.

7.2.2 Microstructure engineering

It has been shown that short-circuiting in polycrystalline LLZO arises from penetration of metallic Li along the grain boundary network. Thus, elimination of these failure points from the

microstructure is a possible strategy to make LLZO a viable SSE. To this end, two approaches are proposed:

I) Elimination of grain boundaries from the microstructure by moving toward single crystal LLZO. The single crystalline LLZO can be achieved by longer hold times at higher temperature during hot-pressing and annealing. It should be noted that the failure mode in single crystalline might change, thus more effort should be focused on the evaluation of CCD and factors controlling the CCD in single crystalline LLZO. As an alternative, if single crystal LLZO cannot be fabricated, polycrystalline LLZO with relatively large grains can be used. To evaluate the LLZO stability against metallic Li in the absence of grain boundaries, the LLZO microstructure can be masked as shown schematically in Figure 7.2. The use of a mask would isolate a single grain and would enable CCD measurement in the absence of grain boundaries.

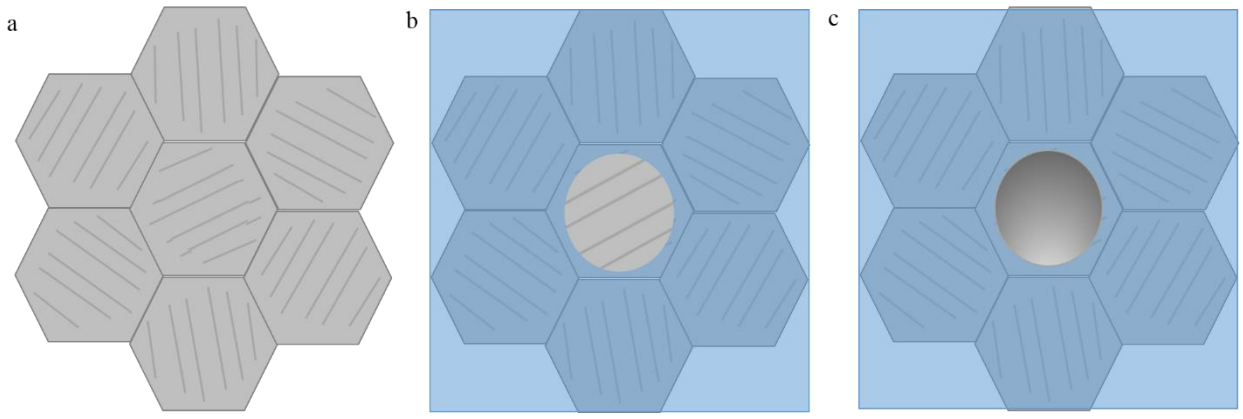

Figure 7.2. a) Schematic of LLZO microstructure with relatively large grain size, b) isolation of a single grain using a mask, c) metallic Li on masked LLZO to evaluate CCD.

II) Microstructural engineering of LLZO in which grain boundaries contain another phase that would suppress the propagation of the metallic Li during cycling (Figure 7.3). The grain boundary modification should make the grain boundaries electrical insulators. The modified grain boundaries preferably should exhibit the following properties:

- May or may not be ionically conducting
- Not soluble in the LLZO grains, such that any chemical modification of the grain boundary, remains at the grain boundary during high temperature processing

- Electrochemically stable at the Li^+/Li^0 redox potential

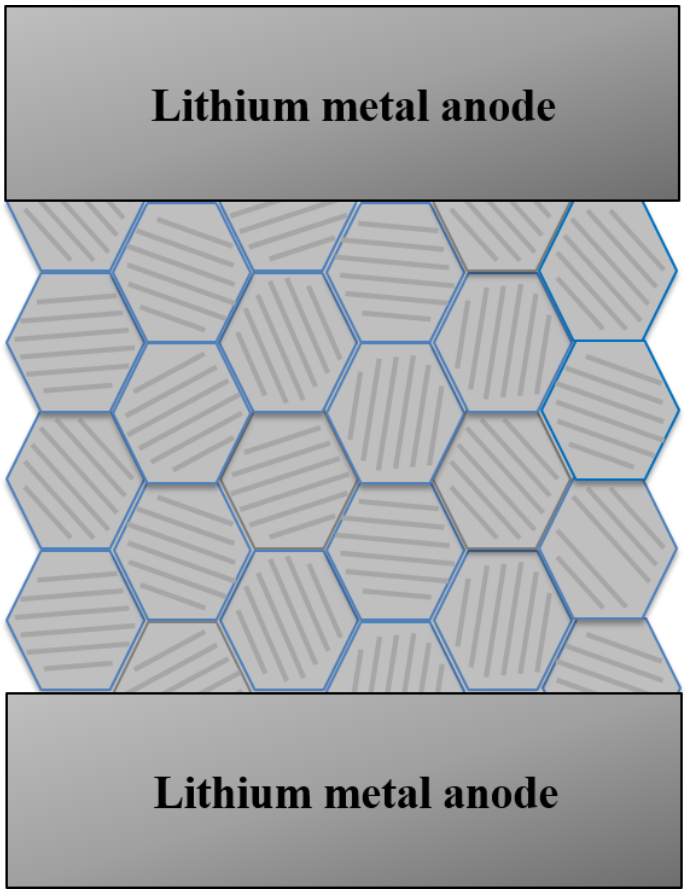

Figure 7.3. Schematic of polycrystalline LLZO with chemically modified grain boundaries.

BIBILOGRAPHY

1. Armand, M.; Tarascon, J.-M., Building better batteries. *Nature* **2008,** *451* (7179), 652-657.

2. Asif, M.; Muneer, T., Energy supply, its demand and security issues for developed and emerging economies. *Renewable and Sustainable Energy Reviews* **2007,** *11* (7), 1388-1413.

3. Agency, I. E., CO2 emissions from fuel combustion highlights. *International Energy Agency: Paris, France* **2015**.

4. Trigg, T.; Telleen, P.; Boyd, R.; Cuenot, F.; D'Ambrosio, D.; Gaghen, R.; Gagné, J.; Hardcastle, A.; Houssin, D.; Jones, A., Global EV outlook: Understanding the electric vehicle landscape to 2020. *Int. Energy Agency* **2013**, 1-40.

5. Dunn, B.; Kamath, H.; Tarascon, J.-M., Electrical Energy Storage for the Grid: A Battery of Choices. *Science* **2011,** *334* (6058), 928-935.

6. Wachsman, E. D.; Marlowe, C. A.; Lee, K. T., Role of solid oxide fuel cells in a balanced energy strategy. *Energy & Environmental Science* **2012,** *5* (2), 5498-5509.

7. Abraham, K. M., Exploding Hoverboards Explained (and other lithium-ion battery devices). *The electrochemcial society* **2016**.

8. Van Noorden, R., A better battery. *Nature* **2014,** *507* (7490), 26-28.

9. Nykvist, B.; Nilsson, M., Rapidly falling costs of battery packs for electric vehicles. *Nature Climate Change* **2015,** *5* (4), 329-332.

10. Howell, D.; Cunningham, B.; Duong, T.; Faguy, P., Overview of the DOE VTO Advanced Battery R&D Program. *Annual Merit Review June* **2016,** *6*.

11. Bruce, P. G.; Freunberger, S. A.; Hardwick, L. J.; Tarascon, J.-M., Li-O_2 and Li-S batteries with high energy storage. *Nat Mater* **2012,** *11* (1), 19-29.

12. Bruce, P. G.; Hardwick, L. J.; Abraham, K., Lithium-air and lithium-sulfur batteries. *MRS bulletin* **2011,** *36* (07), 506-512.

13. Xu, Q.; Li, J. Y.; Sun, J. K.; Yin, Y. X.; Wan, L. J.; Guo, Y. G., Watermelon-Inspired Si/C Microspheres with Hierarchical Buffer Structures for Densely Compacted Lithium-Ion Battery Anodes. *Advanced Energy Materials* **2017,** *7* (3).

14. Yu, Z.-L.; Xin, S.; You, Y.; Yu, L.; Lin, Y.; Xu, D.-W.; Qiao, C.; Huang, Z.-H.; Yang, N.; Yu, S.-H., Ion-catalyzed synthesis of microporous hard carbon embedded with expanded nanographite for enhanced lithium/sodium storage. *J. Am. Chem. Soc* **2016,** *138* (45), 14915-14922.

15. Li, N. W.; Yin, Y. X.; Yang, C. P.; Guo, Y. G., An artificial solid electrolyte interphase layer for stable lithium metal anodes. *Advanced Materials* **2016,** *28* (9), 1853-1858.

16. Li, N. W.; Yin, Y. X.; Li, J. Y.; Zhang, C. H.; Guo, Y. G., Passivation of Lithium Metal Anode via Hybrid Ionic Liquid Electrolyte toward Stable Li Plating/Stripping. *Advanced Science* **2017,** *4* (2).

17. Yang, C.-P.; Yin, Y.-X.; Zhang, S.-F.; Li, N.-W.; Guo, Y.-G., Accommodating lithium into 3D current collectors with a submicron skeleton towards long-life lithium metal anodes. *Nature communications* **2015,** *6*, 8058.

18. Xu, Q.; Li, J. Y.; Yin, Y. X.; Kong, Y. M.; Guo, Y. G.; Wan, L. J., Nano/Micro-Structured Si/C Anodes with High Initial Coulombic Efficiency in Li-Ion Batteries. *Chemistry–An Asian Journal* **2016,** *11* (8), 1205-1209.

19. Zhou, X.; Yin, Y. X.; Wan, L. J.; Guo, Y. G., Self-assembled nanocomposite of silicon nanoparticles encapsulated in graphene through electrostatic attraction for lithium-ion batteries. *Advanced Energy Materials* **2012,** *2* (9), 1086-1090.

20. Xue, D.-J.; Xin, S.; Yan, Y.; Jiang, K.-C.; Yin, Y.-X.; Guo, Y.-G.; Wan, L.-J., Improving the electrode performance of Ge through Ge@ C core–shell nanoparticles and graphene networks. *Journal of the American Chemical Society* **2012,** *134* (5), 2512-2515.

21. Huggins, R., *Advanced batteries: materials science aspects*. Springer Science & Business Media: 2008.

22. Xu, W.; Wang, J.; Ding, F.; Chen, X.; Nasybulin, E.; Zhang, Y.; Zhang, J.-G., Lithium metal anodes for rechargeable batteries. *Energy & Environmental Science* **2014,** *7* (2), 513-537.

23. Tarascon, J.-M.; Armand, M., Issues and challenges facing rechargeable lithium batteries. *Nature* **2001,** *414* (6861), 359-367.

24. Ohsaki, T.; Kishi, T.; Kuboki, T.; Takami, N.; Shimura, N.; Sato, Y.; Sekino, M.; Satoh, A., Overcharge reaction of lithium-ion batteries. *Journal of Power Sources* **2005,** *146* (1), 97-100.

25. Liu, Y.-H.; Hsieh, C.-H.; Luo, Y.-F., Search for an optimal five-step charging pattern for Li-ion batteries using consecutive orthogonal arrays. *IEEE Transactions on Energy Conversion* **2011,** *26* (2), 654-661.

26. Knauth, P., Inorganic solid Li ion conductors: An overview. *Solid State Ionics* **2009,** *180* (14–16), 911-916.

27. Adachi, G.-y.; Imanaka, N.; Aono, H., Fast Li⊕ Conducting Ceramic Electrolytes. *Advanced Materials* **1996,** *8* (2), 127-135.

28. Bates, J.; Dudney, N.; Lubben, D.; Gruzalski, G.; Kwak, B.; Yu, X.; Zuhr, R., Thin-film rechargeable lithium batteries. *Journal of Power Sources* **1995,** *54* (1), 58-62.

29. Bates, J.; Dudney, N.; Gruzalski, G.; Zuhr, R.; Choudhury, A.; Luck, C.; Robertson, J., Electrical properties of amorphous lithium electrolyte thin films. *Solid state ionics* **1992,** *53*, 647-654.

30. Dudney, N. J., Solid-state thin-film rechargeable batteries. *Materials Science and Engineering: B* **2005,** *116* (3), 245-249.

31. Mizuno, F.; Hayashi, A.; Tadanaga, K.; Tatsumisago, M., High lithium ion conducting glass-ceramics in the system Li 2 S–P 2 S 5. *Solid State Ionics* **2006,** *177* (26), 2721-2725.

32. Nazri, G.-A.; Pistoia, G., *Lithium batteries: science and technology*. Springer Science & Business Media: 2008.

33. Levasseur, A.; Brethous, J.; Reau, J.; Hagenmuller, P.; Couzi, M., Synthesis and characterization of new solid electrolyte conductors of lithium ions. *Solid State Ionics* **1980,** *1* (3-4), 177-186.

34. Saienga, J.; Martin, S. W., The comparative structure, properties, and ionic conductivity of LiI+ Li_2S+ GeS_2 glasses doped with Ga_2S_3 and La_2S_3. *Journal of Non-Crystalline Solids* **2008,** *354* (14), 1475-1486.

35. Belous, A., Study of complex oxides with the composition $La_{2/3-X}Li_{3X}TiO_3$. *INORG. MATER. Inorg. Mater.* **1987,** *23* (3), 412.

36. Latie, L.; Villeneuve, G.; Conte, D.; Le Flem, G., Ionic conductivity of oxides with general formula $Li_xLn_{1/3}Nb_{1-x}Ti_xO_3$ (Ln = La, Nd). *Journal of Solid State Chemistry* **1984,** *51* (3), 293-299.

37. Hagman, L. O.; Kierkegaard, P., The crystal structure of $NaMe_2IV(PO_4)_3$; Me IV= Ge, Ti, Zr. *Acta Chem. Scand* **1968,** *22* (6).

38. Xie, H.; Li, Y.; Goodenough, J. B., NASICON-type $Li_{1+2x}Zr_{2-x}Ca_x(PO_4)_3$ with high ionic conductivity at room temperature. *RSC Advances* **2011,** *1* (9), 1728-1731.

39. Goodenough, J.; Hong, H.-P.; Kafalas, J., Fast Na+-ion transport in skeleton structures. *Materials Research Bulletin* **1976,** *11* (2), 203-220.

40. Aono, H.; Sugimoto, E.; Sadaoka, Y.; Imanaka, N.; Adachi, G.-y., Electrical property and sinterability of $LiTi_2(PO_4)_3$mixed with lithium salt (Li_3PO_4 or Li_3BO_3. *Solid State Ionics* **1991,** *47* (3), 257-264.

41. Hong, H.-P., Crystal structures and crystal chemistry in the system $Na_{1+x}Zr_2Si_xP_{3-x}O_{12}$. *Materials Research Bulletin* **1976,** *11* (2), 173-182.

42. Murayama, M.; Kanno, R.; Irie, M.; Ito, S.; Hata, T.; Sonoyama, N.; Kawamoto, Y., Synthesis of new lithium ionic conductor thio-LISICON—lithium silicon sulfides system. *Journal of Solid State Chemistry* **2002,** *168* (1), 140-148.

43. Bruce, P. G.; West, A., The A-C Conductivity of Polycrystalline LISICON, $Li_{2+2x}Zn_{1-x}GeO_4$, and a Model for Intergranular Constriction Resistances. *Journal of The Electrochemical Society* **1983,** *130* (3), 662-669.

44. Hyooma, H.; Hayashi, K., Crystal structures of $La_3Li_5M_2O_{12}$ (M= Nb, Ta). *Materials Research Bulletin* **1988,** *23* (10), 1399-1407.

45. Thangadurai, V.; Kaack, H.; Weppner, W. J., Novel Fast Lithium Ion Conduction in Garnet-Type $Li_5La_3M_2O_{12}$ (M= Nb, Ta). *Journal of the American Ceramic Society* **2003,** *86* (3), 437-440.

46. Murugan, R.; Thangadurai, V.; Weppner, W., Fast Lithium Ion Conduction in Garnet-Type $Li_7La_3Zr_2O_{12}$. *Angewandte Chemie International Edition* **2007,** *46* (41), 7778-7781.

47. Awaka, J.; Takashima, A.; Kataoka, K.; Kijima, N.; Idemoto, Y.; Akimoto, J., Crystal Structure of Fast Lithium-ion-conducting Cubic $Li_7La_3Zr_2O_{12}$. *Chemistry Letters* **2011,** *40* (1), 60-62.

48. Shimonishi, Y.; Toda, A.; Zhang, T.; Hirano, A.; Imanishi, N.; Yamamoto, O.; Takeda, Y., Synthesis of garnet-type $Li_7La_3Zr_2O_{12}$ and its stability in aqueous solutions. *Solid State Ionics* **2011,** *183* (1), 48-53.

49. Awaka, J.; Kijima, N.; Kataoka, K.; Hayakawa, H.; Ohshima, K.-i.; Akimoto, J., Neutron powder diffraction study of tetragonal $Li_7La_3Hf_2O_{12}$ with the garnet-related type structure. *Journal of Solid State Chemistry* **2010,** *183* (1), 180-185.

50. Rangasamy, E.; Wolfenstine, J.; Sakamoto, J., The role of Al and Li concentration on the formation of cubic garnet solid electrolyte of nominal composition $Li_7La_3Zr_2O_{12}$. *Solid State Ionics* **2012,** *206* (0), 28-32.

51. Thompson, T.; Yu, S.; Williams, L.; Schmidt, R. D.; Garcia-Mendez, R.; Wolfenstine, J.; Allen, J. L.; Kioupakis, E.; Siegel, D. J.; Sakamoto, J., Electrochemical Window of the Li-Ion Solid Electrolyte $Li_7La_3Zr_2O_{12}$. *ACS Energy Letters* **2017,** *2* (2), 462-468.

52. Monroe, C.; Newman, J., The impact of elastic deformation on deposition kinetics at lithium/polymer interfaces. *Journal of The Electrochemical Society* **2005,** *152* (2), A396-A404.

53. Ni, J. E.; Case, E. D.; Sakamoto, J. S.; Rangasamy, E.; Wolfenstine, J. B., Room temperature elastic moduli and Vickers hardness of hot-pressed LLZO cubic garnet. *Journal of Materials Science* **2012,** *47* (23), 7978-7985.

54. Yu, S.; Schmidt, R. D.; Garcia-Mendez, R.; Herbert, E.; Dudney, N. J.; Wolfenstine, J. B.; Sakamoto, J.; Siegel, D. J., Elastic Properties of the Solid Electrolyte $Li_7La_3Zr_2O_{12}$ (LLZO). *Chemistry of Materials* **2015,** *28* (1), 197-206.

55. Meyer, W. H., Polymer electrolytes for lithium-ion batteries. *Advanced materials* **1998,** *10* (6), 439-448.

56. Hagman, L.-O.; Kierkegaard, P.; Karvonen, P.; Virtanen, A. I.; Paasivirta, J., The crystal structure of $NaMe_2{}^{IV}(PO_4)_3$; MeIV= Ge, Ti, Zr. *Acta Chem. Scand* **1968,** *22* (6), 1822-32.

57. Buschmann, H.; Dölle, J.; Berendts, S.; Kuhn, A.; Bottke, P.; Wilkening, M.; Heitjans, P.; Senyshyn, A.; Ehrenberg, H.; Lotnyk, A., Structure and dynamics of the fast lithium ion conductor "$Li_7La_3Zr_2O_{12}$". *Physical Chemistry Chemical Physics* **2011,** *13* (43), 19378-19392.

58. Ohta, S.; Kobayashi, T.; Asaoka, T., High lithium ionic conductivity in the garnet-type oxide $Li_{7-X}La_3(Zr_{2-X},Nb_X)O_{12}$ *Journal of Power Sources* **2011,** *196* (6), 3342-3345.

59. Sudo, R.; Nakata, Y.; Ishiguro, K.; Matsui, M.; Hirano, A.; Takeda, Y.; Yamamoto, O.; Imanishi, N., Interface behavior between garnet-type lithium-conducting solid electrolyte and lithium metal. *Solid State Ionics* **2014,** *262*, 151-154.

60. Ohta, S.; Kobayashi, T.; Seki, J.; Asaoka, T., Electrochemical performance of an all-solid-state lithium ion battery with garnet-type oxide electrolyte. *Journal of Power Sources* **2012,** *202* (0), 332-335.

61. Ren, Y.; Shen, Y.; Lin, Y.; Nan, C.-W., Direct observation of lithium dendrites inside garnet-type lithium-ion solid electrolyte. *Electrochemistry Communications* **2015,** *57*, 27-30.

62. Ishiguro, K.; Nakata, Y.; Matsui, M.; Uechi, I.; Takeda, Y.; Yamamoto, O.; Imanishi, N., Stability of Nb-Doped Cubic $Li_7La_3Zr_2O_{12}$ with Lithium Metal. *Journal of The Electrochemical Society* **2013,** *160* (10), A1690-A1693.

63. Ishiguro, K.; Nemori, H.; Sunahiro, S.; Nakata, Y.; Sudo, R.; Matsui, M.; Takeda, Y.; Yamamoto, O.; Imanishi, N., Ta-Doped $Li_7La_3Zr_2O_{12}$ for Water-Stable Lithium Electrode of Lithium-Air Batteries. *Journal of The Electrochemical Society* **2014,** *161* (5), A668-A674.

64. Awaka, J.; Kijima, N.; Hayakawa, H.; Akimoto, J., Synthesis and structure analysis of tetragonal $Li_7La_3Zr_2O_{12}$ with the garnet-related type structure. *Journal of Solid State Chemistry* **2009,** *182* (8), 2046-2052.

65. Shimonishi, Y.; Toda, A.; Zhang, T.; Hirano, A.; Imanishi, N.; Yamamoto, O.; Takeda, Y., Synthesis of garnet-type $Li_{7-x}La_3Zr_2O_{12-1/2x}$ and its stability in aqueous solutions. *Solid State Ionics* **2011,** *183* (1), 48-53.

66. Wolfenstine, J.; Rangasamy, E.; Allen, J. L.; Sakamoto, J., High conductivity of dense tetragonal $Li_7La_3Zr_2O_{12}$. *Journal of Power Sources* **2012,** *208*, 193-196.

67. Geiger, C. A.; Alekseev, E.; Lazic, B.; Fisch, M.; Armbruster, T.; Langner, R.; Fechtelkord, M.; Kim, N.; Pettke, T.; Weppner, W., Crystal Chemistry and Stability of "$Li_7La_3Zr_2O_{12}$" Garnet: A Fast Lithium-Ion Conductor. *Inorganic Chemistry* **2011,** *50* (3), 1089-1097.

68. Nozaki, H.; Harada, M.; Ohta, S.; Jalarvo, N. H.; Mamontov, E.; Watanabe, I.; Miyake, Y.; Ikedo, Y.; Sugiyama, J., Diffusive Behavior of Li Ions in Garnet $Li_{5+x}La_3Zr_xNb_{2-x}O_{12}$ (x = 0–2). *Journal of the Physical Society of Japan* **2013,** *82* (Suppl.A), SA004.

69. Kihira, Y.; Ohta, S.; Imagawa, H.; Asaoka, T., Effect of Simultaneous Substitution of Alkali Earth Metals and Nb in $Li_7La_3Zr_2O_{12}$ on Lithium-Ion Conductivity. *ECS Electrochemistry Letters* **2013,** *2* (7), A56-A59.

70. Bernstein, N.; Johannes, M.; Hoang, K., Origin of the structural phase transition in $Li_7La_3Zr_2O_{12}$. *Physical review letters* **2012,** *109* (20), 205702.

71. David, I. N.; Thompson, T.; Wolfenstine, J.; Allen, J. L.; Sakamoto, J., Microstructure and Li-ion conductivity of hot-pressed cubic $Li_7La_3Zr_2O_{12}$. *Journal of the American Ceramic Society* **2015,** *98* (4), 1209-1214.

72. Huggins, R., Simple method to determine electronic and ionic components of the conductivity in mixed conductors a review. *Ionics* **2002,** *8* (3-4), 300-313.

73. Irvine, J. T.; Sinclair, D. C.; West, A. R., Electroceramics: characterization by impedance spectroscopy. *Advanced Materials* **1990,** *2* (3), 132-138.

74. Cheng, L.; Park, J. S.; Hou, H.; Zorba, V.; Chen, G.; Richardson, T.; Cabana, J.; Russo, R.; Doeff, M., Effect of microstructure and surface impurity segregation on the electrical and electrochemical properties of dense Al-substituted $Li_7La_3Zr_2O_{12}$. *Journal of Materials Chemistry A* **2014,** *2* (1), 172-181.

75. Goodenough, J. B.; Kim, Y., Challenges for rechargeable Li batteries†. *Chemistry of Materials* **2010,** *22* (3), 587-603.

76. Wolfenstine, J.; Allen, J.; Read, J.; Sakamoto, J., Chemical stability of cubic $Li_7La_3Zr_2O_{12}$ with molten lithium at elevated temperature. *Journal of Materials Science* **2013,** *48* (17), 5846-5851.

77. Samsonov, G. V., *Handbook of the physicochemical properties of the elements*. Springer Science & Business Media: 2012.

78. Kotobuki, M.; Suzuki, Y.; Munakata, H.; Kanamura, K.; Sato, Y.; Yamamoto, K.; Yoshida, T., Fabrication of three-dimensional battery using ceramic electrolyte with honeycomb structure by sol–gel process. *Journal of The Electrochemical Society* **2010,** *157* (4), A493-A498.

79. Gibson, A., Power Sources ed. Collins DH Ch. 6Academic Press: 1977.

80. Viswanathan, L.; Virkar, A. V., Wetting characteristics of sodium on β ″-alumina and on nasicon. *Journal of Materials Science* **1982,** *17* (3), 753-759.

81. Virkar, A. V.; Viswanathan, L.; Biswas, D. R., On the deterioration of ß ″-alumina ceramics under electrolytic conditions. *Journal of Materials Science* **1980,** *15* (2), 302-308.

82. Lu, X.; Li, G.; Kim, J. Y.; Mei, D.; Lemmon, J. P.; Sprenkle, V. L.; Liu, J., Liquid-metal electrode to enable ultra-low temperature sodium–beta alumina batteries for renewable energy storage. *Nat Commun* **2014,** *5*.

83. Tenhaeff, W. E.; Rangasamy, E.; Wang, Y.; Sokolov, A. P.; Wolfenstine, J.; Sakamoto, J.; Dudney, N. J., Resolving the Grain Boundary and Lattice Impedance of Hot-Pressed $Li_7La_3Zr_2O_{12}$ Garnet Electrolytes. *ChemElectroChem* **2014,** *1* (2), 375-378.

84. Zhang, S. S.; Xu, K.; Jow, T. R., The low temperature performance of Li-ion batteries. *Journal of Power Sources* **2003,** *115* (1), 137-140.

85. Virkar, A. V.; Miller, G. R., Degradation of rapid ion conductors under electrolytic conditions. **1979**.

86. Zhang, S.; Ding, M. S.; Xu, K.; Allen, J.; Jow, T. R., Understanding solid electrolyte interface film formation on graphite electrodes. *Electrochemical and Solid-State Letters* **2001,** *4* (12), A206-A208.

87. Liu, P.; Wang, J.; Hicks-Garner, J.; Sherman, E.; Soukiazian, S.; Verbrugge, M.; Tataria, H.; Musser, J.; Finamore, P., Aging mechanisms of $LiFePO_4$ batteries deduced by electrochemical and structural analyses. *Journal of the Electrochemical Society* **2010,** *157* (4), A499-A507.

88. Aurbach, D., Review of selected electrode–solution interactions which determine the performance of Li and Li ion batteries. *Journal of Power Sources* **2000,** *89* (2), 206-218.

89. Broussely, M.; Biensan, P.; Bonhomme, F.; Blanchard, P.; Herreyre, S.; Nechev, K.; Staniewicz, R., Main aging mechanisms in Li ion batteries. *Journal of power sources* **2005,** *146* (1), 90-96.

90. Zhang, S.; Xu, K.; Jow, T., Electrochemical impedance study on the low temperature of Li-ion batteries. *Electrochimica acta* **2004,** *49* (7), 1057-1061.

91. Cheng, L.; Crumlin, E. J.; Chen, W.; Qiao, R.; Hou, H.; Lux, S. F.; Zorba, V.; Russo, R.; Kostecki, R.; Liu, Z., The origin of high electrolyte–electrode interfacial resistances in lithium cells containing garnet type solid electrolytes. *Physical Chemistry Chemical Physics* **2014,** *16* (34), 18294-18300.

92. Galven, C.; Dittmer, J.; Suard, E.; Le Berre, F. o.; Crosnier-Lopez, M.-P., Instability of Lithium Garnets against Moisture. Structural Characterization and Dynamics of $Li_{7-x}H_xLa_3Sn_2O_{12}$ and $Li_{5-x}H_xLa_3Nb_2O_{12}$. *Chemistry of Materials* **2012,** *24* (17), 3335-3345.

93. Toda, S.; Ishiguro, K.; Shimonishi, Y.; Hirano, A.; Takeda, Y.; Yamamoto, O.; Imanishi, N., Low temperature cubic garnet-type CO_2-doped $Li_7La_3Zr_2O_{12}$. *Solid State Ionics* **2013,** *233* (0), 102-106.

94. Xia, W.; Xu, B.; Duan, H.; Guo, Y.; Kang, H.; Li, H.; Liu, H., Ionic conductivity and air stability of Al-doped $Li_7La_3Zr_2O_{12}$ sintered in alumina and Pt crucibles. *Acs Applied Materials & Interfaces* **2016,** *8* (8), 5335-5342.

95. Jin, Y.; McGinn, P. J., $Li_7La_3Zr_2O_{12}$ electrolyte stability in air and fabrication of a $Li/Li_7La_3Zr_2O_{12}/Cu_{0.1}V_2O_5$ solid-state battery. *Journal of Power Sources* **2013,** *239* (0), 326-331.

96. Larraz, G.; Orera, A.; Sanjuan, M., Cubic phases of garnet-type $Li_7La_3Zr_2O_{12}$: the role of hydration. *Journal of Materials Chemistry A* **2013,** *1* (37), 11419-11428.

97. Cheng, L.; Wu, C. H.; Jarry, A.; Chen, W.; Ye, Y.; Zhu, J.; Kostecki, R.; Persson, K.; Guo, J.; Salmeron, M., Interrelationships among grain size, surface composition, air stability, and interfacial resistance of Al-substituted $Li_7La_3Zr_2O_{12}$ solid electrolytes. *Acs Applied Materials & Interfaces* **2015,** *7* (32), 17649-17655.

98. Yow, Z. F.; Oh, Y. L.; Gu, W.; Rao, R. P.; Adams, S., Effect of Li^+/H^+ exchange in water treated Ta-doped $Li_7La_3Zr_2O_{12}$. *Solid State Ionics* **2016,** *292*, 122-129.

99. Kresse, G.; Furthmüller, J., Efficient iterative schemes for ab initio total-energy calculations using a plane-wave basis set. *Physical Review B* **1996,** *54* (16), 11169-111186.

100. Blöchl, P. E., Projector augmented-wave method. *Physical Review B* **1994,** *50* (24), 17953.

101. Kresse, G.; Joubert, D., From ultrasoft pseudopotentials to the projector augmented-wave method. *Physical Review B* **1999,** *59* (3), 1758-1775.

102. Perdew, J. P.; Burke, K.; Ernzerhof, M., Generalized gradient approximation made simple. *Physical review letters* **1996,** *77* (18), 3865-3868.

103. Ma, C.; Rangasamy, E.; Liang, C.; Sakamoto, J.; More, K. L.; Chi, M., Excellent Stability of a Lithium-Ion-Conducting Solid Electrolyte upon Reversible Li^+/H^+ Exchange in Aqueous Solutions. *Angewandte Chemie* **2015,** *127* (1), 131-135.

104. Larraz, G.; Orera, A.; Sanz, J.; Sobrados, I.; Diez-Gómez, V.; Sanjuan, M., NMR study of Li distribution in $Li_{7-x}H_xLa_3Zr_2O_{12}$ garnets. *Journal of Materials Chemistry A* **2015,** *3* (10), 5683-5691.

105. Monkhorst, H. J.; Pack, J. D., Special points for Brillouin-zone integrations. *Physical Review B* **1976,** *13* (12), 5188-5193.

106. Murnaghan, F., The compressibility of media under extreme pressures. *Proceedings of the National Academy of Sciences* **1944,** *30* (9), 244-247.

107. Chase, M. W., JANAF thermochemical tables. *JANAF thermochemical tables, by Chase, MW Washington, DC: American Chemical Society; New York: American Institute of Physics for the National Bureau of Standards, c1986.. United States. National Bureau of Standards.* **1986,** *1*.

108. Marsh, K. N., *Recommended reference materials for the realization of physicochemical properties*. Blackwell Scientific Publications: 1987.

109. Boulant, A.; Bardeau, J. F.; Jouanneaux, A.; Emery, J.; Buzare, J.-Y.; Bohnke, O., Reaction mechanisms of $Li_{0.30}La_{0.57}TiO_3$ powder with ambient air: H^+/Li^+ exchange with water and Li_2CO_3 formation. *Dalton Transactions* **2010,** *39* (16), 3968-3975.

110. Thompson, T.; Wolfenstine, J.; Allen, J. L.; Johannes, M. D.; Huq, A.; David, I. N.; Sakamoto, J., Tetragonal vs. cubic phase stability in Al–free Ta doped $Li_7La_3Zr_2O_{12}$ (LLZO). *Journal of Materials Chemistry A* **2014**.

111. Mukhopadhyay, S.; Thompson, T.; Sakamoto, J.; Huq, A.; Wolfenstine, J.; Allen, J. L.; Bernstein, N.; Stewart, D. A.; Johannes, M., Structure and stoichiometry in supervalent doped $Li_7La_3Zr_2O_{12}$. *Chemistry of Materials* **2015,** *27* (10), 3658-3665.

112. Tietz, F.; Wegener, T.; Gerhards, M.; Giarola, M.; Mariotto, G., Synthesis and Raman micro-spectroscopy investigation of $Li_7La_3Zr_2O_{12}$. *Solid State Ionics* **2013,** *230*, 77-82.

113. Tsuji, J.; Nakamatsu, H.; Mukoyama, T.; Kojima, K.; Ikeda, S.; Taniguchi, K., Lithium K-edge XANES spectra for lithium compounds. *X-Ray Spectrometry* **2002,** *31* (4), 319-326.

114. Thompson, T.; Sharafi, A.; Johannes, M. D.; Huq, A.; Allen, J. L.; Wolfenstine, J.; Sakamoto, J., A Tale of Two Sites: On Defining the Carrier Concentration in Garnet-Based Ionic Conductors for Advanced Li Batteries. *Advanced Energy Materials* **2015**.

115. Sharafi, A.; Meyer, H. M.; Nanda, J.; Wolfenstine, J.; Sakamoto, J., Characterizing the Li–$Li_7La_3Zr_2O_{12}$ interface stability and kinetics as a function of temperature and current density. *Journal of Power Sources* **2016,** *302*, 135-139.

116. Kim, Y.; Yoo, A.; Schmidt, R.; Sharafi, A.; Lee, H.; Wolfenstine, J.; Sakamoto, J., Electrochemical Stability of $Li_{6.5}La_3Zr_{1.5}M_{0.5}O_{12}$ (M= Nb or Ta) against Metallic Lithium. *Frontiers in Energy Research* **2016,** *4*, 20.

117. Zhang, S.; Xu, K.; Jow, T., The low temperature performance of Li-ion batteries. *Journal of Power Sources* **2003,** *115* (1), 137-140.

118. Tsai, C.-L.; Roddatis, V.; Chandran, C. V.; Ma, Q.; Uhlenbruck, S.; Bram, M.; Heitjans, P.; Guillon, O., $Li_7La_3Zr_2O_{12}$ interface modification for Li dendrite prevention. *ACS applied materials & interfaces* **2016,** *8* (16), 10617-10626.

119. Barocas, D. A.; Liu, A.; Burks, F. N.; Suh, R. S.; Schuster, T. G.; Bradford, T.; Moylan, D. A.; Knapp, P. M.; Murtagh, D. S.; Morris, D.; Dunn, R. L.; Montie, J. E.; Miller, D. C., Practice Based Collaboration to Improve the Use of Immediate Intravesical Therapy after Resection of Nonmuscle Invasive Bladder Cancer. *Journal of Urology* **2013,** *190* (6), 2011-2016.

120. Han, X.; Gong, Y.; Fu, K. K.; He, X.; Hitz, G. T.; Dai, J.; Pearse, A.; Liu, B.; Wang, H.; Rubloff, G.; Mo, Y.; Thangadurai, V.; Wachsman, E. D.; Hu, L., Negating interfacial impedance in garnet-based solid-state Li metal batteries. *Nature materials* **2017,** *16* (5), 572-579.

121. Dupin, J.-C.; Gonbeau, D.; Vinatier, P.; Levasseur, A., Systematic XPS studies of metal oxides, hydroxides and peroxides. *Physical Chemistry Chemical Physics* **2000,** *2* (6), 1319-1324.

122. Yao, K. P.; Kwabi, D. G.; Quinlan, R. A.; Mansour, A. N.; Grimaud, A.; Lee, Y.-L.; Lu, Y.-C.; Shao-Horn, Y., Thermal stability of Li_2O_2 and Li_2O for Li-air batteries: In situ XRD and XPS studies. *Journal of The Electrochemical Society* **2013,** *160* (6), A824-A831.

123. Huang, M.; Liu, T.; Deng, Y.; Geng, H.; Shen, Y.; Lin, Y.; Nan, C.-W., Effect of sintering temperature on structure and ionic conductivity of $Li_{7-x}La_3Zr_2O_{12-0.5x}$ (x= 0.5~ 0.7) ceramics. *Solid State Ionics* **2011,** *204*, 41-45.

124. Jena, R. K.; Yue, C. Y., Cyclic olefin copolymer based microfluidic devices for biochip applications: Ultraviolet surface grafting using 2-methacryloyloxyethyl phosphorylcholine. *Biomicrofluidics* **2012,** *6* (1), 012822.

125. Lee, K.; Murray, É. D.; Kong, L.; Lundqvist, B. I.; Langreth, D. C., Higher-accuracy van der Waals density functional. *Physical Review B* **2010,** *82* (8), 081101-1-081101-4.

126. Smith, J. R.; Hong, T.; Srolovitz, D. J., Metal-ceramic adhesion and the Harris functional. *Physical review letters* **1994,** *72* (25), 4021-4024.

127. Cheng, E. J.; Sharafi, A.; Sakamoto, J., Intergranular Li metal propagation through polycrystalline $Li_{6.25}Al_{0.25}La_3Zr_2O_{12}$ ceramic electrolyte. *Electrochimica Acta* **2017,** *223*, 85-91.

128. Beyer, H.; Meini, S.; Tsiouvaras, N.; Piana, M.; Gasteiger, H., Thermal and electrochemical decomposition of lithium peroxide in non-catalyzed carbon cathodes for Li–air batteries. *Physical Chemistry Chemical Physics* **2013,** *15* (26), 11025-11037.

129. Kanamura, K.; Tamura, H.; Takehara, Z.-i., XPS analysis of a lithium surface immersed in propylene carbonate solution containing various salts. *Journal of Electroanalytical Chemistry* **1992,** *333* (1), 127-142.

130. Liu, J.; Hasche, E.; Dunn, R.; Smillie, C.; Dixson, H.; Bui, C.; Chiam, Q.; Elison, B.; Kilian, J.; Tie, H.; Lee, K., Clinical Outcome of Ultralow Dose Stress Only Myocardial

Perfusion Imaging (Uldso-Mpi) Performed with Concurrent Low Dose Coronary Artery Calcium Score (Cacs) Using State-of-the Art Dedicated Cardiac Hybrid Scanner (Ge570c), with Cadmium-Zinc-Telluride (Czt) Spect and Adaptive Statistical Iterative Reconstruction (Asir) Ct in Low Pre-Test Probability Patients. *Internal Medicine Journal* **2014,** *44*, 8-9.

131. Sakamoto, J., Super-ionic Conducting Oxide Electrolytes. *Handbook of Solid State Batteries* **2015,** *6*, 391.

132. Stramare, S.; Thangadurai, V.; Weppner, W., Lithium lanthanum titanates: a review. *Chemistry of Materials* **2003,** *15* (21), 3974-3990.

133. Thangadurai, V.; Weppner, W., Recent progress in solid oxide and lithium ion conducting electrolytes research. *Ionics* **2006,** *12* (1), 81-92.

134. Sharafi, A.; Yu, S.; Naguib, M.; Lee, M.; Ma, C.; Meyer, H. M.; Nanda, J.; Chi, M.; Siegel, D. J.; Sakamoto, J., Impact of air exposure and surface chemistry on Li–$Li_7La_3Zr_2O_{12}$ interfacial resistance. *Journal of Materials Chemistry A* **2017**.

135. Han, X.; Gong, Y.; Fu, K. K.; He, X.; Hitz, G. T.; Dai, J.; Pearse, A.; Liu, B.; Wang, H.; Rubloff, G., Negating interfacial impedance in garnet-based solid-state Li metal batteries. *Nature materials* **2016**.

136. Callister, W. D.; Rethwisch, D. G., *Materials science and engineering*. John Wiley & Sons NY: 2011; Vol. 5.

137. Anstis, G.; Chantikul, P.; Lawn, B. R.; Marshall, D., A critical evaluation of indentation techniques for measuring fracture toughness: I, direct crack measurements. *Journal of the American Ceramic Society* **1981,** *64* (9), 533-538.

138. Harmer, M.; Brook, R., Fast firing- microstructural benefits. *Trans. J. Br. Ceram. Soc.* **1981,** *80* (5), 147.

139. Wollmershauser, J. A.; Feigelson, B. N.; Gorzkowski, E. P.; Ellis, C. T.; Goswami, R.; Qadri, S. B.; Tischler, J. G.; Kub, F. J.; Everett, R. K., An extended hardness limit in bulk nanoceramics. *Acta Materialia* **2014,** *69*, 9-16.

140. Goldstein, A., Correlation between $MgAl_2O_4$-spinel structure, processing factors and functional properties of transparent parts (progress review). *Journal of the European Ceramic Society* **2012,** *32* (11), 2869-2886.

141. Barsoum, W., *Fundamentals of Ceramics*. Taylor & Francis: 2002.

142. Richerson, D. W., *Modern ceramic engineering: properties, processing, and use in design*. CRC press: 2005.

143. Wang, W.; Fu, Z.; Wang, H.; Yuan, R., Influence of hot pressing sintering temperature and time on microstructure and mechanical properties of TiB_2 ceramics. *Journal of the European Ceramic Society* **2002,** *22* (7), 1045-1049.

144. Daniels, A.; Lowrie, R.; Gibby, R.; Cutler, I. B., Observations on normal grain growth of magnesia and calcia. *Journal of the American Ceramic Society* **1962,** *45* (6), 282-285.

145. Spriggs, R.; Brissette, L.; Vasilos, T., Grain growth in fully dense magnesia. *Journal of the American Ceramic Society* **1964,** *47* (8), 417-418.

146. Turnbull, D., Theory of grain boundary migration rates. *J. Metals (NY)* **1951,** *3*.

147. Brook, R., The impurity-drag effect and grain growth kinetics. *Scripta Metallurgica* **1968,** *2* (7), 375-378.

148. Coble, R. L., Sintering crystalline solids. II. Experimental test of diffusion models in powder compacts. *Journal of Applied Physics* **1961,** *32* (5), 793-799.

149. Wolfenstine, J.; Sakamoto, J.; Allen, J., Electron microscopy characterization of hot-pressed Al substituted $Li_7La_3Zr_2O_{12}$. *Journal of Materials Science* **2012,** *47* (10), 4428-4431.

150. Gordon, R. S., Mass transport in the diffusional creep of ionic solids. *Journal of the American Ceramic Society* **1973,** *56* (3), 147-152.

151. Ruoff, A., Mass transfer problems in ionic crystals with charge neutrality. *Journal of Applied Physics* **1965,** *36* (9), 2903-2907.

152. Cherniak, D., Rare earth element and gallium diffusion in yttrium aluminum garnet. *Physics and Chemistry of Minerals* **1998,** *26* (2), 156-163.

153. Jiménez-Melendo, M.; Haneda, H.; Nozawa, H., Ytterbium cation diffusion in yttrium aluminum garnet (YAG)—implications for creep mechanisms. *Journal of the American Ceramic Society* **2001,** *84* (10), 2356-2360.

154. De Jonghe, L. C.; Rahaman, M. N., 4.1 Sintering of Ceramics. *Handbook of Advanced Ceramics: Materials, Applications, Processing and Properties* **2003,** *2*, 187.

155. Rahaman, M. N., *Sintering of ceramics*. CRC press: 2007.

156. Barrett, C. S., 'Recrystallization Texture of Aluminum after Compression. *Trans. Metall. Soc. AIME* **1940,** *137*, 128-149.

157. Jensen, D. J., Growth rates and misorientation relationships between growing nuclei/grains and the surrounding deformed matrix during recrystallization. *Acta Metallurgica et Materialia* **1995,** *43* (11), 4117-4129.

158. Gleiter, H., Theory of grain boundary migration rate. *Acta Metallurgica* **1969,** *17* (7), 853-862.

159. Beck, P. A.; Sperry, P. R.; Hu, H., The orientation dependence of the rate of grain boundary migration. *Journal of Applied Physics* **1950,** *21* (5), 420-425.

160. Parthasarathi, M.; Beck, P. A., The oriented growth mechanism of the formation of recrystallization textures in aluminum. *Transactions of the Metallurgical Society of AIME* **1961,** *221* (4), 831-838.

161. Yoshida, H.; Liebmann, B.; Lücke, K., Orientation of recrystallized grains in strained aluminum single crystals. *Acta Metallurgica* **1959,** *7* (1), 51-56.

162. Metals, A. S. f., *Recrystallization, grain growth, and textures: papers presented at a seminar of the American Society for Metals, October 16 and 17, 1965*. American Society for Metals: 1966.

163. Kohara, S.; Parthasarathi, M.; Beck, P. A., Anisotropy of boundary mobility. *Journal of Applied Physics* **1958,** *29* (7), 1125-1126.

164. Kim, Y.; Jo, H.; Allen, J. L.; Choe, H.; Wolfenstine, J.; Sakamoto, J., The Effect of Relative Density on the Mechanical Properties of Hot-Pressed Cubic $Li_7La_3Zr_2O_{12}$. *Journal of the American Ceramic Society* **2016**.

165. Wachtman, J. B.; Cannon, W. R.; Matthewson, M. J., Types of Mechanical Behavior. In *Mechanical Properties of Ceramics*, John Wiley & Sons, Inc.: 2009; pp 27-33.

166. Davidge, R. W., *Mechanical behaviour of ceramics*. CUP Archive: 1979.

167. Sharafi, A.; Yu, S.; Naguib, M.; Lee, M.; Ma, C.; Meyer, H. M.; Chi, M.; Nanda, J.; Siegel, D. J.; Sakamoto, J., Impact of Air Exposure and Surface Chemistry on the Li-$Li_7La_3Zr_2O_{12}$ Interfacial Resistance. *Journal of Materials Chemistry A* **2017**.

168. Virkar, A. V.; Viswanathan, L., A three-dimensional approach to the electrolytic degradation of solid electrolytes. *Journal of Materials Science* **1983,** *18* (4), 1202-1212.

169. Cook, R. F.; Lawn, B. R.; Fairbanks, C. J., Microstructure-Strength Properties in Ceramics: I, Effect of Crack Size on Toughness. *J. Am. Ceram. Soc.* **1985,** *68* (11), 604-615.

170. Rice, R., Grain size and porosity dependence of ceramic fracture energy and toughness at 22 C. *Journal of Materials Science* **1996,** *31* (8), 1969-1983.

171. Chou, H.; Case, E. D., Characterization of some mechanical properties of polycrystalline yttrium iron garnet (YIG) by non-destructive methods. *Journal of materials science letters* **1988,** *7* (11), 1217-1220.

172. Shahriari, D.; Koffler, J. Y.; Tuszynski, M. H.; Campana, W. M.; Sakamoto, J. S., Hierarchically Ordered Porous and High-Volume Polycaprolactone Microchannel Scaffolds Enhanced Axon Growth in Transected Spinal Cords. *Tissue Engineering Part A* **2017,** *23* (9-10), 415-425.

173. Rice, R., Microstructural dependence of fracture energy and toughness of ceramics and ceramic composites versus that of their tensile strengths at 22 C. *Journal of Materials Science* **1996,** *31* (17), 4503-4519.